eXPRESS Polymer Letters Vol.8, No.6 (2014) 373
Available online at www.expresspolymlett.com
DOI: 10.3144/expresspolymlett.2014.41

Editorial corner – a personal view
Chemical modification of graphene for functional polymer nanocomposites

J. Seppälä[*], *N. D. Luong*

Aalto University, Department of Biotechnology and Chemical Technology, PO Box 16100, FI-00076 Aalto, Finland

Graphene is a single layer of sp^2-bonded carbon atoms forming a two-dimensional honeycomb structure. It could be considered as a basic structural element of all other graphitic carbons. Many physical properties of graphene have been characterized experimentally and some of them are higher than those of any other known materials. For example, it exhibits a Young's modulus of 1TPa and ultimate strength of 130 GP. The very high thermal conductivity of above 5000 $W \cdot m \cdot K^{-1}$ corresponds to the upper bound of the highest values for SWCNTs [DOI: 10.1021/nl0731872]. Additionally, it has high electrical conductivity of around 6000 $S \cdot m^{-1}$. Especially, graphene is completely impermeable to any gas [DOI: 10.1021/nl801457b]. It has very large surface area and tunable surface properties. Based on these valuable characteristics, in the last decade, graphene has been viewed as promising material for many applications including polymer nanocomposites (PNCs).

However, due to the inertness, graphene is not compatible with most of polymers. Thus, it must be appropriately modified to provide it with suitable functional groups which are able to have good dispersion and strong interactions or even forming covalent bonds with the chemical moieties in polymers. Using graphene oxide (GO), an oxidized form of graphene, and its various derivatives have widely been considered as the most promising approach for the preparation of graphene. GO contains several oxygen functionalities such as hydroxyl and carboxyl groups and it is readily compatible with a nanocellulose (NFC) in form of suspension. Taking this advantage, we combined them together to form a mechanically strong and conductive composite film [DOI: 10.1039/C1JM12134K]. NFC/graphene porous structure has been used effectively as host matrix for sulphur impregnation in lithium sulphur batteries [DOI: 10.1016/j.jpowsour.2013.12.081]. In a study on polyimide graphene composite film [DOI: 10.1016/j.polymer.2011.09.033], GO has been treated with ethylisocyanate and the resulted modified GO was seen as good reinforcement in polyimide (PI). Electrical conductivity of the PI/graphene composite film is above the antistatic criterion. Polymer and graphene can also be combined in PNCs *via grafting-to or grafting-from* approaches [DOI: 10.1002/marc.201100527]. By *grafting-to/grafting-from* approaches, covalent binding between polymers graphene sheets is formed, leading to a single compound of PNCs where graphene forms an integral part of the polymer chains. However, by these methods, the covalent bonding can enhance some properties while it may be negative for some others, for example, electrical conductivity. Thus, quantitative estimation on the kind of chemical functionalization and degree of the functionalization on the single layer properties such as mechanical and electrical properties would be highly valuable [DOI: 10.1021/ma401606d].

In general, chemical modification of graphene is an effective way to widen the utilization of graphene in PNCs for different purposes. GO has been used as starting material to modify the structure of graphene as it contains several active groups which are hydroxyl, carboxyl and epoxide functionalities.

[*]Corresponding author, e-mail: Jukka.Seppala@aalto.fi

eXPRESS Polymer Letters Vol.8, No.6 (2014) 374–386
Available online at www.expresspolymlett.com
DOI: 10.3144/expresspolymlett.2014.42

Ionic elastomers based on carboxylated nitrile rubber (XNBR) and magnesium aluminum layered double hydroxide (hydrotalcite)

A. Laskowska[1*], *M. Zaborski*[1], *G. Boiteux*[2], *O. Gain*[2], *A. Marzec*[1], *W. Maniukiewicz*[3]

[1]Institute of Polymer and Dye Technology, Technical University of Lodz, Stefanowskiego 12/16, 90-924 Lodz, Poland
[2]Ingénierie des Matériaux Polymères, Université Claude Bernard Lyon1, UMR CNRS 5223, 15 Bd A. Latarjet, 69622 Villeurbanne, France
[3]Institute of General and Ecological Chemistry, Technical University of Lodz, Zeromskiego 116, 90-924 Lodz, Poland

Received 31 October 2013; accepted in revised form 12 January 2014

Abstract. The presence of carboxyl groups in carboxylated nitrile butadiene rubber (XNBR) allows it to be cured with different agents. This study considers the effect of crosslinking of XNBR by magnesium aluminum layered double hydroxide (MgAl-LDH), known also as hydrotalcite (HT), on rheometric, mechano-dynamical and barrier properties. Results of XNBR/HT composites containing various HT loadings without conventional curatives are compared with XNBR compound crosslinked with commonly used zinc oxide. Hydrotalcite acts as an effective crosslinking agent for XNBR, as is particularly evident from rheometric and Fourier transform infrared spectroscopy (FTIR) studies. The existence of ionic crosslinks was also detected by dynamic mechanical analysis (DMA) of the resulting composites. DMA studies revealed that the XNBR/HT composites exhibited two transitions – one occurring at low temperature is associated to the T_g of elastomer and the second at high temperature corresponds to the ionic transition temperature T_i. Simultaneous application of HT as a curing agent and a filler may deliver not only environmentally friendly, zinc oxide-free rubber product but also ionic elastomer composite with excellent mechanical, barrier and transparent properties.

Keywords: *rubber, mechanical properties, carboxylated nitrile rubber, crosslinking, ionic elastomers*

1. Introduction

Carboxylated acrylonitrile butadiene rubber (XNBR) is a terpolymer composed of acrylonitrile, butadiene and monomers containing carboxyl groups, such as acrylic and methacrylic acids. XNBR contains different active functional groups, including nitrile groups (–CN), carboxylic groups (–COOH), and alkene groups. All of these groups can participate in the crosslinking reaction, leading to the formation of different types of bonds, mainly covalent and ionic. Lateral carboxyl functionalities –COOH provide additional curing sites and make possible to use curing agents that can react with them contributing to the formation of ionic bonds [1, 2]. The conventional curing agents for XNBR that lead to ionic crosslinks are generally based on salts and oxides of multivalent metals (e.g., ZnO, MgO, CaO), where the crosslinking reaction occurs through the formation of the corresponding salt of the metal ion [3]. Recently, it has been demonstrated that magnesium aluminum layered double hydroxides (MgAl-LDHs) may act not only as a filler but also as a curative for XNBR, because of the Mg-Al-OH framework [4]. Pradhan *et al*. [5] reported that LDH has considerable potential for use as a reinforcing nanofiller in elastomers and also as a curing agent in car-

*Corresponding author, e-mail: anna.laskowska@hotmail.com

boxylated elastomers. The mechanical properties of XNBR/decane sulfonate-modified LDH nanocomposites were enhanced due to the secondary interactions that occur between carboxylated rubber and layered double hydroxide filler. The use of LDHs has been already reported in elastomer composites of ethylene-propylene-diene rubber (EPDM) [5–9], acrylonitrile-butadiene rubber (NBR) [10], chloroprene rubber (CR) [11], silicone rubber (SR) [12, 13], and polyurethane PU [14–16] and solution styrene-butadiene rubber (SSBR) [17]. However, in the literature, there is no information on the impact of high loadings of unmodified magnesium aluminum layered double hydroxide used as a filler and a curing agent on the crosslinking process in XNBR. Layered double hydroxides (LDHs), also known as anionic clays, are minerals consisting of stacks of positively charged metal hydroxide layers (1:1, brucite-like) with interlayer anions that maintain the overall charge neutrality [18]. LDH is characterized by a layered structure and hexagonal particles with lateral dimensions of 50–400 nm. LDH particles are often very large and it is difficult to produce the single LDH sheets by the exfoliation because of strong electrostatic attraction between the layers and interlayer anions due to the surface charge density [19]. On the contrary to cationic clays that occur abundantly on the Earth, only a few anionic clays have been found in nature (e.g. hydrotalcite, $Mg_6Al_2(OH)_{16}CO_3{\cdot}4H_2O$), and most LDHs are synthesized in the laboratory [20]. LDHs have attracted researchers attention due to their interesting properties, such as their layered structure, simplicity of synthesis, possibility of controlling particle size and aspect ratio by changing the reaction conditions and their highly designable characteristics. LDHs are widely used for the preparation of polyolefin nanocomposites with improved thermal properties, for example, the poly(ethylene terephthalate) (PET)/LDH nanocomposites exhibited enhanced thermal stability relative to pure PET [21]. Recent research has demonstrated that incorporation of LDHs into a rubber matrix can remarkably enhance polymer properties such as mechanical, thermal and reduce gas permeability [6, 13]. Some other physicochemical properties were also improved, compared to the one of neat polymers or composites that contain conventional fillers. Das *et al*. [10] developed a rubber composite based on zinc-stearate-modified LDH with NBR that does not require the incorporation of ZnO and stearic acid in the sulfuric curing system. In our work, the advantage of using unmodified magnesium/aluminum LDH in elastomer systems (XNBR or its hydrogenated counterpart HXNBR) lays in the possibility of full replacement of conventional metal oxide curatives used for functionalized elastomers (XNBR, HXNBR), particularly ZnO, which is believed to be harmful for the environment [22]. While crosslinking XNBR with a conventional sulfur vulcanizing system or ZnO is well known and commonly used, the application of magnesium aluminum layered double hydroxides MgAl-LDH for crosslinking process of XNBR is still a relatively new approach. This work presents the influence of hydrotalcite HT on the curing characteristics, mechanical and barrier properties of the XNBR composites. The results from XNBR/HT composites containing various filler loadings of HT (2.5, 5, 10, 20 and 30 parts per hundred rubber, phr) without any conventional curatives are compared with the results from XNBR compound crosslinked with commonly used zinc oxide to demonstrate that this mineral has potential to be an interesting alternative to zinc oxide. The HT may provide the metal ions for metal-carboxylate curing, however it was found that quite high loadings of HT filler are needed for the preparation of composites with mechanical parameters that are comparable to those of XNBR/ZnO5. However, the addition of large amounts of inexpensive and easily synthesized filler is advantageous because it reduces the cost of the final product.

2. Experimental

2.1. Materials

The carboxylated acrylonitrile-butadiene rubber XNBR used in this study was Krynac® X 750 (7 wt% carboxyl groups content, 27 wt% acrylonitrile content, Mooney viscosity ((ML (1+4) 100ºC) 47 and zinc oxide were supplied by LANXESS (Leverkusen, DE). Magnesium aluminum layered double hydroxide named hydrotalcite was obtained from Sigma Aldrich (652288, Schnelldorf, DE) was used in its unmodified form as a reinforcing filler for XNBR rubber and simultaneously played the additional role of a curative for XNBR. The compounding ingredients and the amounts used for this study are presented in Table 1.

Table 1. Formulation of XNBR compounds [phr]

Component	X	XZnO5	XHT2.5	XHT5	XHT10	XHT20	XHT30
XNBR	100	100	100	100	100	100	100
HT	0	0	2.5	5	10	20	30
ZnO	0	5	0	0	0	0	0

2.2. Characterization of hydrotalcite

2.2.1. X-ray diffraction analysis (XRD)

Room-temperature powder X-ray diffraction patterns were collected using a PANalytical X'Pert Pro MPD diffractometer in Bragg-Brentano reflecting geometry with (CuK_α) radiation from a sealed tube (Almelo, Netherlands). Data were collected in the 2θ range of 2–70º with a 0.0167° step and 20-s exposition per step.

2.2.2. X-ray photoelectron spectroscopy (XPS)

The surface elemental composition of HT was determined by X-ray photoelectron spectroscopy (XPS) analysis to confirm its stoichiometric composition. XPS spectra was recorded by using an X-ray photoelectron spectrometer Prevac (Rogow, Poland) equipped with hemispheric electron energy analyzer SES 2002, VG Scienta (Uppsala, Sweden) with an aluminum (mono) K_α source (1486.6 eV). The aluminum K_α source was operated at 15 kV and 25 mA. For hydrotalcite sample, a high-resolution survey (pass energy 50 eV) was performed in the appropriate spectral regions. All core level spectra were referenced to the C 1s neutral carbon peak at 284.6 eV.

2.3. Preparation of XNBR/HT composites

The samples were prepared using an internal mixer Brabender Measuring Mixer N50 (Duisburg, DE). The rubber compounds were processed at a rotor speed of 50 rpm (revolutions per minute), and the initial temperature was set to 70°C. After approximately 5 minutes of rubber mastication, the HT (2.5, 5, 10, 20 and 30 phr) was added. The total time of compounding in the internal mixer was 20 minutes. Subsequently, the compounded rubbers were milled in a laboratory-scale open two-roll mixing mill.

2.4. Curing behavior

The curing characteristics of XNBR composites were determined using a MonTech Moving Die Rheometer MDR 3000 (Buchen, DE) at 160°C for 120 minutes. A sinusoidal strain of 7% and frequency of 1.67 Hz was applied. The optimum cure time (t_{90}), scorch time (t_2), minimum torque (S_{min}), maximum torque (S_{max}), and delta torque (ΔS) were determined from the curing curves. The mixed stocks were cured in a standard hot press at 160°C for t_{90}.

2.5. Infrared spectroscopy ATR-FTIR

Attenuated total reflection Fourier transform infrared (ATR-FTIR) spectra were recorded on a Thermo Scientific Nicolet 6700 FT-IR spectrometer (Waltham, MA, USA) at room temperature with a resolution of 4 cm^{-1} and a 64-scan signal from 600–4000 cm^{-1} in absorbance mode.

2.6. Dynamic mechanical analysis

Dynamic mechanical analysis (DMA) was performed by means of a Dynamic Mechanical Analyzer TA Instruments Q 800 (New Castle, USA) operating in a tension mode at a frequency of 10 Hz in the temperature range of -80 to 100°C and at a heating rate of 2°C/min.

2.7. Crosslink density

The vulcanizates were subjected to equilibrium swelling in toluene for 48 h at room temperature. The swollen samples were then weighted on a torsion balance, dried in a dryer at a temperature of 60°C to a constant weight, and reweighed after 48 h. The crosslinking density was determined based on Flory-Rehner's equation [23]. The Huggins parameter of the elastomer-solvent interaction χ was calculated from Equation (1) [24–26]:

$$\chi = 0.487 + 0.228V_r \quad (1)$$

where V_r is the volume fraction of elastomer in the swollen gel.

2.8. Stress-strain behavior

The tensile properties were carried out with a ZWICK 1435 tensile testing machine of Zwick Roell Group (Ulm, DE). The moduli at 100, 200 and 300% elongation, tensile strength, and elongation at

break were measured at room temperature with a crosshead speed of 500 mm/min according to the PN-ISO 37-2005 standard. For this purpose, five different dumbbell-shaped specimens were tested, and the average value of each formulation was reported.

2.9. Air permeability

The through-plane air permeability of the composites was determined using the manometric method in accordance with the ASTM standard D1434, using circular samples of 30 mm in diameter and 1 mm in thickness. The tests were conducted using atmospheric air at room temperature.

2.10. UV aging

The UV aging studies were conducted for rubber composites using an UV2000, Atlas solar simulation chamber (Linsengericht, DE). The measurement lasted for 120 h and consisted of two alternately repeating segments with the following parameters: a day segment (radiation intensity of 0.7 W·m^{-2}, temperature of 60°C, duration of 8 h), a night segment (without UV radiation, temperature of 50°C, duration of 4 h). After UV aging the stress-strain tests were performed. The UV aging coefficients K were calculated according to the relationship Equation (2):

$$K = \frac{(TS \cdot EB)_{\text{after aging}}}{(TS \cdot EB)_{\text{before aging}}} \quad (2)$$

where TS – tensile strength [MPa], EB – elongation at break [%]. The crosslink densities of the samples subjected to UV radiation were measured through a swelling method with toluene as the solvent, which was described above.

2.11. Scanning electron microscopy (SEM)

The fractured surfaces of the prepared materials were inspected using a scanning electron microscopy with a microscope SEM HITACHI S800 (Tokyo, Japan) at the accelerating voltage of 15 kV. Prior to SEM observations, liquid nitrogen-fractured surfaces of the composites were Au/Pd sputtered (with a thickness of approximately 10 nm).

3. Results and discussion

3.1. Hydrotalcite surface properties

Figure 1 presents the X-ray diffraction data for synthetic hydrotalcite. The interlayer distance d, calculated according to the Bragg's equation, was found to be 0.77 nm. The XRD analysis of unmodified MgAl-CO_3^{2-} structure showed the basal reflections (003), (006), (009), which correspond to d-spacings of 0.77, 0.34 and 0.26 nm respectively. The sample of hydrotalcite did not contain any impurities, as generally, such materials are easily synthesized with a high degree of purity. The atomic content for hydrotalcite surface composition was determined by XPS analysis to confirm its stoichiometric composition. The total amount of magnesium, aluminum, oxygen and carbon was taken as 100%, the atomic percentage of each element is given in Table 2. Based on the obtained data we could confirm that the ratio of magnesium to aluminum is approximately the same as stoichiometric ratio of the elements specified on the basis of chemical formula $Mg_6Al_2(OH)_{16}CO_3 \cdot 4H_2O$. Also, the oxygen content is comparable to the typical content of the mineral. However, the atomic percentage of carbon on the

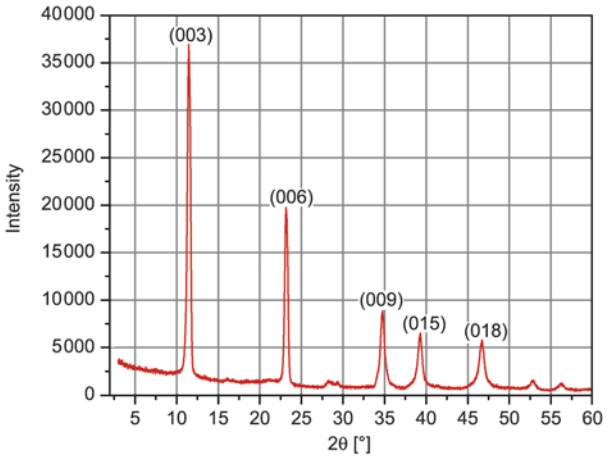

Figure 1. X-ray diffraction patterns of unmodified hydrotalcite HT

Table 2. XPS atomic content for hydrotalcite surface composition

Atom	C	O	Al	Mg
		[atomic %]		
Hydrotalcite	39.2	42.2	4.5	14.1

Table 3. Binding energies of the main peaks for the hydrotalcite

Photoelectron line positions [eV]		Chemical environment
Al. 2p	73.9	Al-OH
Mg 2p	49.6	Mg-OH
O 1s	531.6	Oxygen bonds in hydroxyl groups
C 1s	284.6	Adventitious carbon
C 1s	289.0	CO_3^{2-}

surface of the filler particles exceeds the expected value. This may result from a surface contamination with impurities derived from the decomposition of carbon compounds adsorbed from the air. Table 3 shows binding energies of the main peaks for hydrotalcite sample. For XPS C 1s there are two components, one appears at *EB* = 284.6 eV, which corresponds to so-called 'adventitious carbon' layer (C–C bonds, contamination) and second one appears at *EB* = 289.0 eV, which corresponds to inorganic carbonates, here CO_3^{2-}. Summarizing, surface analysis of hydrotalcite confirmed its stoichiometric composition and at the same time indicated that the surface of mineral is covered with a thin layer of carbon.

3.2. Curing studies

Figures 2 and 3 present the variation in the normalized elastic (*S*′) and viscous (*S*″) components of the torque versus time, respectively. The curves were obtained from a MDR rheometer at 160°C. Figure 2 shows the influence of an increase in the amount of HT on the curing curves compared with the curves for the crosslinking XNBR with 5 phr of ZnO and pure XNBR. In the case of pure XNBR, self-crosslinking is possible through the formation of anhydride linkages between two carboxylic groups, however this process may occur at rather more severe conditions than 160°C [1, 2, 27]. The curves show the continuous growth of the elastic component *S*′ due to the increase of crosslinks of XNBR with ZnO as well as HT at each concentration (2.5, 5, 10, 20 and 30 phr). The difference between maximum torque S'_{max} and minimum torque S'_{min}, which is called the torque increment $\Delta S'$ (Table 4), gradually rises with the content of HT which reflects an increment of the crosslink density and thus, an improvement in the mechanical properties. It can be clearly observed that an increase in the amount of HT leads to a greater number of crosslinks and consequently higher values of *S*′. However, a plateau (Figure 2) was reached faster when ZnO was used as a curing agent, in the case of HT, the plateau was achieved more slowly during the analyzed reaction

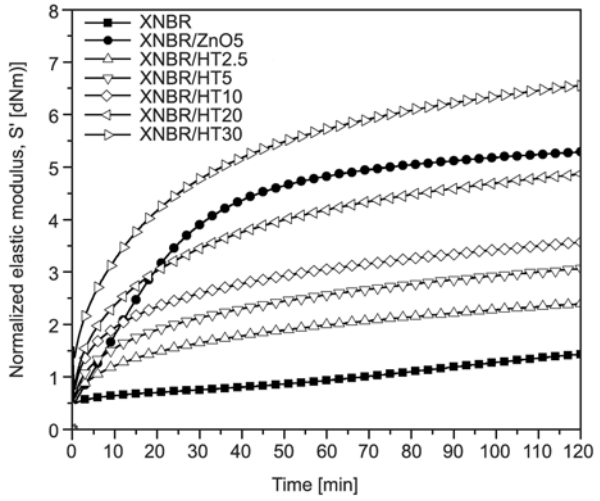

Figure 2. Normalized elastic component (*S*′) of the torque as a function of time for XNBR compounds crosslinked at 160ºC

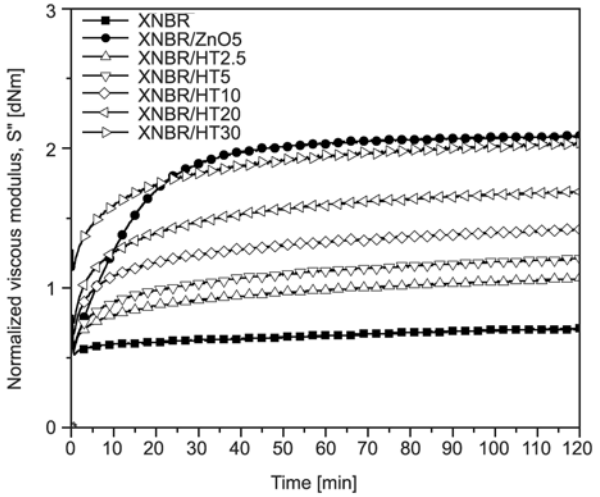

Figure 3. Normalized viscous component (*S*″) of the torque as a function of time for XNBR compounds crosslinked at 160ºC

Table 4. Rheometric properties of XNBR/HT composites crosslinked at 160ºC

Sample name	S'_{min} [dNm]	S'_{max} [dNm]	$\Delta S'$ [dNm]	t_2 [min]	t_{90} [min]	CRI [min^{-1}]
X	0.5	1.4	0.9	0.0	0	–
XZnO5	0.5	5.3	4.8	7.9	59	1.96
XHT2.5	0.6	2.4	1.8	27.6	90	1.60
XHT5	0.6	3.1	2.5	11.8	87	1.33
XHT10	0.8	3.6	2.8	7.0	83	1.32
XHT20	0.9	4.9	4.0	5.1	79	1.35
XHT30	1.4	6.6	5.2	4.1	77	1.37

Note: S'_{min} – minimal torque; S'_{max} – maximum torque; $\Delta S'$ – torque increment; t_2 – scorch time; t_{90} – optimum cure time, CRI – cure rate index $100/(t_{90} - t_2)$.

time. However, the scorch time for XNBR/HT composites was shorter than that for XNBR/ZnO, and t_2 parameter (Table 4) was strongly dependent on the HT loading (decreasing with an increase in HT amount). As can be observed from the curves, there is practically no induction time. The compounds begin to vulcanize almost immediately, what is characteristic of crosslinking with metal oxides [28]. The presence of the MgAl-LDH also affects the viscosity of the compounds, resulting in higher values for normalized viscous component S'' (Figure 3). It is well known from the literature that the increase in viscous component S'' with time, is due to the formation of ionic bonds [27–31]. The curve corresponding to the curing with the ZnO, which also forms ionic crosslinks, showed a similar behavior to that observed for XNBR cured with HT. For each HT concentration, S'' curves that increased with the reaction time were obtained, which is a characteristic of ionic vulcanization. Furthermore, as the HT loading increases, the value for the viscous component increases and here, S'' increased until it reached a plateau for each sample, regardless of the curative type used. In our opinion, curing with HT undoubtedly gives rise to ionic crosslinks. Table 4 presents the rheometric parameters of the XNBR compounds. From the values of t_{90} it can be concluded that the optimum curing time slightly decreases with an increase in the amount of HT. The cure rate index (CRI) indicates that a faster curing reaction was achieved when ZnO was used compared to that of XNBR/HT. Based on the rheometric data rubber compounds were subsequently cured in a standard hot press at 160°C, at the optimum cure time (t_{90}) for the samples. It should be mentioned that crosslinking of XNBR with HT yields high transparent properties in the final composites, even when such high content as 30 phr of HT is added (Figure 4). Optical transparency, which can be a desirable characteristic, was not observed in case of XZnO5 composite that was opaque. The transparency of rubber composites filled with LDHs has already been reported for NBR vulcanized with sulfur [10] and SSBR also vulcanized using a conventional sulfur cure system [17].

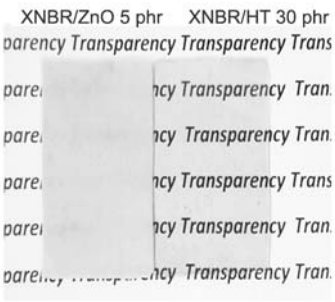

Figure 4. Opacity of XNBR with 5 phr of ZnO and optical transparency of XNBR with 30 phr of HT

3.3. FTIR studies

Figures 5 and 6 show the ATR spectra of the sample without crosslinking agent (XNBR pure), the sample cured with ZnO (5 phr) and crosslinked with various amounts of HT (5, 10, 20 and 30 phr) at 160°C. Each spectra shows the existence of two principal absorption peaks for the XNBR compounds at 2928 and 2844 cm^{-1} due to the $–CH_2$ groups on the rubber backbone. Another strong absorption peak that appears at 2237 cm^{-1} is due to the CN-group in the acrylonitrile component. Those peaks remain unchanged during the crosslinking process for all investigated samples (Figure 5). The most important region of spectrum is the range between 1800 and 1500 cm^{-1}, where peaks result from the >C=O

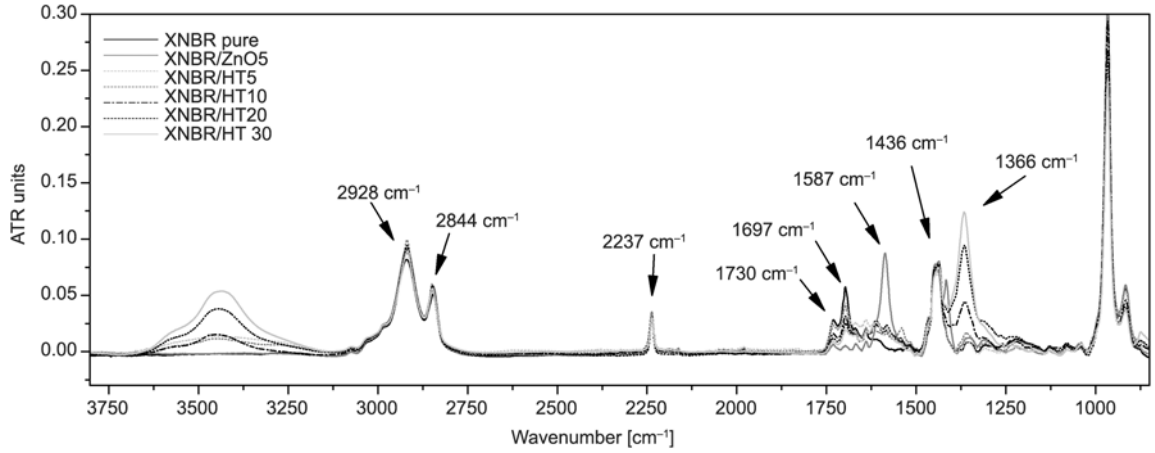

Figure 5. ATR spectra of XNBR compounds with various loadings of HT

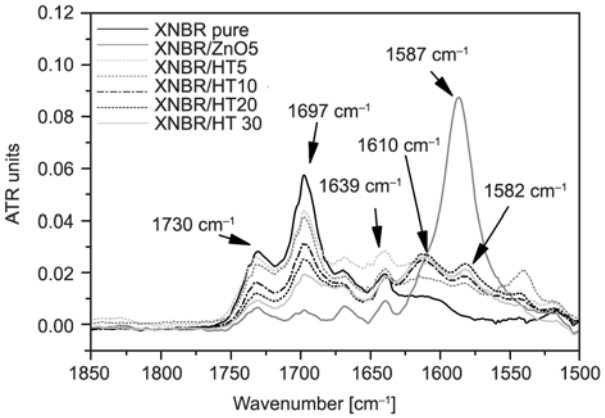

Figure 6. ATR spectra (1850–1500 cm^{-1}) of XNBR containing various loadings of hydrotalcite HT

group of the carboxylic component in the rubber (Figure 6). The uncured sample shows two bands at 1697 and 1730 cm^{-1}, which disappear in the sample crosslinked with ZnO and their intensities decrease when XNBR is cured with increasing amount of HT. This is due to the chemical change from weak acid to ionic bonds or slat formation. The first peak (1697 cm^{-1}) is attributed to carbonyl stretching of hydrogen-bonded acid dimer, whereas the second one (1730 cm^{-1}) is due to carbonyl stretching of monocarboxylic acid. The peak for –COOH appearing at a wavelength of 1697 cm^{-1} is reduced and a new peak at 1587 cm^{-1} is observed for the sample cured with ZnO, that is attributed to the formation of ionic clusters between $–COO^-$ groups and Zn^{2+} ions of ZnO, or. For samples crosslinked with HT the intensity of peaks at 1697 and 1730 cm^{-1}, related to carboxylic groups, decreases with increasing content of metal hydroxide filler, what suggests that HT has evident influence in the dimer formation [1], and emphasizes the decrease of free acid groups with increasing HT amount [5]. According to the obtained data it can be assumed that the crosslinking occurs only with the –COOH groups of the elastomeric chain. The ionic bonds formed from the carboxylic groups and the magnesium aluminum layered double hydroxide generate some new bands at 1639, 1610 and 1582 cm^{-1}, which intensities slightly increase with HT content. According to the work of Pradhan, such a new band which appears at 1582 cm^{-1} corresponds to the C=O stretching vibration of the metal carboxylate salt [5], that may be some type of confirmation of the chemical interaction between XNBR and HT. Table 5 shows the interpretation of existing peaks.

3.4. Dynamic mechanical analysis (DMA)

Figure 7a–7c show the variation of tan δ, storage modulus (E') and loss modulus (E'') with temperature for XNBR compounds at an oscillation frequency of 10 Hz. The values of T_g, T_i and E' are showed in Table 6. As expected, the E' for XNBR containing the highest amount of HT (30 phr) was the best of all tested samples, consequently the peak height of tan δ was reduced significantly (Figure 7a, Table 6). The incorporation of increasing amounts of layered mineral gradually reduces the amplitude of tan δ that indicates reinforcement by the filler which hinders the mobility of the rubber chains due to molecular confinement. The presence of HT at each content increases the curves of E' as well as the maximum for E'' and shifts tan δ towards higher temperature in comparison to the neat XNBR, as a consequence of the increase in the crosslink density. The increase of storage modulus E' with increasing HT concentration is probably due to the strong interfacial interactions between HT particles and XNBR matrix. The neat XNBR sample gives only one tran-

Table 5. Peak assignments of FTIR spectra for XNBR composites

Wavenumber [cm^{-1}]	Assignment
3420	Stretching of –O–H
2928	Asymmetric stretching of the methylene group $–CH_2$
2844	Symmetric stretching of the methylene group $–CH_2$
2237	Stretching vibration of nitrile triple bonds in XNBR
1730	Carbonyl stretching of monocarboxylic acid
1697	Carbonyl stretching vibration of H-bonded –COOH group
1640–1670	Stretching of C=C
1610	Carbonyl stretching of magnesium hydroxycarboxylate salt
1587	Asymmetric carbonyl stretching vibration of zinc carboxylate salt
1582	Asymmetric carbonyl stretching vibration of magnesium carboxylate salt
1436	CH deformation, in-plane deformation of methylene group
1366	Asymmetric stretching of carbonate counter-ions CO_3^{2-}

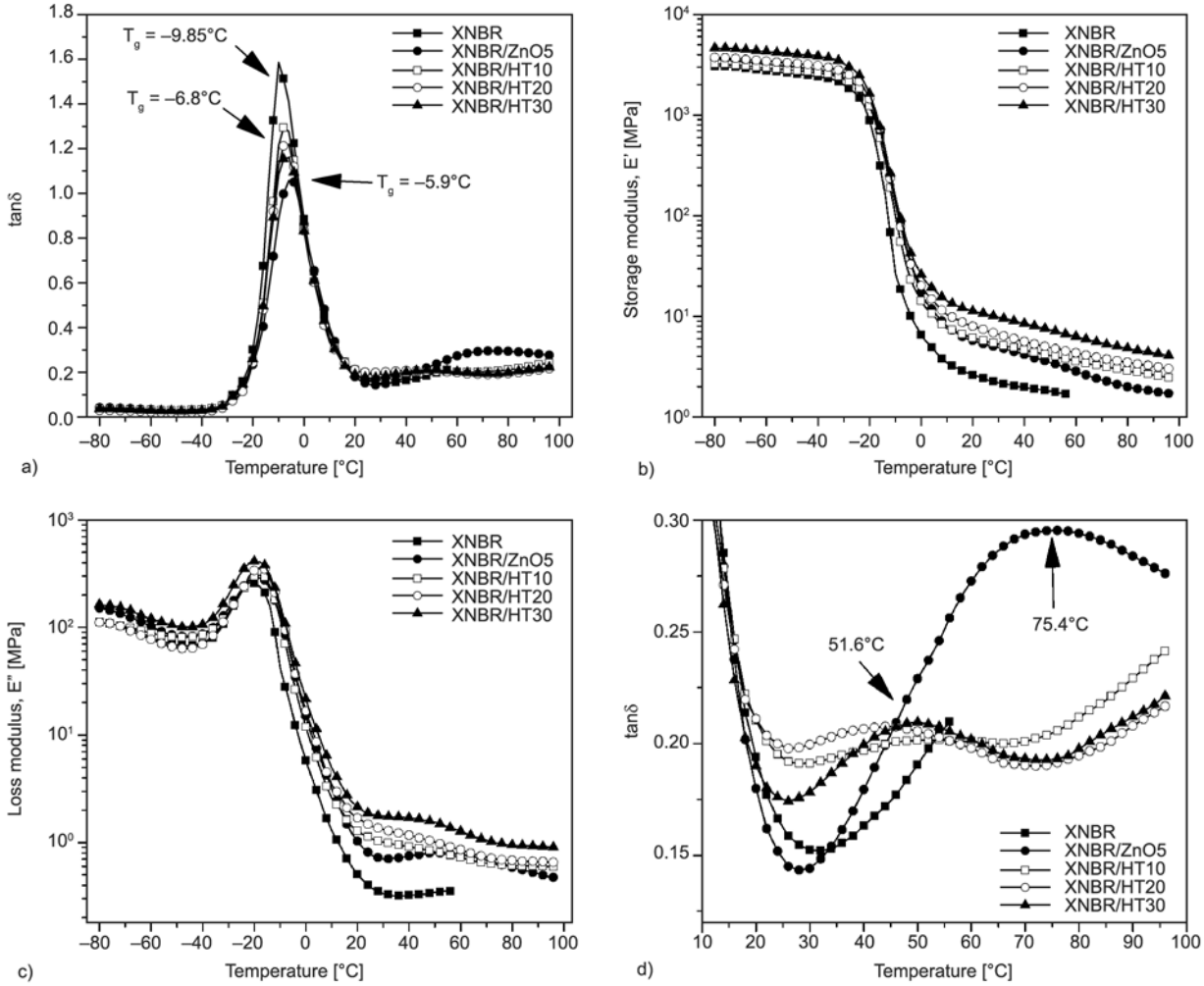

Figure 7. (a) Plot of tan δ, (b) plot of storage modulus E' (c) plot of loss modulus E'' versus temperature, (d) ionic transition region for XNBR composites. Vibration frequency, 10 Hz

Table 6. Dynamic mechanical measurements at 10 Hz of XNBR/HT composites

Sample name	T_g from E'' [ºC]	T_g from tan δ [ºC]	Height of tan δ [–]	T_i from tan δ [ºC]	E' at 25ºC [MPa]
X	–22.2	–9.9	1.59	–	2.3
XZnO5	–18.2	–5.9	1.06	75.4	5.2
XHT10	–18.0	–6.8	1.30	45.6	5.6
XHT20	–18.0	–6.8	1.20	45.6	7.1
XHT30	–18.0	–6.8	1.16	51.6	10.4

sition corresponding to the glass transition temperature of elastomer (T_g = –9.9°C), however it can be observed from Figure 7d that there occurs an additional high temperature relaxation corresponding to ionic temperature transition T_i. This is particularly evident for XNBR cured with ZnO (T_i = 75.4°C). This transition, is associated with the formation of ionic structures and occurs over a wide range of temperatures. In general, it is attributed to the hard phase arising from the formation of ionic clusters or conglomerates [27, 32]. Those clusters or ionic associates begin to relax and weaken at the ionic transition temperature and consequently the elastomer loses its rigidity [28]. Figure 7d shows that the T_i peak height slightly increases with the HT content in XNBR formulation as well as shifts towards higher temperatures up to 51.6°C when 30 phr of HT is added. Table 6 shows the calculated values for the rubber glass transition and the ionic transition, obtained from the loss modulus E'' and tan δ versus temperature curves.

3.5. Mechanical properties and crosslink density

Table 7 shows the mechanical properties and the crosslink density values (v) of the XNBR compounds cured with ZnO or alternatively with HT at various loadings. Apparently, an improvement in the tensile strength was observed for all vulcanizates filled with HT compared with the neat XNBR, what can be attributed to the existence of an ionic/polar interaction between HT and rubber. XNBR is a polar rubber that contains –CN and –COOH functionalities and appears to be compatible with polar fillers containing basic –OH groups, such as layered double hydroxides. Evidently HT exhibited a reinforcing effect on the XNBR, which raised the moduli at 100, 200 and 300% elongation, and the tensile strength of the XNBR/HT composites gradually increased with increasing amounts of HT. Moreover, the presence of HT remarkably reduced the elongation at break of the XNBR composites compared to the unfilled neat gum, probably due to the reduced free volume as a result of the interaction between the filler and the matrix, as well as the higher crosslink density. The incorporation of ZnO in XNBR produced an ionic elastomer with higher mechanical parameters what is probably related to stronger interactions between ZnO particles and rubber matrix. However, we can observe that HT also effectively participates in crosslinking reaction of XNBR and contributes to obtain strong and stiff elastomeric composites. The crosslink density is an important parameter influencing rubber properties. Table 7 shows that the tear strength and the 300% modulus of the rubber containing 10 phr of HT are seen to be higher than those of the comparative neat rubber as well as XNBR cured with ZnO. What is worth to note is that network density of vulcanizates remarkably increases with an increasing level of HT in the XNBR compounds. The trend observed here is in harmony with that recorded in the case of the tensile strength and the increment in torque $\Delta S'$, which is further confirmation that layered double hydroxide may play a role not only as a reinforcing filler but also as a curative agent for functionalized elastomers such as XNBR.

3.6. Barrier properties

The dependence of air permeability on the XNBR composition is presented in Figure 8. An uncrosslinked, neat XNBR sample was too weak mechanically and was destroyed almost immediately by the pressure of the gas at the very beginning of the experiment. It is evident that the air permeability was reduced with increasing layered double hydroxide content, what is surely related to the higher network density of the samples. The barrier properties of XNBR are enhanced the most by the incorporation of 30 phr of hydrotalcite, the same sample that was characterized by the highest amount of ionic crosslinks. The effect of reduced permeability may be explained through strongly restricted the motion of

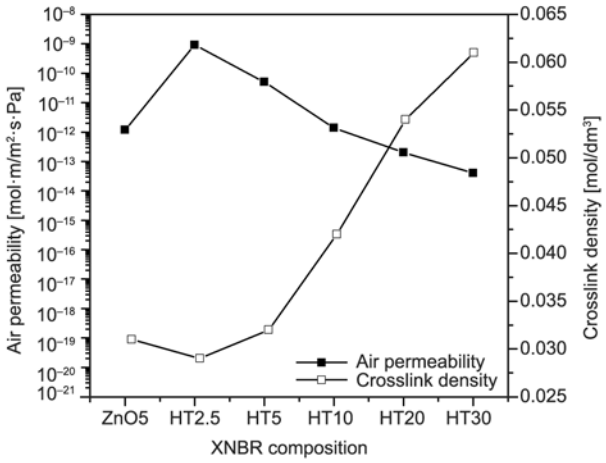

Figure 8. Dependence of air permeability and crosslink density on XNBR composition

Table 7. Mechanical properties of XNBR/HT composites

Sample name	SE_{100} [MPa]	SE_{200} [MPa]	SE_{300} [MPa]	TS [MPa]	EB [%]	F [N/mm]	v [mol/dm^3]
X	0.7	0.7	0.6	0.7	1401	3.1	–
XZnO5	1.4	1.9	2.3	19.0	500	6.3	0.031
XHT2.5	1.0	1.2	1.4	4.5	727	8.2	0.029
XHT5	1.2	1.7	2.3	8.4	688	9.2	0.032
XHT10	1.9	2.8	4.1	14.5	536	12.8	0.042
XHT20	2.5	4.3	6.4	16.0	542	12.6	0.054
XHT30	3.3	5.8	8.3	18.6	519	14.3	0.061

$SE_{100, 200, 300}$ – stress modulus at 100, 200 and 300% elongation, *TS* – tensile strength, *EB* – elongation at break, *F* – tear strength, *v* – crosslink density

rubber chains by hydrotalcite particles that results in reducing the diffusion of the gas molecules. Another reason may be that the impermeable hydrotalcite layers forced a tortuous pathway, which retarded the diffusion of the gas molecules [33].

3.7. Resistance to UV radiation

Table 8 summarizes the mechanical properties and crosslink densities of XNBR samples exposed to ultraviolet light. XNBR generally has poor resistance to ozone, UV radiation and weathering because double bonds are present in polybutadiene segment of the chemical backbone. Inorganic compounds, such as metal oxides provide effective UV screening. The presence of the layered double hydroxide enhanced UV stability of XNBR material compared with that of the corresponding gum rubber matrix or that crosslinked with zinc oxide, as the aging factor *K* increased gradually with the increase in the filler content. The effect was more pronounced for samples containing the highest concentration, 30 phr of HT. From the obtained data we may conclude that the addition of HT improves UV stability of XNBR composites.

3.8. Scanning electron microscopy analysis (SEM)

The micrographs of filler particles and XNBR composite containing 30 phr of HT obtained from scanning electron microscopy are shown in Figure 9a–9d. Figure 9b, shows that hydrotalcite is characterized by a layered structure and hexagonal-shaped particles with lateral dimensions of 50–400 nm. A high layer charge density makes LDH extremely difficult to exfoliate or delaminate into single sheets compared to cationic clays. However, because of the polar surface of LDH, a good compatibility with XNBR (containing polar groups such as nitrile, carboxyl), is expected. Moreover, dispersed HT particles may form strong bonds with rubber matrix, possibly through the chemical interaction between the acidic –COOH functionality of XNBR and the basic –OH groups on the layered metal hydroxide particle surface [5]. It is evident from Figure 9c, 9d that HT particles forms agglomerates with an average size of about 5 μm. It can be said that melt mixing of HT with rubber matrix does not provide good enough dispersion, as some agglomerates were detected, the state of HT dispersion is not uniform throughout the whole mass of rubber material. Because of high content of HT in rubber matrix (30 phr), which is necessary to obtain composites with high mechanical properties as well as great number of crosslinks, the problem of uniform distribution of HT particles in elastomer matrix appears.

4. Conclusions

In this study the effect of magnesium aluminum layered double hydroxide, also called hydrotalcite (MgAl-LDH, HT), on the crosslink reaction, mechanical and barrier properties of XNBR were examined. It was found that the HT effectively participates in the crosslinking reaction of XNBR and contributes to obtaining strong and stiff elastomeric composites. The dynamic mechanical analysis revealed a remarkable enhancement in the storage moduli and increase in glass transition temperature when HT is present in the XNBR matrix. The increase in crosslink density and the improvement in mechanical properties of XNBR/HT composites may result from the following types of interactions between: (a) acidic functionalities of XNBR and basic hydroxyl groups existing on the filler sheets, (b) polar functional groups of XNBR and polar surface of filler, (c) –COOH and metal ions provided

Table 8. Mechanical properties of XNBR/HT composites subjected to UV radiation

Sample name	SE_{100} [MPa]	SE_{200} [MPa]	SE_{300} [MPa]	TS [MPa]	EB [%]	K [–]	v [mol/dm^3]
X	0.9	0.9	0.9	1.2	1202	–	0.019
XZnO5	1.9	2.5	3.3	6.0	400	0.2	0.028
XHT2.5	1.5	1.7	2.0	2.8	510	0.2	0.049
XHT5	1.6	1.9	2.3	3.2	470	0.2	0.051
XHT10	2.0	2.7	3.8	5.3	460	0.3	0.066
XHT20	3.2	4.7	6.1	8.0	420	0.4	0.094
XHT30	3.8	5.6	7.2	11.1	480	0.6	0.107

$SE_{100, 200, 300}$ – stress modulus at 100, 200 and 300% elongation, *TS* – tensile strength, *EB* – elongation at break, *K* – aging coefficient, *v* – crosslink density.

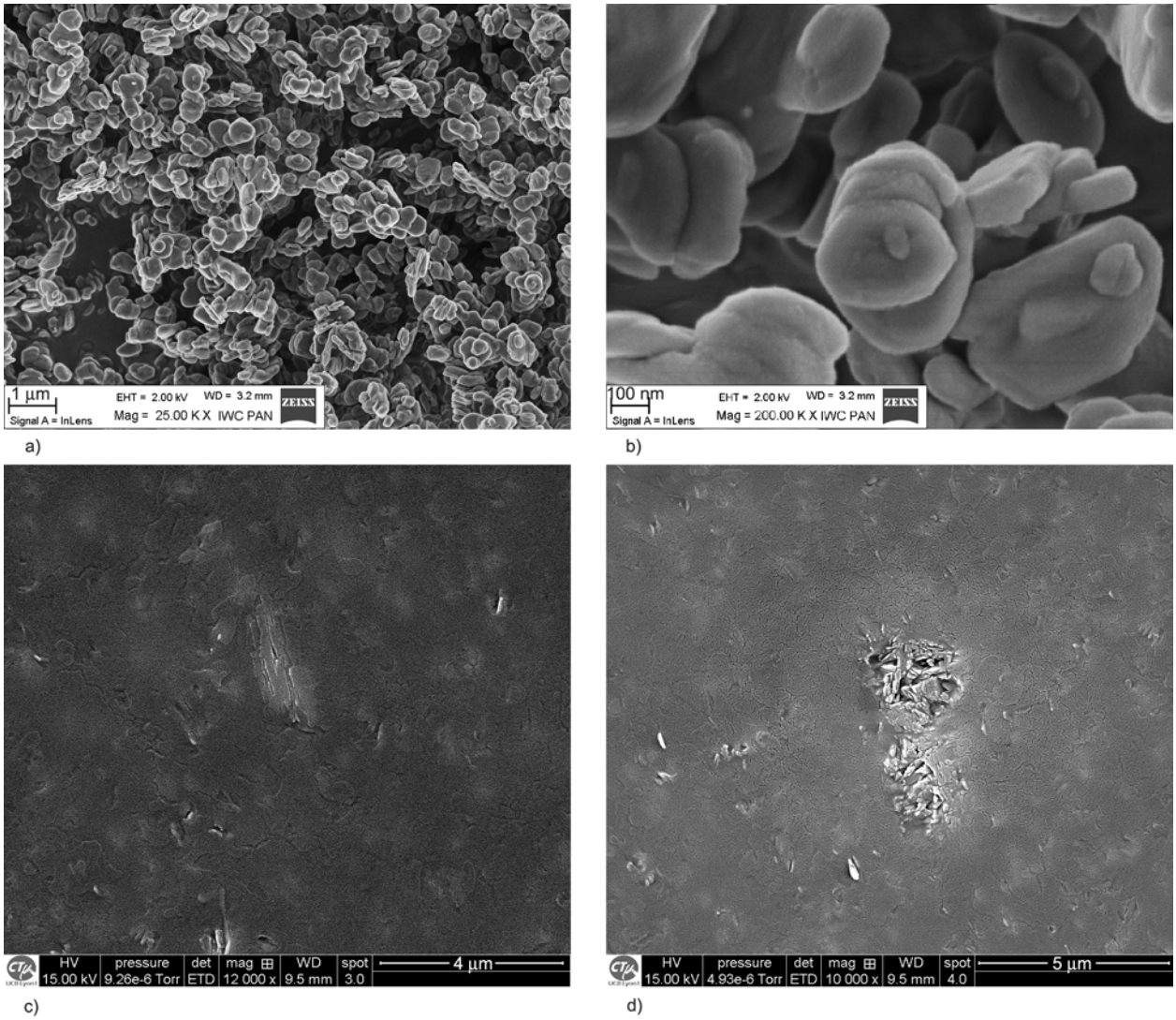

Figure 9. SEM micrographs of (a), (b) particles of hydrotalcite HT, (c), (d) XNBR composite with 30 phr of hydrotalcite HT

by HT (ionic bonds). The simultaneous application of HT as a curing agent and a filler may deliver not only an environmentally friendly, zinc oxide-free rubber product but also an ionic elastomer composite with excellent mechanical, barrier and transparent properties. However, obtaining material with aforementioned parameters requires high loadings of HT. Application of large amounts of an inexpensive and easily synthesized filler is economically beneficial due to the reduction of the cost of the final product.

Acknowledgements

The authors wish to acknowledge the Center of Electronic Microscopy of UCB Lyon 1 (Mr. Thierry Tamet & Mr. Pierre Alcouffe) for performing electronic microscopy analysis and also to Mr. Flavien Melis for his valuable suggestions and help.

References

[1] Brown H. P.: Carboxylic elastomers. Rubber Chemistry and Technology, **30**, 1347–1386 (1957). DOI: 10.5254/1.3542762

[2] Thakur V., Das A., Mahaling R. N., Rooj S., Gohs U., Wagenknecht U., Heinrich G.: Influence of layered double hydroxides on the curing of carboxylated nitrile rubber with zinc oxide. Macromolecular Materials and Engineering, **294**, 561–569 (2009). DOI: 10.1002/mame.200900083

[3] Ibarra L., Marcos-Fernández A., Alzorriz M.: Mechanistic approach to the curing of carboxylated nitrile rubber (XNBR) by zinc peroxide/zinc oxide. Polymer, **43**, 1649–1655 (2002). DOI: 10.1016/S0032-3861(01)00734-0

[4] Costa F. R., Pradhan S., Wagenknecht U., Bhowmick A. K., Heinrich G.: XNBR/LDH nanocomposites: Effect of vulcanization and organic modifier on nanofiller dispersion and strain-induced crystallization. Journal of Polymer Science Part B: Polymer Physics, **48**, 2302–2311 (2010).
DOI: 10.1002/polb.22116

[5] Pradhan S., Costa F. R., Wagenknecht U., Jehnichen D., Bhowmick A. K., Heinrich G.: Elastomer/LDH nanocomposites: Synthesis and studies on nanoparticle dispersion, mechanical properties and interfacial adhesion. European Polymer Journal, **44**, 3122–3132 (2008).
DOI: 10.1016/j.eurpolymj.2008.07.025

[6] Acharya H., Srivastava S. K., Bhowmick A. K.: Synthesis of partially exfoliated EPDM/LDH nanocomposites by solution intercalation: Structural characterization and properties. Composites Science and Technology, **67**, 2807–2816 (2007).
DOI: 10.1016/j.compscitech.2007.01.030

[7] Acharya H., Srivastava S. K., Bhowmick A. K.: A solution blending route to ethylene propylene diene terpolymer/layered double hydroxide nanocomposites. Nanoscale Research Letters, **2**, 1–5 (2006).
DOI: 10.1007/s11671-006-9020-x

[8] Kumar B., Rana S., Singh R. P.: Photo-oxidation of EPDM/layered double hydroxides composites: Influence of layered hydroxides and stabilizers. Express Polymer Letters, **1**, 748–754 (2007).
DOI: 10.3144/expresspolymlett.2007.103

[9] Wang D-Y., Das A., Leuteritz A., Mahaling R. N., Jehnichen D., Wagenknecht U., Heinrich G.: Structural characteristics and flammability of fire retarding EPDM/layered double hydroxide (LDH) nanocomposites. RSC Advances, **2**, 3927–3933 (2012).
DOI: 10.1039/C2RA20189E

[10] Das A., Wang D-Y., Leuteritz A., Subramaniam K. H., Greenwell C. H., Wagenknecht U., Heinrich G.: Preparation of zinc oxide free, transparent rubber nanocomposites using a layered double hydroxide filler. Journal of Materials Chemistry, **21**, 7194–7200 (2011).
DOI: 10.1039/C0JM03784B

[11] Das A., Costa F. R., Wagenknecht U., Heinrich G.: Nanocomposites based on chloroprene rubber: Effect of chemical nature and organic modification of nanoclay on the vulcanizate properties. European Polymer Journal, **44**, 3456–3465 (2008).
DOI: 10.1016/j.eurpolymj.2008.08.025

[12] Pradhan B., Srivastava S. K., Ananthakrishnan R., Saxena A.: Preparation and characterization of exfoliated layered double hydroxide/silicone rubber nanocomposites. Journal of Applied Polymer Science, **119**, 343–351 (2011).
DOI: 10.1002/app.32614

[13] Pradhan B., Srivastava S. K., Bhowmick A. K., Saxena A.: Effect of bilayered stearate ion-modified Mg-Al layered double hydroxide on the thermal and mechanical properties of silicone rubber nanocomposites. Polymer International, **61**, 458–465 (2012).
DOI: 10.1002/pi.3218

[14] Kotal M., Srivastava S. K.: Structure–property relationship of polyurethane/modified magnesium aluminium layered double hydroxide nanocomposites. International Journal of Plastics Technology, **15**, 61–68 (2011).
DOI: 10.1007/s12588-011-9006-0

[15] Guo S., Zhang C., Peng H., Wang W., Liu T.: Structural characterization, thermal and mechanical properties of polyurethane/CoAl layered double hydroxide nanocomposites prepared via *in situ* polymerization. Composites Science and Technology, **71**, 791–796 (2011).
DOI: 10.1016/j.compscitech.2010.12.001

[16] Kotal M., Srivastava S. K., Bhowmick A. K.: Thermoplastic polyurethane and nitrile butadiene rubber blends with layered double hydroxide nanocomposites by solution blending. Polymer International, **59**, 2–10 (2010).
DOI: 10.1002/pi.2686

[17] Das A., George J. J., Kutlu B., Leuteritz A., Wang D-Y., Rooj S., Jurk R., Rajeshbabu R., Stöckelhuber K. W., Galiatsatos V., Heinrich G.: A novel thermotropic elastomer based on highly-filled LDH-SSB composites. Macromolecular Rapid Communications, **33**, 337–342 (2012).
DOI: 10.1002/marc.201100735

[18] Reichle W. T.: Synthesis of anionic clay minerals (mixed metal hydroxides, hydrotalcite). Solid State Ionics, **22**, 135–141 (1986).
DOI: 10.1016/0167-2738(86)90067-6

[19] Leroux F., Besse J-P.: Polymer interleaved layered double hydroxide: A new emerging class of nanocomposites. Chemistry of Materials, **13**, 3507–3515 (2001).
DOI: 10.1021/cm0110268

[20] Xu Z. P., Zhang J., Adebajo M. O., Zhang H., Zhou C.: Catalytic applications of layered double hydroxides and derivatives. Applied Clay Science, **53**, 139–150 (2011).
DOI: 10.1016/j.clay.2011.02.007

[21] Cui W., Jiao Q., Zhao Y., Li H., Liu H., Zhou M.: Preparation of poly(ethylene terephthalate)/layered double hydroxide nanocomposites by *in-situ* polymerization and their thermal property. Express Polymer Letters, **6**, 485–493 (2012).
DOI: 10.3144/expresspolymlett.2012.51

[22] Heideman G., Noordermeer J. W. M., Datta R. N., van Baarle B.: Effect of zinc complexes as activator for sulfur vulcanization in various rubbers. Rubber Chemistry and Technology, **78**, 245–257 (2005).
DOI: 10.5254/1.3547881

[23] Flory P. J., Rehner J.: Statistical mechanics of cross-linked polymer networks II. Swelling. Journal of Chemical Physics, **11**, 521–526 (1943).
DOI: 10.1063/1.1723792

[24] Lenko D., Schlögl S., Temel A., Schaller R., Holzner A., Kern W.: Dual crosslinking of carboxylated nitrile butadiene rubber latex employing the thiol-ene photoreaction. Journal of Applied Polymer Science, **129**, 2735–2743 (2013).
DOI: 10.1002/APP.38983

[25] Zaborski M., Kosmalska A., Gulinski J.: Silica modified by use of organosilanes as a filler for carboxylate butadiene-acrylonitrile rubber. Kautschuk und Gummi Kunststoffe, **58**, 354–357 (2005).

[26] Przepiórkowska A., Chrońska K., Zaborski M.: Chrome-tanned leather shavings as a filler of butadiene–acrylonitrile rubber. Journal of Hazardous Materials, **141**, 252–257 (2007).
DOI: 10.1016/j.jhazmat.2006.06.136

[27] Eisenberg A., Hird B., Moore R. B.: A new multiplet-cluster model for the morphology of random ionomers. Macromolecules, **23**, 4098–4107 (1990).
DOI: 10.1021/ma00220a012

[28] Ibarra L., Rodríguez A., Mora-Barrantes I.: Crosslinking of carboxylated nitrile rubber (XNBR) induced by coordination with anhydrous copper sulfate. Polymer International, **58**, 218–226 (2009).
DOI: 10.1002/pi.2519

[29] Ibarra L., Alzorriz M.: Ionic elastomers based on carboxylated nitrile rubber and calcium oxide. Journal of Applied Polymer Science, **87**, 805–813 (2003).
DOI: 10.1002/app.11468

[30] Ibarra L., Alzorriz M.: Ionic elastomers based on carboxylated nitrile rubber (XNBR) and zinc peroxide: Influence of carboxylic group content on properties. Journal of Applied Polymer Science, **84**, 605–615 (2002).
DOI: 10.1002/app.10313

[31] Mandal U. K., Tripathy D. K., De S. K.: Dynamic mechanical spectroscopic studies on plasticization of an ionic elastomer based on carboxylated nitrile rubber by ammonia. Polymer, **37**, 5739–5742 (1996).
DOI: 10.1016/S0032-3861(96)00545-9

[32] Sahoo S., Bhowmick A. K.: Influence of ZnO nanoparticles on the cure characteristics and mechanical properties of carboxylated nitrile rubber. Journal of Applied Polymer Science, **106**, 3077–3083 (2007).
DOI: 10.1002/app.24832

[33] Zhang Y., Liu Q., Zhang Q., Lu Y.: Gas barrier properties of natural rubber/kaolin composites prepared by melt blending. Applied Clay Science, **50**, 255–259 (2010).
DOI: 10.1016/j.clay.2010.08.006

eXPRESS Polymer Letters Vol.8, No.6 (2014) 387–396
Available online at www.expresspolymlett.com
DOI: 10.3144/expresspolymlett.2014.43

Effect of different plasticizers on the properties of bio-based thermoplastic elastomer containing poly(lactic acid) and natural rubber

V. Tanrattanakul[*]*, P. Bunkaew*

Bioplastic Research Unit, Department of Materials Science and Technology, Faculty of Science, Prince of Songkla University, 90112 Songkla, Thailand

Received 5 November 2013; accepted in revised form 25 January 2014

Abstract. Bio-based thermoplastic elastomers (TPE) containing natural rubber and poly(lactic acid) were prepared by melt blending in an internal mixer. The blend ratio was 60% of natural rubber and 40% of poly(lactic acid). Dynamic vulcanization of natural rubber was performed with the sulfur system. The 2 mm – thick sheet samples were prepared by compression molding. The objective of this study was to investigate the effect of plasticization of PLA on the mechanical and physical properties of the derived TPE. Four plasticizers were selected: tributyl acetyl citrate (TBAC), tributyl citrate (TBC), glycerol triacetate (GTA), and triethyl-2-acetyl citrate (TEAC). The investigated properties were the tensile properties, tear strength, thermal ageing and ozone resistance, hardness, resilience, tension set and compression set. All plasticizers increased the strain at break. TBAC and TBC increased the stress at break. All plasticizers decreased the tear strength, hardness and resilience, and slightly changed the tension and compression set. TBAC seemed to be the best plasticizer for the TPE. The presence of 4 pph (parts per hundred resin) of plasticizer provided the highest strength and tensile toughness and the strain at break increased with the increasing plasticizer content. The plasticizers decreased the T_g and T_{cc} of the PLA and did not affect the degree of crystallinity of PLA in the TPE.

Keywords: *biopolymers, natural rubber, poly(lactic acid), polymer blend, thermoplastic elastomer*

1. Introduction

Bio-based polymers have recently been receiving much attention. These polymers or their monomers are derived from renewable resources and they could be biodegradable or non-biodegradable. Poly (lactic acid) or PLA is a well-known biodegradable, bio-based polymer. It has been widely used as a commodity plastic over past years. Lactic acid is the monomer for PLA and is derived from normal microbial fermentation process mainly from natural carbohydrates such as sugar or starch. Natural rubber (NR) is perhaps the oldest bio-polymer used for more than one hundred years. Although NR is mainly derived from the Hevea Rubber tree, it is not readily biodegradable. Research on the biodegradation of NR is being conducted by our research group. Recently, there was an article that reported the biodegradation of latex gloves prepared from vulcanized NR [1]. Thus a polymer blend between PLA and NR is interesting because this polymer blend is a totally bio-based polymer. Due to the brittleness of PLA, NR is used as a toughening agent for PLA [2–6]. PLA/NR blends in other forms have not been reported except from our group and we have reported on a thermoplastic natural rubber prepared from PLA and NR [7].

A thermoplastic elastomer (TPE) is an interesting polymer. It shows elastomeric properties at room

[*]Corresponding author, e-mail: varaporn.t@psu.ac.th

temperature and can be processed as a typical thermoplastic in the melting state. TPEs could be classified into 3 types based on preparation methods or chemical structure: (1) a triblock copolymer, (2) a thermoplastic polyurethane and (3) a polymer blend between thermoplastic and elastomer. When NR is used as the elastomer phase in type 3, this TPE is referred to as thermoplastic natural rubber (TPNR) or NR-based TPE. Generally, a typical thermoplastic has been made from polypropylene, polyethylene and polyamide and the elastomer phase has varied. In order to activate or accelerate biodegradation of NR-based TPE, a biodegradable plastic such as PLA should be employed. There are lots of publications of TPE and TPNR, but there has been no publication of a TPE prepared from a blend of PLA and NR except for the one publication [7]. This TPE could be referred to as a bio-based TPE. Generally NR in a TPE must be vulcanized during mechanical blending with the thermoplastic in order to obtain dispersed NR particles. It is still questionable that NR may be biodegradable because its backbone consists of only carbon-carbon double bonds and does not have ester linkages. Furthermore, a vulcanized NR might be more difficult to degrade due to it being crosslinked molecules. Our group is seeking to isolate some microorganisms with the potential to rapidly degrade NR and vulcanized NR. We believe that perhaps a PLA/NR bio-based TPE would be a polymer with a high possibility for biodegradation. Such a TPE would be useful for many applications. Biodegradation would perhaps first occur by removal of the PLA, then, hopefully, some microorganisms could attack the restructured NR phase.

A TPE made from PLA blended with NR shows a relatively low strain at break, i.e., less than 300%, because the PLA is a brittle plastic. The strain at break of PLA is ~5%. The conventional TPE is made from a ductile plastic such as polypropylene, polyethylene or nylon. As a result, its strain at break is higher than the TPE prepared from PLA. In order to increase the strain at break, modification of NR and PLA has been considered. It has been established that mastication of NR increases the strain at break of TPE [7]. The second approach was modifications to PLA. It was assumed that a ductile PLA could increase the strain at break of TPE because PLA exists as a continuous phase. A simple method for increasing the ductility of PLA is plasticization and there are many known plasticizers of PLA such as tributyl citrate (TBC) [8–13], tributyl acetyl citrate (TBAC) [8, 9, 13–15], triacetin or glycerol triacetate (GTA) [9, 11, 16] and triethyl acetyl citrate (TEAC) [8, 9, 17].

The objective of this study was to investigate the effect of plasticizers incorporated into PLA on the mechanical and physical properties of the PLA/NR TPE. Four plasticizers were selected including TBC, TEBC, TEAC and GTA. The effect of the plasticizer content was also evaluated. The characterization of TPEs was carried out by scanning electron microscopy, differential scanning calorimetry and dynamic mechanical thermal analysis.

2. Experimental

2.1. Materials

PLA Ingeo®4042D from NatureWorks LLC. (Minnetonka, MN, USA) and block NR (STR5CV60) from Jana Concentrated Latex Co. Ltd. (Songkhla, Thailand) were employed. Four types of plasticizers were selected: tributyl acetyl citrate (TBAC), tributyl citrate (TBC), triethyl acetyl citrate (TEAC) and glycerol triacetate (GTA). Their molecular weights are 402, 360, 318 and 218 g/mol, respectively. Their chemical structure was shown in Figure 1. All plasticizers were obtained from Sigma-Aldrich Inc. (Milwaukee, WI, USA) and used without treatment.

Commercial grade curatives for NR included sulfur, an accelerator, an activator and an antioxidant. All

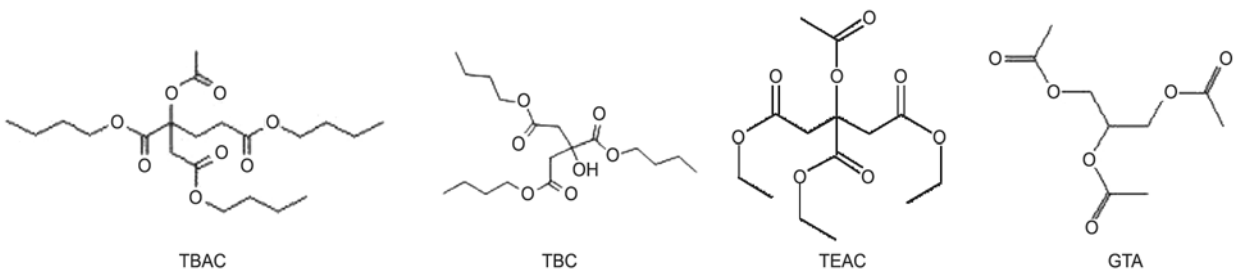

Figure 1. Chemical structure of plasticizers

Table 1. NR compounding formula

Chemical	Weight
NR	100
Stearic acid	2
Zinc oxide	5
Dibenzothiazyldisulphide (MBTS)	1.5
Antioixdant (Wingstay® L)	1
Sulfur	1

chemicals were commercial grades and used as received. NR compound formulation was tabulated in Table 1.

2.2. Sample preparation

Melt blending was carried out in an internal mixer (Brabender® Mixer 350E, Duisburg, Germany) with a rotor speed of 100 rpm at 155°C. The ratio between the PLA and NR was 40:60 by weight. The plasticizer was weighted according to parts per 100 parts of the blend (pph). The content of the curatives was based on the NR. NR was primarily loaded and masticated for 1 min before adding the PLA. The plasticizer was mixed with PLA before being loaded into the internal mixer. Curatives were added at the last step when a constant torque was obtained after adding PLA. The residence time in the internal mixer was 420–600 s. Compression molding was carried out (Kao Tieh (KT7014), Taipei, Taiwan) at 155°C under a pressure of 0.3 kg/m^2 for 420 s followed by a pressing at room temperature for 600 s to obtain a 2 mm thick sheet. The blends were kept in a desiccator before testing.

2.3. Testing of physical properties

All physical properties including the tensile properties, tear strength, tension set, compression set, thermal ageing and ozone resistance, hardness and resilience were carried out according to the ASTM listed in Table 2. The tensile properties, tear resistance and tension set were tested at a crosshead speed of 500 mm/min. The thermal ageing and ozone resistance were reported in terms of changes in the tensile properties after testing. The thermal aging resistance test was performed at 70°C for 7 days. The ozone exposure was carried out under a concentration of 50 parts per hundred million (pphm) at 40°C for 6 h. The percentage change (Δ) in the tensile properties (the tensile strength and the strain at break) was calculated according to Equation (1):

$$\Delta(\%) = \frac{A - O}{O} \cdot 100 \tag{1}$$

where O was the original value, and A was the value after ageing by heat or ozone. Increases are indicated as positive and decreases as negative. The tension set and the compression set were calculated according to Equations (2) and (3), respectively:

$$\text{Tension set [\%]} = 100 \cdot \frac{L_{1T} - L_{0T}}{L_{0T}} \tag{2}$$

$$\text{Compression set [\%]} = \frac{T_{0C} - T_{1C}}{T_{0C} - T_{2C}} \cdot 100 \tag{3}$$

where L_{0T} was the initial length (20 mm) before testing and L_{1T} was the length after testing. For the compression set test, T_{0C} was the initial thickness of the specimen (12.5 mm), T_{1C} was the specimen thickness after testing and T_{2C} was the thickness of a test bar (9.4 mm).

2.4. Material characterizations

Thermal analysis was conducted using a differential scanning calorimeter (DSC) (Perkin Elmer®DSC7, Norwalk, CT, USA) in a nitrogen atmosphere. The samples were heated from 30 to 100°C at a heating rate of 10°C/min. The heat of fusion of the pure crystalline PLLA (ΔH_c) was 93 J/g [2]. A Rheometric Scientific® DMTA V (Piscataway, NJ, USA) was used for determination of the dynamic mechanical thermal analysis (DMTA) under the following condition: frequency 1 Hz, heating rate 3°C/min, strain

Table 2. Mechanical and physical testing methods

Property	Test method	Equipment	Manufacturer
Tensile properties	ASTM D412 C	Instron®5569	Bucks, UK
Tear resistance	ASTM D624 C		
Tension set	ASTM D412		
Compression set	ASTM D395	Memmert®400 Air Oven	Schwabach, Germany
Thermal ageing resistance	ASTM D573	Tabai® gphh-200 Geer Oven	Taipei, Taiwan
Ozone resistance	ASTM D1149	Toyosieki® EG2001	Tokyo, Japan
Hardness Shore A	ASTM D2240	Shore Durameter® PTC408	New York, USA
Resilience (vertical rebound)	ASTM D2632	Shore Resiliometer®SRI74000	New York, USA

control 0.01% and dual cantilever mode. Scanning electron micrographs were recorded using a JEOL® JSM5800LV (Tokyo, Japan). All specimens were immersed in liquid nitrogen for 6 hr and immediately fractured prior to coating with gold. The NR and PLA on their fractured surfaces were etched by petroleum ether and dimethyl formamide, respectively.

3. Results and discussion

3.1. Effect of plasticizer type

3.1.1. Mechanical properties of bio-based TPE

In this section the plasticizer content was 4 pph. The tensile properties were the main criterion used to determine the effect of the plasticizer type on the mechanical properties of the present bio-based TPE. The stress-strain curves of TPEs with and without plasticizer are shown in Figure 2. Their tensile behavior looked similar to a typical thermoplastic elastomer such as a poly(styrene-isoprene-styrene) block copolymer [18], poly(styrene-butadiene/butylene-styrene) block copolymer [19], silicone rubber [20], PE/nitrile rubber TPE [21] and nylon-6/EPDM TPE [22]. The tensile strength or the stress at break and the strain at break of all TPEs are displayed in Figure 3. The TBAC and TBC increased the stress at break of TPE whereas the GTA decreased this property. TEAC had no effect on the stress at break of TPE. All plasticizers increased the strain at break. According to theory, plasticization causes a lower glass transition temperature (T_g) of the polymer matrix leading to an increase in flexibility and ductility. This was the reason for the enhancement of the strain at break. All plasticizers, except GTA, increased the tensile toughness of the TPE as indicated by the area under each stress-strain curve. TBAC, TBC and TEAC showed a high promise for increasing the tensile properties of TPE. According to Ljunberg and Wesslen [9] the solubility parameter of PLA was 20.1 $(J/cm^3)^{1/2}$ while Kaczmarek and Vuković-Kwiatkowska [23] reported this value was in the range of 19.28–21.73 $(J/cm^3)^{1/2}$. The solubility parameter of NR was 16.6 $(J/cm^3)^{1/2}$ [24]. The solubility parameter of the four plasticizers was in the range of 18.0–19.6 $(J/cm^3)^{1/2}$ [8, 9]. It should be noted that the solubility parameters of PLA and all plasticizers were in the same range. There is a contradiction in ranking of the solubility parameters of these plasticizers. They could be ranked as TEAC (19.6 $(J/cm^3)^{1/2}$) > TBC (18.8 $(J/cm^3)^{1/2}$) > TBAC (18.7 $(J/cm^3)^{1/2}$) [8], or as TBC (19.6 $(J/cm^3)^{1/2}$) > GTA (19.1 $(J/cm^3)^{1/2}$) > TEAC (18.9 $(J/cm^3)^{1/2}$) > TBAC (18.0 $(J/cm^3)^{1/2}$) [9]. The solubility of NR was lower than that of PLA and plasticizers, whereas the solubility of PLA and plasticizers were almost in the same range. This indicated that PLA should interact with plasticizers more than NR. The smallest solubility parameter of TBAC may result in the lower strain at break compared to the TPE containing TEAC and TBC. However, the rank of these solubility parameters cannot explain the lowest tensile properties of the TPE containing GTA. There are two possibilities that should be considered. Firstly, the plasticization effect of these plasticizers in TPE may not be straightforward because TPE was a polymer

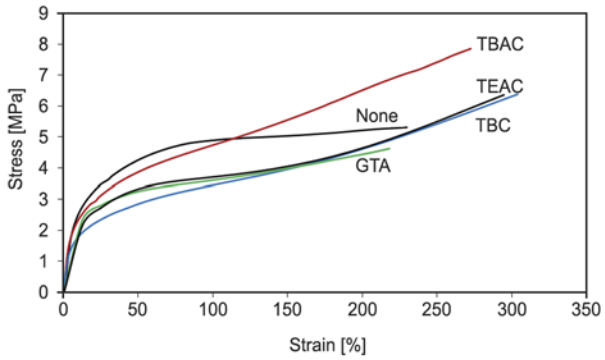

Figure 2. Stress-strain curves of TPE with and without plasticizer

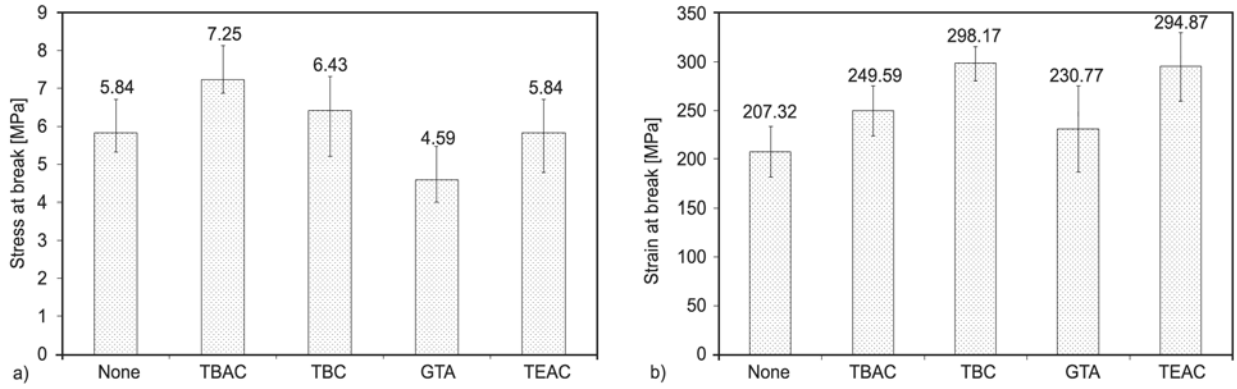

Figure 3. The effect of the plasticizer type on the tensile properties of TPE: (a) the stress at break; (b) the strain at break

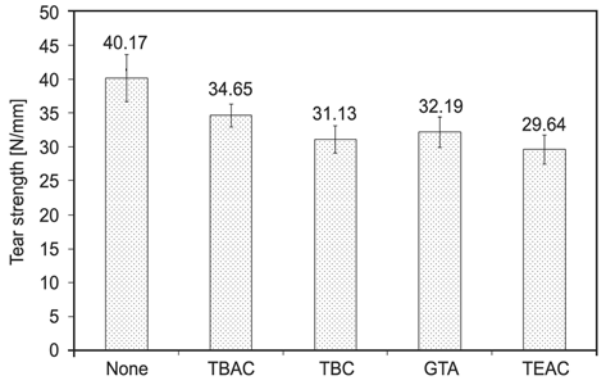

Figure 4. The effect of the plasticizer type on the tear strength of TPE

blend. The presence of the NR phase and the curing agents may interfere with the plasticization efficiency of the plasticizer. Secondly, the lowest molecular weight of GTA may cause the lowest intermolecular attraction of PLA leading to the lowest tensile strength and strain. The increment of the stress at break due to the plasticizer could be explained in view of the strain hardening of the plasticized PLA matrix as shown in Figure 2. A higher ductility and higher stress at break was obtained. GTA seemed to be the least effective plasticizer for TPE based on the tensile properties. All plasticizers decreased the tear strength as shown in Figure 4. The plasticized PLA was softer and its intermolecular attraction was reduced because of the penetration of the plasticizer molecules into the PLA matrix. This was attributed to a decrease in the tear strength when adding the plasticizer.

Table 3 represents the effect of the plasticizers on other physical properties of the TPE. Plasticization decreased the hardness Shore A and the resilience of TPE. There was no doubt that the lower hardness of TPE was derived by adding a plasticizer to the PLA matrix. The TPE containing TEAC showed a slight decrease in the hardness and that containing TBC showed a maximum decrease. Resilience is an interesting property of the elastomer. It indicates the ability of a build-up of heat or the damping characteristic of the elastomer. The lower resilience implied that TPE was able to absorb more energy. The increase in flexibility of the molecular backbone of PLA arising from the plasticization was attributed to more energy absorption. However, it is not acceptable to draw the conclusion that a high or low hardness/resilience is better because it depends on the applications for which it will be used. The tension set and compression set are physical properties that predict the elastomeric behavior of polymers. Both properties are a sign of the permanent or plastic deformations after tension or compression. Therefore, a low value is favorable for an elastomeric material. In the present study, the sample without plasticizer was used as a reference. An unchanged or lower value was the target. Based on this requirement, only TBAC was suitable for the present TPE. Remarkably, GTA increased the tension set of TPE while the other plasticizers decreased this property. This result indicated that GTA was not suitable for the present TPE.

Changes in the tensile properties after thermal and ozone ageing of TPE are tabulated in Table 4. These properties are important for polymers, especially for NR because its carbon-carbon double bond (C=C) is easily attacked by ozone. In theory there are two major types of molecular mechanisms occurring in polymeric molecules during thermal and ozone ageing: chain scission and crosslinking. It was not the aim of the present study to identify the degradation mechanisms. It was our objective to obtain the minimum change in both the positive and negative value. Although a positive value means an increase in the property, an increased value may not be desirable. Therefore, the least change in view of the absolute value compared with the TPE without plasticizer was considered. TBAC was the best plasticizer for thermal ageing and ozone resistance. Concern-

Table 3. The effect of plasticizers on the physical properties of TPE

Plasticizer (4 pph)	Hardness [Shore A]	Resilience [%]	Tension set [%]	Compression set [%]
None	75±3	45±0	14.00±2.0	95.9±1.3
TBAC	68±2	32±1	6.50±1.8	95.5±0.9
TBC	63±6	26±3	13.10±2.1	100.3±1.3
GTA	66±1	26±2	23.72±0.7	100.1±1.8
TEAC	73±2	26±2	10.00±1.5	109.5±0.6

Table 4. The effect of plasticizers on the thermal and ozone ageing resistance of TPE

Plasticizer (4 pph)	Thermal ageing		Ozone ageing	
	$\Delta\delta_b$ [%]	$\Delta\varepsilon_b$ [%]	$\Delta\delta_b$ [%]	$\Delta\varepsilon_b$ [%]
None	2.2	14.3	8.7	–26.5
TBAC	–8.5	14.7	–25.5	–6.2
TBC	–30.6	–29.3	–30.4	–27.8
GTA	12.4	19.9	–32.0	–84.3
TEAC	–30.8	–28.2	–25.0	–26.5

ing the resistance to thermal ageing, the change in the strain at break of the TBAC-sample was similar to that of the None-sample and its stress at break was decreased by less than 10%. All plasticizers led to a reduction in the stress at break in the range of –25 to –32% after ozone exposure. The TBAC-sample showed the least change in the strain at break (–6%) whereas the other samples had high reduction values such as –27 or –84%. Consequently, TBAC seemed to be the best plasticizer for the present TPE in terms of the mechanical properties of the TPE.

All plasticizers used in the present study had been already selected because they were known for their ability to plasticize PLA. The effect of these plasticizers on the transition temperature of PLA in the TPE was also established as described in the following section. Although these plasticizers did not affect the transition temperature of NR, their effect on the mechanical properties of NR in terms of the lubrication effect was also considered. The TPE in the present study was complex because there were two polymeric phases. Thus, the affinity between a plasticizer and each polymer (PLA and NR) and any interactions between the plasticizer and the curatives were our concern. This consideration needs to be studied in detail but it was not in the scope of the present study.

3.1.2. Characteristics of bio-based TPE

TPE behaves like an elastomer at room temperature and it can be melted like a thermoplastic. Therefore, TPE is widely used in the products need some rubber elasticity and can be thermally recycled or processed with thermoplastic equipment. The characteristics of TPE made from a polymer blend are primarily controlled by the blend morphology. Normally the plastic content is less than the rubber content for the preparation of TPE in order to receive the rubber characteristic. Theoretically the major component becomes a continuous phase in the polymer blend. In order to make a phase inversion in the present study, NR which was the major component became the dispersed phase by a dynamic vulcanization where NR became vulcanized during blending with PLA. Figure 5 confirmed the occurrence of the dynamic vulcanization. Dispersed NR particles were observed in the sample etched with dimethyl formamide, a good solvent for PLA and a non-solvent of NR (Figure 5a). Figure 5b represents the SEM micrograph of the sample etched with petroleum ether, a good solvent of NR. The continuous phase of PLA was remarkable and some crosslinked NR particles that were unable to be dissolved were also observed. Actually we also did a preliminary test to investigate the vulcanization of NR itself in the internal mixer. NR was able to undergo vulcanization under this blending condition. Furthermore, we had already determined the recyclability of the TPE, i.e., its ability to return to its original form (not shown here).

The thermal properties of TPE investigated by DSC are demonstrated in Figure 6. DSC thermograms were recorded from the first heating scan. A double melting peak of PLA was observed that was similar to the blend of PLA containing 10% of NR [2, 3]. Their glass transition temperature (T_g), cold crystallization temperature (T_{cc}) and melting temperatures

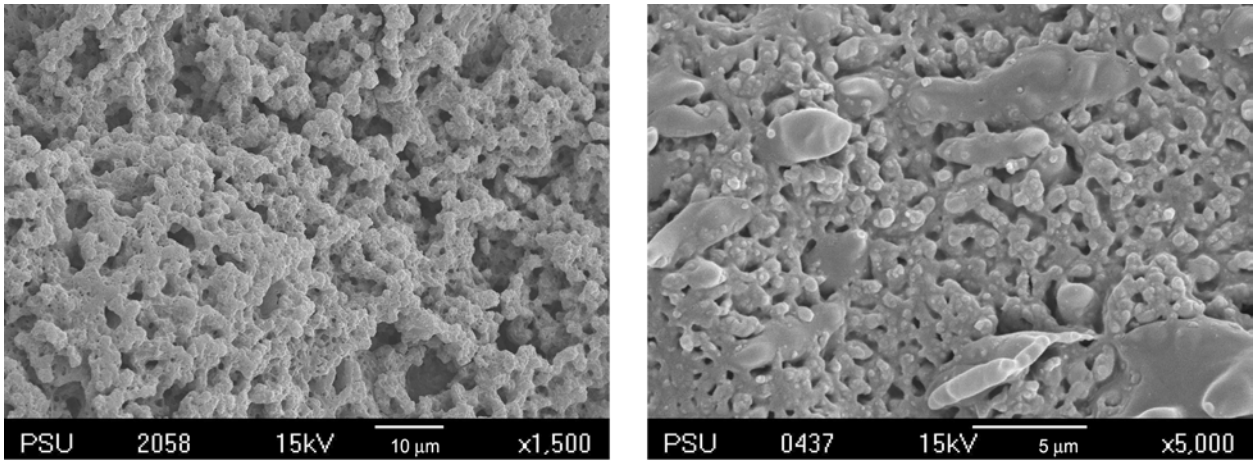

Figure 5. SEM micrographs of TPE: (a) etched with dimethyl formamide showing the NR particles; (b) etched with petroleum ether showing PLA continuous phase and some remained dispersed NR particles

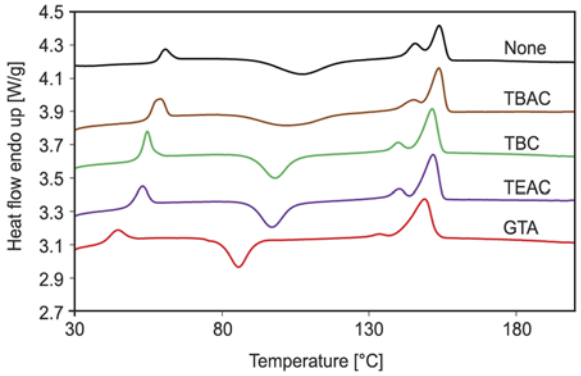

Figure 6. DSC thermograms of TPE with and without plasticizer

are listed in Table 5. All plasticizers significantly decreased the T_g and T_{cc} of PLA, and GTA showed the most effectiveness in plasticization because it produced the lowest T_g and T_{cc}. Only GTA seemed to influence the T_m of the PLA whereas the others showed only a slight decrease in the T_m. The degree of crystallinity of PLA did not change due to the plasticization, and their degree of crystallinity was in the range of 21–22%. The plasticizers enhanced the chain flexibility of PLA resulting in a faster cold crystallization process (lower T_{cc}). It was assumed that the cold crystallization contributed to the double melting peak. The lower melting peak belonged to the crystals from the cold crystallization process. The higher one was from the original crystals derived from the sample preparation. The significant drop in T_m by GTA implied the presence of smaller sized crystals or more defects in the crystals but the degree of crystallinity remained constant. It is generally known that short chain polymer can crystallize faster than long chain polymer but the crystals containing more chain ends in the crystalline structure could be a defect in its crystal and resulted in low T_m. The tension set in Table 2 was also evidence indicating more plastic deformation caused by the short chain PLA in the TPE containing GTA. This might have an impact on the low tensile strength of this TPE as well. It seemed that the molecular weight of the plasticizers had a strong effect on the T_g and T_{cc} of PLA. The lower the molecular weight of the plasticizer, the lower was the T_g and T_{cc} of the PLA. The lowest T_g of the TPE containing GTA may contribute to the lowest tensile strength and strain at break of the TPE.

Figure 7 exemplifies the temperature dependence of the loss tangent (tan δ) of the TPEs derived from DMTA. All TPEs showed two remarkable α transition temperatures that were equivalent to the T_g of NR and PLA and are listed in Table 4. Pure PLA had a T_g of 79.6°C and was in the same range as the T_g of PLA in the TPE without plasticizers (78.7°C). The T_g of the PLA phase in the TPE was much decreased by plasticization. In a similar observation to the DSC result, GTA yielded the lowest T_g of PLA. Although GTA provided the lowest T_g it did not provide better mechanical properties than other plasticizers. As a result, from the present study GTA was not the best plasticizer. The T_g of the NR phase did not change significantly. It showed a broad peak and the temperature was in the range of –56 to –52°C. This result substantiated the assumption that the plasticizers did not affect the thermal transition of NR. Obviously, the plasticizers increased the tan δ of the PLA phase and decreased that of NR phase. This behavior was related to the molecular weight of the plasticizers. The lower molecular weight pro-

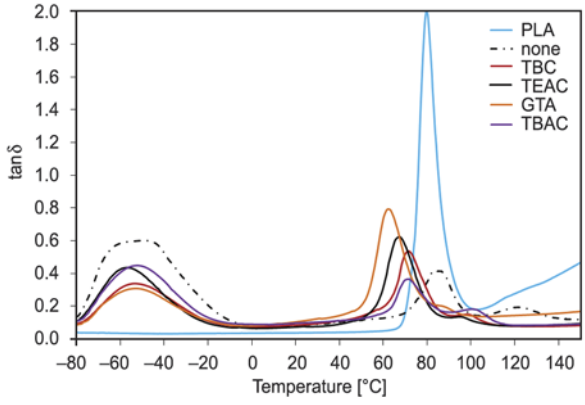

Figure 7. Loss tangent of TPE with and without plasticizer

Table 5. The effect of plasticizers on the transition temperature of TPE

Plasticizer (4 pph)	DSC[a]				DMTA	
	T_g [°C]	T_{cc} [°C]	T_m [°C]	% X_c	$T_{g\text{-}NR}$ [°C]	$T_{g\text{-}PLA}$ [°C]
None	60.5	106.8	145.5/153.8	21.42	–54.4	78.7
TBAC	58.8	101.3	145.1/153.6	21.60	–52.2	71.2
TBC	54.5	98.0	140.0/151.3	21.58	–53.7	71.3
GTA	44.3	85.5	133.3/148.8	22.14	–52.8	62.2
TEAC	52.8	96.8	140.1/151.6	22.39	–56.0	67.6

[a]Thermal properties of PLA phase

vided more changes. It should be noted that the PLA phase in TPE showed another transition temperature above its α transition (T_g) and this transition temperature shifted to a lower temperature after plasticization. This transition has also been seen in the PLA blended with 10% NR [2]. It might be involved with the cold crystallization process.

3.2. Effect of the plasticizer content

In this section, two plasticizers were selected for determination of the effect of the plasticizer content. TBAC was used because it provided the best properties. TBC was used for a cross check of the optimal content. Figure 8 shows the effect of the plasticizer content on the stress-strain curve of TPE and the mechanical properties of these TPEs are listed in Table 6. Obviously, 4 pph was the optimal content for both plasticizers. The strain at break of TPE increased with the increasing TBAC content. The modulus at 300% ($E_{300\%}$) or the stress at 300% strain appeared at a TBAC content ≥6 pph. The area under the stress-strain curve could be used to predict the energy absorbed for the material failure and designated as the tensile toughness. The 4 pph of TBAC provided the maximum tensile toughness and the maximum tear strength. The hardness of the TPE decreased with any further increase of the TBAC content while the resilience decreased when the TBAC content ≥6 pph (Table 7). The TBAC content did not show any significant effect on the tension set and the compression set of TPE. Although the 4 pph of TBAC provided the maximum strength and tensile toughness, it also produced the lowest strain at break. The 6–8 pph of TBAC would be appropriate for applications requiring $E_{300\%}$.

The effect of TBC on the tensile behavior of TPE was different from that of the TBAC. Deplasticization may occur in the sample containing 2 pph and this may have caused the lower tensile properties. The strain at break increased with the increasing TBC content, except at 4 and 6 pph when the values were the same. The stress at break was highest at 4 pph and, then, decreased with the increasing TBC content.

Table 6. The effect of the plasticizer content on the mechanical properties of TPE

Plasticizer content		$E_{300\%}$ [MPa]	σ_b [MPa]	ε_b [%]	Tear strength [N/mm]
None	0 pph	0.00	5.5±0.5	207±26	40.2±3.5
TBAC	2 pph	0.00	5.0±0.7	275±34	21.3±3.0
	4 pph	0.00	7.3±1.2	250±26	34.7±1.7
	6 pph	4.3±2.7	5.6±0.8	326±33	24.8±1.0
	8 pph	4.1±5.7	5.6±0.9	412±54	20.9±1.0
TBC	2 pph	0.00	4.1±0.6	114±7	29.4±3.4
	4 pph	0.00	6.4±0.6	298±18	31.1±2.0
	6 pph	0.00	5.4±0.8	281±42	26.2±2.3
	8 pph	3.6±0.2	4.5±0.8	413±37	24.5±1.8

Table 7. The effect of the TBAC content on the physical properties of TPE

TBAC content (pph)	Hardness [Shore A]	Resilience [%]	Tension set [%]	Compression set [%]
0	75±3	45±0	14.0±2.0	95.9±1.4
2	72±4	47±1	8.6±0.8	85.9±3.1
4	68±2	32±1	6.5±1.8	95.5±0.9
6	66±2	34±1	14.4±0.5	94.5±2.3
8	58±1	34±2	11.8±1.0	98.9±1.4

Table 8. The effect of the TBC content on the physical properties of TPE

TBC content (pph)	Hardness [Shore A]	Resilience [%]	Tension set [%]	Compression set [%]
0	75±3	45±0	14.0±2.0	95.9±1.3
2	73±2	43±2	11.4±1.0	90.1±2.1
4	63±6	26±3	13.1±6.1	100.3±1.3
6	65±2	24±0	8.9±1.4	93.2±3.5
8	63±4	28±3	13.3±1.7	98.7±3.8

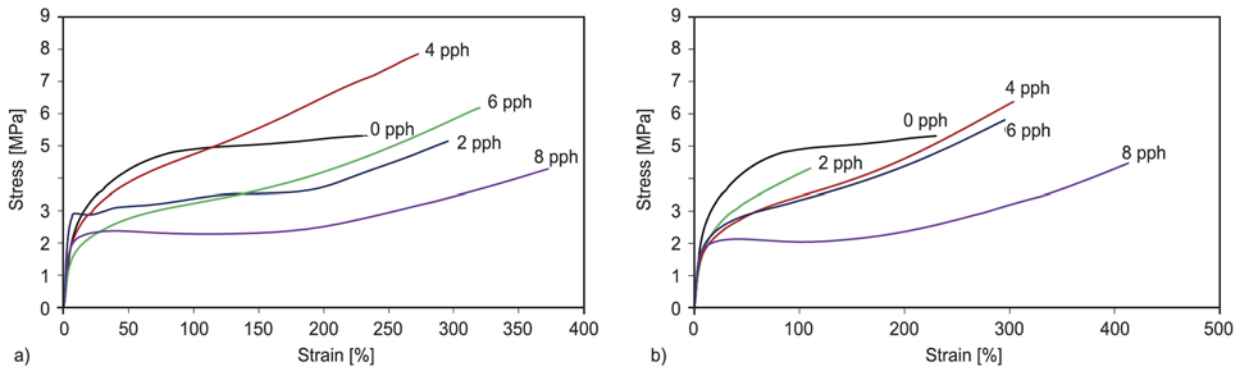

Figure 8. Stress-strain curves of TPE containing different plasticizer content: (a) TBAC; (b) TBC

It required a greater quantity of TBC than TBAC to obtain the strain at break >300%. The 2 pph of TBC slightly changed the hardness and resilience of TPE. These properties were decreased slightly and tended to be in the same range when the TBC content increased (Table 8). The TBC content also had a slight effect on the tension set and the compression set of TPE.

The experimental results indicated that the 4 pph of plasticizer offered the strongest and toughest TPE. Due to a variety of possible TPE applications, the specification of the mechanical and physical properties should be based on the product applications. For that reason, the plasticizer content could be ≥4 pph depending on the product specification.

4. Conclusions

A bio-based thermoplastic elastomer from PLA blended with NR was developed. Dynamic vulcanization took place during the melt blending and this was attributed to the phase inversion in the polymer blends. Thus the blends behaved as an elastomer in view of their mechanical and physical properties and as a thermoplastic due to their recyclability. Plasticization of PLA produced significant effects on the mechanical and physical properties of the TPE. It was required to plasticize PLA in order to obtain the modulus at 300% ($E_{300\%}$). All plasticizers increased the strain at break of TPE. The tensile strength of TPE, except for the one containing glyceral triacetate (GTA), also increased after plasticization. Changes in the mechanical and physical properties of TPE depended on the plasticizer type. Solubility parameter and molecular weight of plasticizers played a role on the tensile properties and transition temperature of TPE. The presence of plasticizer decreased the hardness, the resilience and the tear strength of TPE because of the increase in chain mobility/flexibility of PLA. Tributyl acetyl citrate (TBAC) was the best plasticizer used in the present study. The appropriate plasticizer content should be ≥4 pph depending on the desired properties.

Acknowledgements

This project is financially supported by National Innovation Agency Thailand (Grant no. BP33/52, Project no. C49-52) and the Faculty of Science Research Fund, Prince of Songkla University. Thanks to Dr. Brian Hodgson for assistance with the English.

References

[1] Watcharakul S., Umsakul K., Hodgson B., Chumeka W., Tanrattanakul V.: Biodegradation of a blended starch/natural rubber foam biopolymer and rubber gloves by *Streptomyces coelicolor* CH13. Electronic Journal of Biotechnology, **15**, 1–10 (2012).
DOI: 10.2225/vol15-issue1-fulltext-10

[2] Jaratrotkamjorn R., Khaokong C., Tanrattanakul V.: Toughness enhancement of poly(lactic acid) by melt blending with natural rubber. Journal of Applied Polymer Science, **124**, 5027–5036 (2102).
DOI: 10.1002/app.35617

[3] Chumeka W., Tanrattanakul V., Pilard J-F., Pasetto P.: Effect of poly(vinyl acetate) on mechanical properties and characteristics of poly(lactic acid)/natural rubber blends. Journal of Polymers and the Environment, **21**, 450–460 (2013).
DOI: 10.1007/s10924-012-0531-5

[4] Suksut B., Deeprasertkul C.: Effect of nucleating agents on physical properties of poly(lactic acid) and its blend with natural rubber. Journal of Polymers and the Environment, **19**, 288–296 (2011).
DOI: 10.1007/s10924-010-0278-9

[5] Bitinis N., Verdejo R., Cassagnau P., Lopez-Manchado M. A.: Structure and properties of polylactide/natural rubber blends. Materials Chemistry and Physics, **129**, 823–831 (2011).
DOI: 10.1016/j.matchemphys.2011.05.016

[6] Kowalczyk M., Piorkowska E.: Mechanisms of plastic deformation in biodegradable polylactide/poly(1,4-*cis*-isoprene) blends. Journal of Applied Polymer Science, **124**, 4579–4589 (2012).
DOI: 10.1002/app.35489

[7] Tanrattanakul V., Bunkaew P., Boonlong N.: Influence of rubber mastication on mechanical properties of poly(lactic acid)–based thermoplastic natural rubber. Journal of Biobased Materials and Bioenergy, **6**, 573–579 (2012).
DOI: 10.1166/jbmb.2012.1259

[8] Labrecque L. V., Kumar R. A., Davé V., Gross R. A., Mccarthy S. P.: Citrate esters as plasticizers for poly (lactic acid). Journal of Applied Polymer Science, **66**, 1507–1513 (1997).
DOI: 10.1002/(SICI)1097-4628(19971121)66:8<1507::AID-APP11>3.0.CO;2-0

[9] Ljungberg N., Wesslén B.: The effects of plasticizers on the dynamic mechanical and thermal properties of poly(lactic acid). Journal of Applied Polymer Science, **86**, 1227–1234 (2002).
DOI: 10.1002/app.11077

[10] Ljungberg N., Wesslén B.: Tributyl citrate oligomers as plasticizers for poly (lactic acid): Thermo-mechanical film properties and aging. Polymer, **44**, 7679–7688 (2003).
DOI: 10.1016/j.polymer.2003.09.055

[11] Ljungberg N., Andersson T., Wesslén B.: Film extrusion and film weldability of poly(lactic acid) plasticized with triacetine and tributyl citrate. Journal of Applied Polymer Science, **88**, 3239–3247 (2003). DOI: 10.1002/app.12106

[12] Ljungberg N., Wesslén B.: Preparation and properties of plasticized poly(lactic acid) films. Biomacromolecules, **6**, 1789–1796 (2005). DOI: 10.1021/bm050098f

[13] Harte I., Birkinshaw C., Jones E., Kennedy J., DeBarra E.: The effect of citrate ester plasticizers on the thermal and mechanical properties of poly(DL-lactide). Journal of Applied Polymer Science, **127**, 1997–2003 (2013). DOI: 10.1002/APP.37600

[14] Wang N., Zhang X., Ma X., Fang J.: Influence of carbon black on the properties of plasticized poly(lactic acid) composites. Polymer Degradation and Stability, **93**, 1044–1052 (2008). DOI: 10.1016/j.polymdegradstab.2008.03.023

[15] Höglund A., Hakkarainen M., Albertsson A-C.: Migration and hydrolysis of hydrophobic polylactide plasticizer. Biomacromolecules, **11**, 277–283 (2010). DOI: 10.1021/bm901157h

[16] Oksman K., Skrifvars M., Selin J-F.: Natural fibres as reinforcement in polylactic acid (PLA) composites. Composites Science and Technology, **63**, 1317–1324 (2003). DOI: 10.1016/S0266-3538(03)00103-9

[17] Zhang J-F., Sun X.: Physical characterization of coupled poly(lactic acid)/starch/maleic anhydride blends plasticized by acetyl triethyl citrate. Macromolecular Bioscience, **4**, 1053–1060 (2004). DOI: 10.1002/mabi.200400076

[18] Dair B. J., Honeker C. C., Alward D. B., Avgeropoulos A., Hadjichristidis N., Fetters L. J., Capel M., Thomas E. L.: Mechanical properties and deformation behavior of the double gyroid phase in unoriented thermoplastic elastomers. Macromolecules, **32**, 8145–8152 (1999). DOI: 10.1021/ma990666h

[19] Li Y., Shimizu H.: High-shear processing induced homogenous dispersion of pristine multiwalled carbon nanotubes in a thermoplastic elastomer. Polymer, **48**, 2203–2207 (2007). DOI: 10.1016/j.polymer.2007.02.066

[20] Frogley M. D., Ravich D., Wagner H. D.: Mechanical properties of carbon nanoparticle-reinforced elastomers. Composites Science and Technology, **63**, 1647–1654 (2003). DOI: 10.1016/S0266-3538(03)00066-6

[21] George J., Varughese K. T., Thomas S.: Dynamically vulcanised thermoplastic elastomer blends of polyethylene and nitrile rubber. Polymer, **41**, 1507–1517 (2000). DOI: 10.1016/S0032-3861(99)00302-X

[22] Oderkerk J., Groeninckx G., Soliman M.: Investigation of the deformation and recovery behavior of nylon-6/rubber thermoplastic vulcanizates on the molecular level by infrared-strain recovery measurements. Macromolecules, **35**, 3946–3954 (2002). DOI: 10.1021/ma010651v

[23] Kaczmarek H., Vuković-Kwiatkowska I.: Preparation and characterization of interpenetrating networks based on polyacrylates and poly(lactic acid). Express Polymer Letters, **6**, 78–94 (2012). DOI: 10.3144/expresspolymlett.2012.9

[24] Robeson L. M.: Polymer blends: A comprehensive review. Hanser, Munich (2007).

eXPRESS Polymer Letters Vol.8, No.6 (2014) 397–412
Available online at www.expresspolymlett.com
DOI: 10.3144/expresspolymlett.2014.44

Biodegradable polyester-based shape memory polymers: Concepts of (supra)molecular architecturing

J. Karger-Kocsis[1,2*], *S. Kéki*[3]

[1]Department of Polymer Engineering, Faculty of Mechanical Engineering, Budapest University of Technology and Economics, Műegyetem rkp. 3., H-1111 Budapest, Hungary
[2]MTA–BME Research Group for Composite Science and Technology, Műegyetem rkp. 3., H-1111 Budapest, Hungary
[3]Department of Applied Chemistry, University of Debrecen, Egyetem tér 1, H-4032 Debrecen, Hungary

Received 19 December 2013; accepted in revised form 25 January 2014

Abstract. Shape memory polymers (SMPs) are capable of memorizing one or more temporary shapes and recovering to the permanent shape upon an external stimulus that is usually heat. Biodegradable polymers are an emerging family within the SMPs. This minireview delivers an overlook on actual concepts of molecular and supramolecular architectures which are followed to tailor the shape memory (SM) properties of biodegradable polyesters. Because the underlying switching mechanisms of SM actions is either related to the glass transition (T_g) or melting temperatures (T_m), the related SMPs are classified as T_g- or T_m-activated ones. For fixing of the permanent shape various physical and chemical networks serve, which were also introduced and discussed. Beside of the structure developments in one-way, also those in two-way SM polyesters were considered. Adjustment of the switching temperature to that of the human body, acceleration of the shape recovery, enhancement of the recovery stress, controlled degradation, and recycling aspects were concluded as main targets for the future development of SM systems with biodegradable polyesters.

Keywords: *polymer synthesis, molecular engineering, smart polymers, biopolymers, biodegradable polymers*

1. Introduction

Shape memory (SM) biodegradable polymers (SMPs) and related composites are emerging smart materials in different applications. SMPs may adopt one (dual-shape), two (triple-shape) or several (multi-shape) stable temporary shapes and recover their permanent shape (or other temporary shapes in case of multi-shape versions) upon the action of an external stimulus. The external stimulus may be temperature, pH, water, light irradiation, redox condition etc. In most cases, however, the SMPs are thermally activated. The 'switching' or transformation temperature (T_{trans}), enabling the material to return to its permanent shape, is either linked with the glass transition (T_g) or with the melting temperature (T_m). Thus, SMPs are often subdivided based on their switch types into T_g- or T_m-based SMPs. As reversible 'switches' other mechanisms such as liquid crystallization and related transitions, supermolecular assembly/disassembly, irradiation-induced reversible network formation, formation and disruption of a percolation network, may also serve [1]. The permanent shape is guaranteed by physical or chemical network structures. The latter may be both on molecular and supramolecular levels. Linkages of these networks are termed net points. The temporary shape is created by mechanical deformation above T_{trans}. In some cases the deformation temperature may be below T_{trans} values (i.e. T_g- and T_m-linked temperatures) [2]. The macroscopic deformation applied is translated

*Corresponding author, e-mail: karger@pt.bme.hu

to conformational changes of the molecular chains, molecular segments of the networks or macroscopic deformation of the 'switching' phase. Temporary shape is fixed by maintaining the deformation via cooling causing vitrification and crystallization in T_g- and T_m-based SMP variants, respectively. The deformation energy, stored by this way, is released when the material is unloaded and reheated above T_{trans}. Note that $T_{trans} \geq T_g$ or T_m. Heating induces conformational rearrangements of the molecular chains and segments of the networks, melting of the crystals formed, release the constraints on macroscopically deformed phases, respectively, through which the permanent shape is restored. All what is described above is related to one-way SMPs. This means that the external stimulus activates only the change from the temporary to the permanent shape (dual-shape variant) or from one temporary to the other one in multi-shape SMPs. There are, however, two-way SMPs featuring a reversible shape change between the permanent and temporary shapes upon external stimulus.

Many works have been dealing with different SMPs, and the related knowledge is summarized in reviews and books [3–7]. SM properties are typically quantified by the shape fixity (R_f) and shape recovery ratios (R_r). R_f means the extent of fixing of the externally applied deformation in the temporary shape. Its value is 100% when the applied deformation, set above T_{trans}, is fully kept below T_{trans} in the temporary shape. R_r is the percentage of the recovery of the original shape when the material is reheated above T_{trans}. $R_r = 100\%$ when the original shape of the material is fully restored. SM properties are usually determined in cyclic (one or more) thermomechanical tests performed under stress- or strain-controlled conditions. A scheme of shape programming and recovery in a thermomechanical test is given in three-dimensional (3D) stress-deformation-temperature plot in Figure 1. Beside of R_f and R_r, further SM characteristics, such as the temperature interval of recovery, recovery rate and recovery force, can be measured. An excellent overview on the quantification of SM behavior in cyclic thermomechanical tests was compiled by Sauter *et al.* [8].

Environmental concerns and public interest for sustainable growth fuel the research and development (R&D) works to produce and use biodegradable and biobased polymers. Biodegradable means that the polymers decompose to carbon dioxide, water and

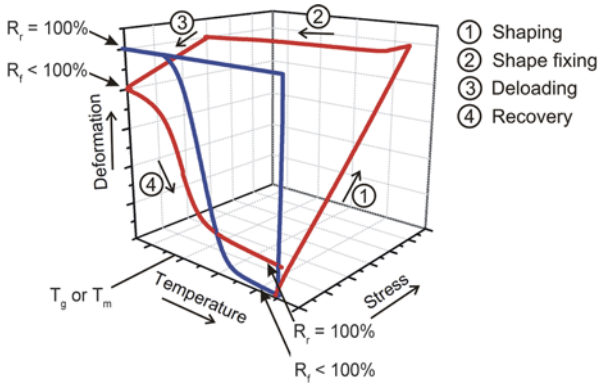

Figure 1. Single SM cycles of one-way (1W) SMPs in 3D plots, schematically. This figure also shows the reading of the R_f and R_r values

biomass under aerobic, while the decomposition products contain methane after decomposition in anaerobic conditions. Biobased polymers originate from biomass, synthesized by microorganisms or produced by biotechnological routes from monomers got from renewable resources. Biodegradable polymers can be produced from petrochemical sources, as well. Poly(ε-caprolactone) (PCL), polyesteramides, aliphatic- aromatic copolyesters belong to this category. Major part of biodegradable polymers are polyesters, and in particular, aliphatic polyesters. Monomers of the latter can be synthesized from renewable resources.

Biodegradable polymers, and especially polyesters, play a key role in medical applications due to their biodegradability and versatile syntheses resulting in tailored properties. SM biodegradable polyesters are predestinated for medical use because the related 'SM devices' (e.g. sutures, catheters, stents) should be present only temporarily in the human body. Their versatile synthesis is the premise of adjusting T_{trans} to the temperature of the body.

Next we shall give an overview on SMP systems which are composed fully or partly from biodegradable polyesters. This overlook is aimed at introducing the basic strategies of tailoring the (supra)molecular structures to meet the required performance.

2. One-way SMP (1W-SMP)

It is intuitive that to control the SM properties attention should be focused on the manipulation of the switching or fixing structures, or on both. The goals behind may be different: broadening or narrowing the temperature interval of the switching transition, reduction of the switch temperature (i.e. T_{trans}), enhancing the recovery force and speed, creation of

additional physical network, substitution of the physical network by a chemical one, generation of a temporary networks etc. Next we shall introduce the actual (supra)molecular design concepts for T_g- and T_m-based SM biodegradable polyesters. This survey concentrates on general strategies, which can be adapted to other SM polymer systems, rather to deliver a detailed listing of the related developments.

2.1. Molecular structure

2.1.1. T_g-based systems

The working principle of T_g-based SMPs is depicted schematically in Figure 2. As net points, remaining unaffected during deformation, molecular entanglements and entanglements along with crystalline domains act in linear (i.e. thermoplastic) amorphous and semicrystalline systems, respectively. The net points are structural units of the above physical networks.

Semicrystalline poly(L-lactic acid) (PLLA or PLA) exhibits T_g and T_m in the ranges of 60–70 and 150–170°C, respectively. In its uncrosslinked form the crystallites and entanglements act as net points. They can ensure, however, only moderate R_f and R_r data. Variation of the molecular weight (M_W), that affects both entanglement and crystallization, yielded limited success [9]. Incorporation of hydroxyapatite nanoparticles up to 50 wt% into poly(D,L-lactide) (PDLLA) resulted in improved R_r. The initial R_r value of PDLLA was enhanced from ca. 80 to 98% upon filling. This was attributed to H-bonding between the matrix and nanoparticles creating net points in an additional physical network-like structure [10, 11]. Accordingly, a more efficient network should be configured. Further, T_{trans} usually higher than T_g, is too high for biomedical applications and thus its reduction is essential. These two aspects are targets of the ongoing research. T_g is traditionally reduced by plasticizers. For this purpose water [12] and other plasticizers [13] were tried. To avoid the migration of the plasticizer, especially when added in high amount, it is straightforward to crosslink the PLA [13]. So, here we already see an example for the strategy to influence both the switches and net points simultaneously. This approach is quite frequent because manipulation of the switch phase is often accompanied with a change in the net points and vice verse. This change is not always wanted but appears as a necessary 'byproduct' of the design strategy followed. Just one example to underline the latter: the crystalline phase may diminish with

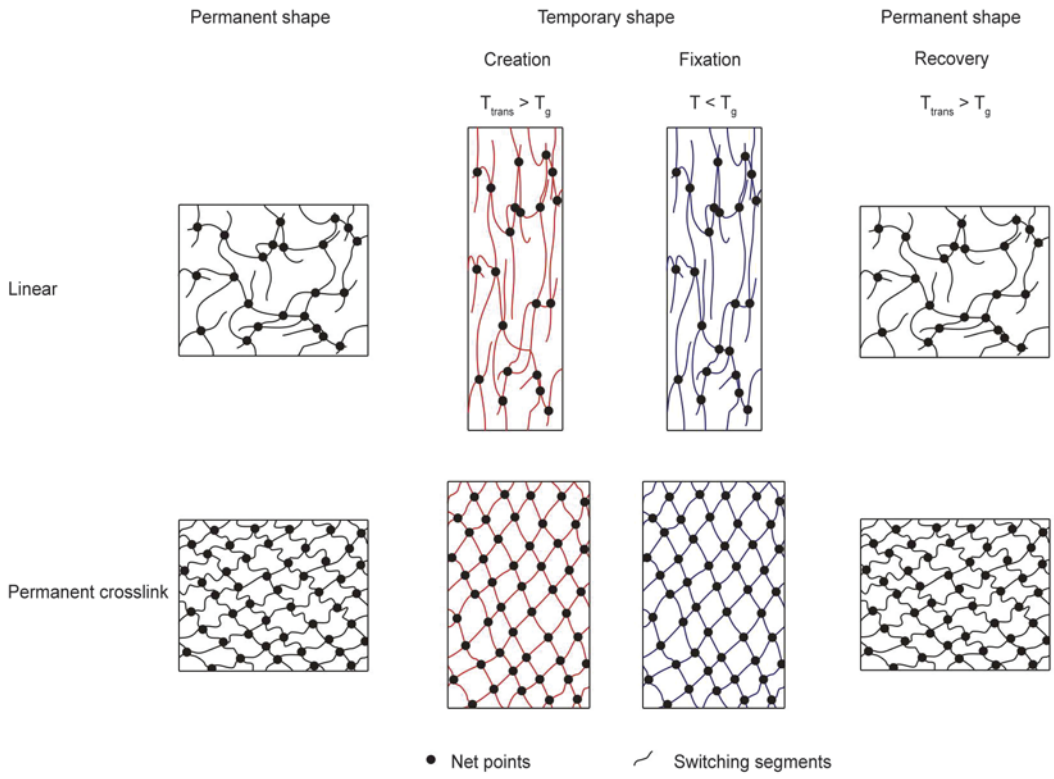

Figure 2. Molecular mechanisms of the thermally-induced 1W-SM effect in amorphous linear (thermoplastic) and crosslinked (thermoset) polymers. Note: temporary shape is created by tensile deformation

crosslinking whereby even a T_m- based SMP can be converted in a T_g-based one.

Plasticization is, however, not the best tool to manipulate T_g. Plasticizer may bleed out with the time, and facilitates the cold crystallization owing to T_g reduction, as well. This substantially affects the SM properties of T_g-based slow crystallizing polymers such as PLA. A far better method is to reduce the T_g is the synthesis of copolymers. Linear poly(L-lactide-co-ε-caprolactone)s (PLACLs) were produced by Lu *et al*. [14]. The lactide/lactone ratio was varied between 90/10 and 60/40 which was associated with a large change in the T_g (reduction from 54 to 14°C) and T_m, as well. Here again T_g adjustment was accompanied with a notable change in T_m. For shaping $T_{trans} = T_g + 15$°C, whereas for shape fixing $T = T_g - 15$°C were selected. R_f decreased, whereas R_r increased with increasing caprolactone content of the copolymer. Copolymerization may work also in the other direction, i.e. toward T_g enhancement. Poly(trimethylene carbonate) (PTMC) itself is an amorphous elastomer having a $T_g \sim -15$°C, which is very low for many SM applications. By copolymerization of TMC with D,L-lactides the T_g of the resulting copolymer (PTMC-DLLA) could be set between 11 and 44°C. As T_{trans} (= 37°C) > T_g (= 22°C) was used for shaping (elongation to 150%), and fixing occurred T = 0°C [15]. Several works were devoted to synthesize terpolymers composed of trimethylene carbonate, L-lactide and glycolide (PTMC-LLA-GA) [16].

Crosslinking is the favored way to 'stabilize' the network and its net points. Crosslinking usually brings further benefits with, such as high recovery stress and rate compared to the linear counterparts. The group of Lendlein functionalized oligomers composed of L-lactide and glycolide with UV-curable methacrylate end groups [17]. The comonomer ratio and length of the chain segments in the corresponding polymer (PLLA-GA) were varied in the experiments. The T_g values of the photocured random PLLA-GA copolymers were between T_g = 50–55°C. Instead of permanent crosslinks, introduced by various techniques (UV irradiation, high energy irradiation, peroxide), temporary ones can also be used. They may be – among others – photo- and thermoreversible ones. Diels-Alder type reactions are favored for thermoresponsive SMPs. The beauty of this approach is that the thermoreversible reaction allows us to recycle the corresponding polymer *via* remelting. As Diels-Alder reaction the cycloaddition, occurring between furan and maleimide groups, is preferred. This selection is due to the fact that the adduct forms and the retro Diels-Alder

Table 1. Selected concepts and their realization for T_g-based SM biodegradable polyesters. Designation: – not reported

Material, composition	Temporary shape, 'switching'		Permanent shape, 'fixing' network, net points	Concept, realization	Reference
	T_g [°C]	T_{trans} [°C]			
PLA (PLLA)	62–64	T_g + 15	crystalline domains + entanglements (physical network)	various M_W PLAs	9
PLA	49	< 227	entanglements (physical network)	simulation study: T_g manipulation by water uptake (< 2 wt%)	12
PLA	~ –50	–	permanent crosslinks (chemical network)	elastic PLA gel with high amount (< 40 wt%) of plasticizer, cured by electron beam. Swelling by plasticizer after crosslinking	13
PLACL	14–54	T_g + 15	crystalline domains + entanglements (physical network). At 40 wt% caprolactone content only entanglements	T_g reduction by copolymerization that reduced T_m, too. Copolymer at high caprolactone content amorphous	14
PTMC PTMC-DLLA	~ –15 11–44	– T_g + 15	entanglements (physical network) entanglements (physical network)	not suited for SM T_g increase via copolymerization	15
PTMC-LLA-GA	38–42	48	entanglements (physical network)	terpolymerization through compositional variations	16
PLLA-GA	50–55	–	permanent crosslinks by UV irradiation (chemical network)	crosslinking of oligo(L-lactide-*r*-glycolide)dimethacrylate. Crosslink density varied via the M_W of the monomers and their ratio	17
PLA	50–65	60– 100	temporary crosslinks (thermoreversible chemical network)	furan-functionalized PLA crosslinked with maleimide functional 'linkers' – Diels-Alder cycloaddition	18

reaction runs at rather low temperatures. Inoue *et al.* [18] reported that the Diels-Alder type crosslinking of properly functionalized PLA yields good SM properties. Recall that here T_{trans} (= 60–100°C) is still linked with the T_g for PLA. The SM function was lost when the material was heated to $T \sim 160$°C where the retro reaction, disconnecting the crosslinks, took place. The above strategies are summarized in Table 1.

2.1.2. T_m-based systems

In semicrystalline polymers T_m is linked with T_{trans}. To use the melting/recrystallization transition instead of the glass/rubbery one is beneficial since the former transition is 'sharper' (occurring in a smaller temperature range) and faster than the latter one. Similar to T_g-based SMPs, chemical (covalent or thermoreversible) or physical crosslinking (through phase segregated domains), and their combinations, may be the 'net points' which guarantee the permanent shape. The molecular mechanism, underlying the SM function in T_m-activated SMPs, is depicted schematically in Figure 3.

Accordingly, the polymer is heated above its T_m and deformed. The deformation induced temporary shape is fixed by cooling during which crystallizations takes place. T_m is never matched with the crystallization temperature (T_c) mostly due to the differently long molecular chains (undercooling effect). Recovery occurs after heating above T_m followed by cooling below T_c. Figure 3 also highlights that the initial crystalline structure may be not be completely restored after the SM cycle. This means a reduction in the R_r value.

Unlike PLA, the ductility of PCL is very high which predestinates it for SM applications. The T_g and T_m of PCL are at about –50 and 60°C, respectively. In order to make use of its T_m as T_{trans} PCL should be crosslinked by a suitable manner. Otherwise only the chain entanglements serve as net points. On the other hand, T_m of PCL is rather high for many biomedical applications and thus its reduction is the other major goal of R&D works.

Physical networks

A novel approach was recommended by Luo *et al.* [19] to 'strengthen' the physical network of PCL and thus improve its SM performance. The cited authors prepared inclusion complexes between α-cyclodextrin and PCL. Through this host-guest complexation a peculiar physical network has been created with 'naked' PCL segments as 'switches' and cyclodextrin-PCL inclusion complex domains as additional net points. A seldom used crosslinking technique is to create ionic clusters as net points through incorporation of ionic monomers in the main chain [20]. They can be, however, easily incorporated into polyesters in polycondensation reactions. The ionic aggregates may restrict the crystallization of the main chain or its segments. Consequently, creation of ionomers may be a reasonable approach to tune T_8 of semicrystalline SMPs.

Chemical networks

Permanent crosslinks in PCL were produced by sol-gel chemistry [21]. The related pathway contained the alkoxysilane end grouping of an α,ω-hydroxyl terminated PCL, followed by hydrolysis and poly-

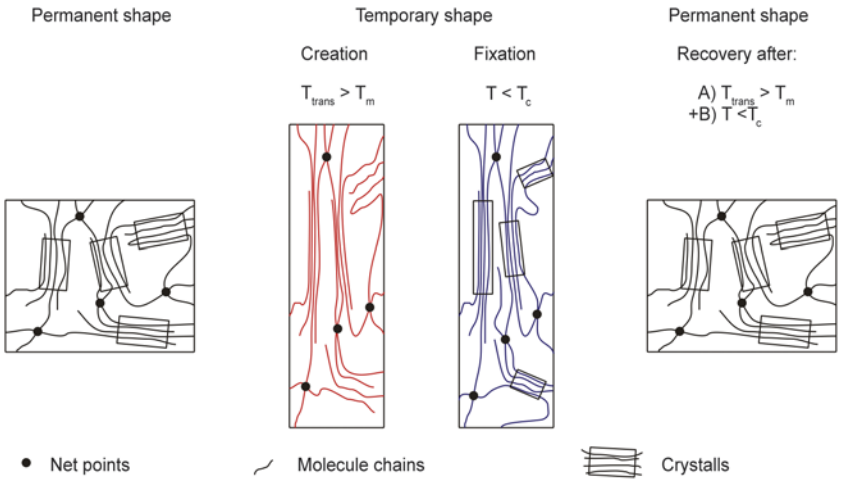

Figure 3. Molecular mechanisms of the thermally-induced SM effect in semicrystalline linear (thermoplastic) and crosslinked (thermoset) polymers. Note: temporary shape is created by tensile deformation

condensation reactions of the terminal alkoxysilane groups. The created chemical crosslinks maintained the crystallization ability of PCL. The T_m and crystallization temperature (T_c) of PCL were, however, affected by the crosslinking degree. This is a further demonstration that manipulation of the net points may affect the switching phase (and vice versa). The resulting material showed both one- and two-way SM behaviors. In a companion paper the same authors [22] prepared peroxide crosslinked PCL with different molecular architectures. In this case the PCL was terminated by methacrylate and crosslinked in its melt phase. Polyhedral silsesquioxane (POSS) containing PCL with acrylate end groups were also synthesized and photocrosslinked. Narendra Kumar *et al.* [23] elaborated a synthesis route for producing thermally and magnetically activated triple-shape memory polymers using methacrylate end functionalized crystallizable PCL (T_m = 55°C) and polyethylene glycol (PEG) (T_m = 38°C). The copolymer was cured by peroxide in presence and absence of silica coated magnetite nanoparticles. The outcome was a magnetically active SMP. For programming of the two temporary shapes the above T_m values were considered whereby adapting one- or two-step shape programming procedures. Peroxide crosslinked poly(propylene sebacate), synthesized from biorenewable resources, exhibited a T_m at about 50°C serving as T_{trans} in the SM cycle. The value of T_m could be tuned by the peroxide crosslinking and boehmite nanofillers content yielding a temperature interval between 37 and 51°C, which is close to the body temperature [24]. Schmidt [25] produced thermosets from oligomeric ε-caprolactone dimethacrylate and butyl acrylate by peroxide crosslinking. Into the network Fe_3O_4 nanoparticles were also embedded to trigger the SM function by electromagnetic activation. The magnetite particles in this case worked for the 'remote' control of the temperature by transforming the electromagnetic energy to heat. T_m of the PCL segments (43–49°C) was selected as T_{trans}.

UV-induced crosslinking is another possibility. ε-caprolactone diol oligomers can easily be converted into the related dimethacrylates which can be efficiently photocured [26]. During their SM programming T_m of the PCL segments served as T_{trans}. The latter could be changed between 30 and 50°C *via* the M_W of the PCL diol. The photosets showed excellent SM properties in multiple cycles. Thus, R_f = 86–97% and R_r = 92–97% data were measured after the 5th cycle. Crosslinkable functional groups may appear as end or side groups, and even in the main macromolecular chains. Garle *et al.* [27] modified PCL homo- and copolymers by cinnamate compound. The UV crosslinkable cinnamoyl side groups resulted in a crosslinked gel content of about 70 wt%. SM transformation was governed by T_m of the PCL segments.

The group of Nagata incorporated UV curable moieties directly into the main chain of the related polymers [28–31]. Thus, photocurable, biodegradable multiblock SMPs were prepared by polycondensation from PCL diol, PEG and 5-cinnamoyloxyisophthalic acid [28]. The latter compounds acted as UV crosslinker without any photoinitiator. The semicrystalline photosets exhibited $T_g \sim -60$°C, and T_m in the range of 35–47°C. Both R_f and R_r values were reported above 90% when selecting tensile deformation between 100 and 300% and T_{trans} =37–60°C. A similar strategy was followed to produce photocrosslinked PCL [29] and copolymers [30] composed of ε-caprolactone and L-lactide whereby incorporating coumarin groups in the man chain. The coumarin compound may participate in reversible crosslinking depending on the wavelength. Multiblock copolymers were also synthesized from PCL diol and PLA diol via polycondensation with cinnamic acid compound [31]. Again, the latter was responsible for reversible photocuring that did not affect the crystallization of PCL but reduced that of PLA. Choosing T_{trans} = 40–60°C, tensile elongations 100–500% and fixing temperature 22°C, R_f and R_r data between 88 and 100% have been measured. The authors emphasized that reversible photocrosslinking may be a promising way to produce light-sensitive SMPs.

Defize and coworkers [32, 33] used the Diels-Alder reaction to create temporary crosslinks. They synthesized star-shaped PCLs with furan, anthracene and maleimide end functionalities, respectively. The resulting SMPs showed excellent R_f and R_r values, even after 4 cycles, using T_m of the PCL as T_{trans} (= 65°C). The outstanding SM behavior was restored after recycling of the corresponding system. Note that recycling means here the onset of the retro Diels-Alder reaction running at $T \geq 105$°C. The anthracene end functionalization, instead of furan, was foreseen to influence the kinetics of the adduct formation and its temperature stability.

Apart from peroxide (free radical-induced) and photocrosslinking, radiation crosslinking methods can also be adapted. The Zhou and coworkers [34, 35] used γ-irradiation to crosslink PCL is presence and absence of various sensitizers and studied the SM behavior as a function of radiation dose and dosage rate. Recovery of the related PCLs were studied at $T = 56$°C. With increasing radiation dose the recovery temperature could be decreased due to a similar decrease in T_m. Introduction of polyfunctional polyester acrylates proved to be suitable additives to enhance the crosslinking degree of PCL upon γ-irradiation [35].

Copolymers

Copolymerization is the most widely used technique to control T_m and also to tune the biodegradability of polymers. Biobased polyesters composed of 1,3-propandiol, sebacic acid and itaconic acid in various ratios showed excellent SM properties after crosslinking with peroxide. T_{trans} could be tuned by the composition between 12 and 54°C [36]. Bacterial synthesis may yield semicrystalline polyhydroxyalkanoates of various compositions and various T_m data. Ishida *et al.* [37] have shown how a bacterial PHA, namely poly(3-hydroxyoctanoate-co-3-hydroxyundecanoate), can be crosslinked by POSS derivative making use of UV-assisted thiol-ene coupling. The thiol compounds were tetrathiol crosslinker and thiol functionalized POSS. The feasibility of Diels-Alder coupling was shown on the example of biodegradable polyester by Ninh and Bettinger [38]. In this case hyperbranched poly(glycerol-co-sebacate) with pendant furan groups was coupled with bifunctional maleimide crosslinker to produce an elastomeric material. POSS moieties may serve as crosslinking sites, as well. This material is, however, owing to its composition not a T_m- but a T_g-activated one.

'Graft' and multiblock copolymers, both in linear and crosslinked forms, may have excellent SM properties, as well. Linear, cyano functionalized polynorbornene having long PCL side chains showed good SM properties according to the report of Yang *et al*. [39]. This polynorbornene grafted by PCL along with the cyano groups in the main chain showed higher ductility and strength than the unmodified polynorbornene. Moreover, T_m of the phase separated PCL could be well used for T_{trans} in SM tests.

There are many possibilities to tailor the properties of SMPs via their block (segmented) architecture. Polyurethane (PU)-based systems are the most widely prepared and studied SMPs. Their development started in the 1990s by Hayashi, working for Mitsubishi Heavy Industries in Nagoya, Japan [40], and they are still in the focus of both industrial and academic interests [41]. This is, in particular, due to the highly versatile PU chemistry. The reason why we are mentioning them here is that the polyols used for PU synthesis are typically biodegradable polyester-based. The interested reader might have already noticed that the ε-caprolactone chemistry plays an important role in the reported polyester-related SMPs. PCL diols are traditional building blocks of PUs. Recently ε-caprolactone based oligomers with various molecular architectures became platform chemicals for PU and polyester syntheses [42]. The interest behind this development is due to the complete biodegradability, low T_g and relatively low T_m of PCL. PCL-based PUs are segmented polymers with excellent SM behaviors. The reaction of diisocyanate with low M_W diol chain extenders yields the 'hard', whereas the PCL chains give the 'soft' segments. Pioneering work in this field should be credited to Kim *et al*. [43]. It is generally accepted that the exceptional shape memory behavior of such PUs is related to their phase segregated morphology. For thermoplastic version the hard phase is responsible for memorizing the permanent, whereas the soft one for the temporary shape and its fixing [41, 43, 44]. As a consequence, T_{trans} is linked to the T_m of PCL. In crosslinked PUs, the crosslinked network guarantees the permanent shape and thus transitions related to the hard phase may also be involved in SM programming. The research on SM PUs has many similarities with that on SM polyesters. Peculiar attention was paid at the copolymer architecture. Enormous efforts have been dedicated to modify both soft and hard phases in order to improve the SM performance of both linear and crosslinked PU-based SMPs. For example, triple shape memory PU systems were produced recently by generating intermolecular H-bonds between carboxyl groups of the related PU chains and pyridine rings of cholesteryl isonicotinate mesogenic units. The SP PU itself contained PCL diol and thus one of the switch temperatures was the T_m of PCL. The other switch phase, having ca. 10°C higher temperature than T_m of PCL, was given by the domains

hold together by H-bonding. The R_f and R_r data of the latter was lower than those triggered by T_m of the PCL [45]. Note that this concept falls into the category of supramolecular assembly – see later.
Relevant strategies followed for T_m-based SMPs are listed in Table 2.

2.2. Supramolecular architecturing

Supramolecular structures are scaled above molecular level. Their constituents may be highly different nano- and micronsized entities, domains. The related structures involve nanodimensional molecular 'strings' (in some interpenetrating networks (IPNs)), disperse or continuous phases in micrometer range and even processing-induced higher order structures (skin-core or multilayer structures). The SM function of the related systems is further on T_g- or T_m-based. Scheme of the morphology of the related SMPs is given in Figure 4. The authors have to underline here that the above definition differs

Table 2. Selected concepts and their realization for T_m-based SM biodegradable polyesters. Designation: – not reported

Material, composition	Temporary shape, 'switching'		Permanent shape, 'fixing' network, net points	Concept, realization	Reference
	T_m [°C]	T_{trans} [°C]			
PCL	59	90	entanglements + inclusion complexes (physical network)	host-guest complexation with cyclodextrin in solution	19
Poly(oxyethylene-block-butylene adipate)	36–42	40	entanglements + ionic clusters (physical network)	ionomer copolymer formation via polycondensation	20
PCL	25–57	T_m + 40	permanent crosslinks (chemical network)	crosslinking of suitable end group functionalized PCLs through sol-gel chemistry and peroxide. Preparation of 1W- and 2W-SMPs	21, 22
PCL	20–40 (PEG), >50 (PCL)	40 and 70	permanent crosslinks – peroxide induced (chemical network)	conetwork formation using acrylate functionalized PCL and PEG. PCL and PEG segments crystallizable and exploited for triple-shape memory function – triggered thermally and magnetically	23
PCL	46–56	70	permanent crosslinks – free radical induced (chemical network)	crosslinking of oligo(ε-caprolactone) dimethacrylate; magnetically activated by incorporation of Fe_3O_4 nanoparticles	25
PCL	44–55	70	permanent crosslinks – UV irradiation (chemical network)	crosslinking of oligo(ε-caprolactone) dimethacrylate in presence and absence of photoinitiator	26
PCL	29–55	60	permanent crosslinks by UV irradiation without initiator (chemical network)	caprolactone functionalized with cinnamate group; random and block copolymers synthesized; T_m tuning by M_W of the caprolactone segments built in the network	27
PCL, PCL-LLA	35–47	37–60	permanent or temporary crosslinks by UV irradiation (chemical network)	crosslinking by photosensitive groups, covalently built in by polycondensation	28–31
PCL	44	65	temporary crosslinks (thermoreversible chemical network)	Diels-Alder reaction of star-shape PCL with furan and maleimide groups, effect of retro reaction on SM properties studied	32, 33
PCL	55–56	52–55	permanent crosslinks – γ-irradiation (chemical network)	crosslinking by high energy irradiation, also in presence of multifunctional sensitizer	34, 35
Poly(propylene sebacate) copolymers	42–54	T_m + 20	permanent crosslinks – peroxide induced (chemical network)	T_m depression by polycondensation via varied composition	36
SM PUs of different compositions and structures	depends on the actual T_m of the crystallizing segment (PLA-, PCL-based)	broad range above T_m	different physical and chemical networks	T_m reduction via crystallization in confined space, M_W change of the crystallizable diols, multiblock and supramolecular architectures…	41, 43–45

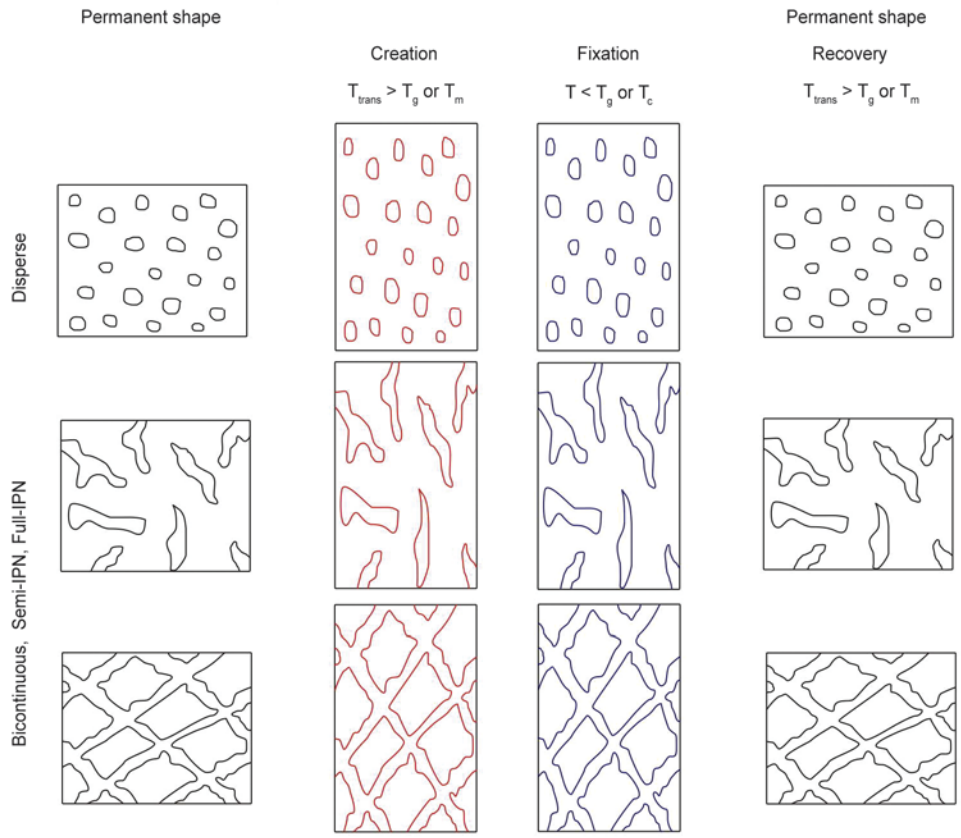

Figure 4. Scheme of the morphology changes during thermally-induced SM cycles in thermoplastic blends, semi and full IPN structures, respectively. Note: temporary shape is created by tensile deformation

from that one often used for supramolecular materials and supramolecular chemistry. Supramolecular chemistry deals with compounds with non-covalent bonds and interactions. Recall that our above classification covers a much broader range than that one of supramolecular chemistry.

2.2.1. Blends

Because PLA is highly brittle, it has been blended with numerous polymers to improve its toughness. A 'byproduct' of this research was the observation that some blends, in fact, showed SM feature. Lai and Lam [46] studied the SM performance of PLA/thermoplastic PU (TPU) blends at 70/30 and 50/50 compositions. TPU was found in dispersed form at 70/30 ratio, while a bicontinuous phase structure was concluded for the PLA/PU = 50/50. After deforming the specimens at T_{trans} = 25, 80 and 120°C, the recovery was assessed in the temperature range T = 20 to 160°C. Note that the selected T_{trans} data are below and above of the T_g of the PLA (ca. 80°C). R_f, R_r and the recovery stress strongly depended on T_{trans} and recovery temperatures. With increasing T_{trans} R_f increased while an adverse trend was observed for R_r. Zhang *et al.* [47] demonstrated SM behavior for PLA toughened by a polyamide-12 based elastomer, which was incorporated up to 30 wt%. For T_{trans} of the tensile loaded specimens room temperature was selected, which is in between the T_g of the polyamide elastomer ($T_g \sim -50$°C) and that of the PLA (T_g = 75°C). Recovery was triggered at temperatures above the T_g of PLA. TPU elastomer ($T_g \sim -35$°C) was blended with PLA in 10 wt% with and without multiwall carbon nanotubes (MWCNT) after various surface treatments [48]. The latter was introduced in 10 wt% to achieve electroresponsive SM. For temporary shaping T_g of PLA was considered. R_r decreased with increasing number of the electroactivated thermal cycles. This was attributed to the formation of 'frozen in' crystals in the dispersed PLA phase. PLA/PCL blends in the compositions range of 100/0 to 60/40 were produced with and without additional MWCNT by Amirian *et al.* [49]. The phase segregated blends exhibited two T_g and two T_m values. The latter increased with increasing amount of MWCNT. For $T_{trans} = T_g$(PLA) + 15°C, while for shape fixing T_g(PLA) – 15°C were chosen. R_r was measured at T = 70°C where the melting of PCL is also involved. As a consequence, both R_f and R_r decreased with

increasing PCL content of the blends. R_f was marginally affected, while R_r went through a maximum as a function of the MWCNT content (0–3 wt%) during the tensile deformation SM tests. PCL worked as efficient switching phase also in styrenic thermoplastic rubbers, such as styrene-butadiene-styrene block copolymer [50]. R_f increased steeply before leveling off above 30 wt% PCL content. An opposite tendency, almost a mirrored picture of the R_f course, was found for R_r as a function of the PCL content that was varied in the whole composition range. This behavior was traced to the actual morphology of the blends. As long as the thermoplastic rubber phase remained continuous excellent R_f and R_r data were measured.

Crosslinking is a useful tool to improve the SM behavior as already quoted. This technique has been adapted for PLA/PEG blends investigated in the range of 100/0 to 70/30. Crosslinking occurred by adding blocked polyisocyanate. T_g of the amorphous phase, composed of both PLA and PEG, served to select the T_{trans}. Both R_f and R_r increased with increasing amount of the polyisocyanate crosslinker. The crosslinking reduced also the recovery time of the corresponding blends [51].

The above treatise makes clear that acceptable SM properties can be achieved mostly by blend with bicontinuous phase structure (cf. Figure 4). The stabilization of the latter is, however, very challenging. It is the right place to mention that to distinguish between thermoset-containing semi IPN and IPN systems the term bicontinuous was used for thermoplastic blends.

2.2.2. Processing-induced structure

Radjabian *et al*. [52] used spun PLA filament, wound in helical form, for SM testing. The filament itself has a complex processing-induced supramolecular structure which does not change in the SM cycle. Thus, R_r did not change with T_{trans} (70–90°C), but remained still modest (~50%). By contrast, R_f deceased with increasing T_{trans}. Wang *et al.* [53] reinforced PLACL by *in situ* produced micro- and nanofibers from poly(glycolic acid) (PGA). The authors generated the PGA fibers in PLACL through in line extrusion stretching. Note that this method basically follows the microfibrillar composite concept of Fakirov ([54] and references therein). The lactide/lactone ratio of 82/18 resulted in an amorphous PLACL with a T_g of 22°C. For the temporary shape $T_{trans} = T_g + 15$°C, and for its fixing $T = T_g - 15$°C were selected. The PGA phase supported both shape fixing (restraining the molecular chain movement) and recovery (acting as additional net points).

Du *et al.* [55] investigated effects of layered architecture and blend morphology on the SM behavior using TPU and PCL. The TPU/PCL ratios set were 75/25, 50/50 and 25/75, respectively. The layered structure was achieved by a special multilayer coextrusion technique. The layer thickness varied with the composition ratio whereby keeping the number of layers and the overall thickness of the multilayer film as constants. T_m of PCL served as T_{trans} (= 70°C) during shape creation that was fixed at T = 21°C. R_f of the multilayer film was the higher the lower its PCL content was, and it changed as a function of the thermomechanical cycles only marginally. The TPU/PCL blend at 50/50 ratio outperformed the multilayer film with respect to R_f at the same PCL content. On the other hand, all other blends showed inferior R_f data to the multilayer film.

2.2.3. Supramolecular networks

Combination of crosslinkable resins with linear and crosslinkable biodegradable polyesters may result in various structures. Micron-scaled dispersion of the linear polyester in a crosslinked thermoset system is the usual prerequisite of toughness improvement of the latter. The dispersion is generated by phase separation upon curing. Such systems may show SM properties though this is not yet reported for systems with biodegradable polyesters. Far more interesting are, however, those systems which feature conetwork, semi interpenetrating (semi IPN) and full IPN structures.

Conetworks

Conetworks are chemically crosslinked networks in which none of the constituents forms a continuous phase. In ideal case the conetwork is on molecular level. Its formation is, however, often accompanied with ‘homocrosslinking’ and the related domains are on supramolecular level. That is the reason why we are treating them here. Conetworks differ markedly from the grafted IPN structure in which both phases are continuous and chemically coupled. Li *et al.* [56] prepared conetwork structured thermosets by the peroxide induced copolymerization of methyl methacrylate and PCL dimethacrylate.

The poly(methyl methacrylate)/CL ratio was varied between 80/20 and 20/80. The related systems exhibited a single T_g that changed as a function of composition in a broad range (T_g = 110…–20°C). The broad T_g relaxation may be used to memorize multiple shapes via careful programming. The authors showed that the related conetwork may show quadruple SM, i.e. 'remembering' to three temporary shapes. The prerequisite for that is that the energy stored in the partitioned T_g range during temporary shaping should be sufficient enough for shape fixing during cooling. Erden and Jana [57] modified SM PU with polybenzoxazine. The precured benzoxazine with its phenolic hydroxyl groups can react with the polyisocyanate whereby forming a conetwork with the polyurethane. Polybenzoxazine appeared in the PU matrix in phase segregated nanoscale domains. They can be treated as net points of a second fixing phase in addition to the hard segments of the PU. Cocrosslinking with benzoxazine shifted the T_g of the corresponding systems toward higher temperatures. At the same time the recovery stress was doubled compared to that of the reference PU. Enhancing the recovery stress is a very actual research direction to meet the demand of sensors and actuators.

Epoxy (EP)-PCL conetworks were produced by Lützen *et al*. [58]. Crystalline PCL domains, overtaking the role of 'switch' phase, were covalently integrated into the cationically polymerized EP network. The EP/PCL ratio has been varied between 85/15 and 60/40. After deformation at T_{trans} = 70°C and fixing at T = 20°C, R_f of 100% was measured.

Semi interpenetrating networks (semi IPNs)

Unlike conetworks, semi IPNs are composed of two continuous phases from which one is of thermoplastic nature. It is intuitive that the related entangled structure should contribute to the onset of SM properties. This was confirmed recently [59]. It is worth noting that entangling of the phases in semi and full IPN structures is never on molecular level though the materials may feature one single T_g [60]. 'Full' IPN denotes that both constituent continuous phases are crosslinked polymers. Semi IPNs may not only have SM, but also self healing properties. Though the term 'shape memory assisted self healing' was coined by the Rodriguez *et al*. [61], the concept should be credited to Karger-Kocsis as quoted by Yuan *et al*. [62].

The group of Rodriguez *et al*. [61] produced semi IPNs containing high M_W PCL as thermoplastic and tetrathiol crosslinked low M_W PCL diacrylate as thermoset phase. The linear/network PCL ratio was studied between 0/100 and 80/20. At 200% tensile deformation R_f increased slightly, whereas R_r decreased sharply with increasing amount of the thermoplastic PCL. Self healing was demonstrated on partially broken double edge notched tensile loaded specimens making use of the essential work of fracture protocol [63]. Healing happened by wetting, diffusion and randomization of the linear PCL component above its T_m, viz at T = 80°C.

Quasi semi IPN structure can be produced by other ways. Such a structure is given when electrospun PCL nanofiber mat is infiltrated by EP followed by curing of the latter. This material showed triple shape behavior. For setting the two temporary shapes T_m of PCL and T_g of EP served. T_g of EP was below the T_m of PCL [64]. Fejős *et al.* [65] not only confirmed this concept on the same material combination but compared the SM behavior with that of a 'real' semi IPN structured EP/PCL at the same composition (cf. Figure 5). The latter was generated in one-pot synthesis via phase segregation. The storage modulus *vs* temperature traces of the PCL nanoweb containing EP and semi IPN structured EP/PCL were similar (cf. Figure 6). The dynamic mechanical analysis (DMA) traces clearly show that both EP systems have a bicontinuous phase structure because their storage moduli do not drop at the T_g of EP which would happen for PCL dispersed in the EP matrix. Instead of that, the moduli

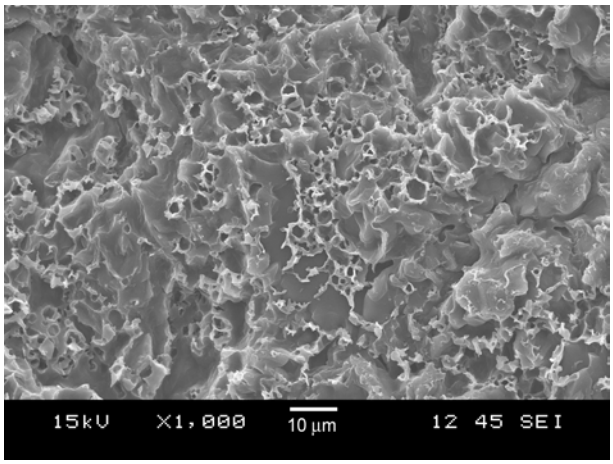

Figure 5. Etched (with methylene chloride) fracture surface of EP/PCL (= 77/23 wt%) displaying a semi IPN structure. Note: the lacy structure is due to the partially removed PCL phase

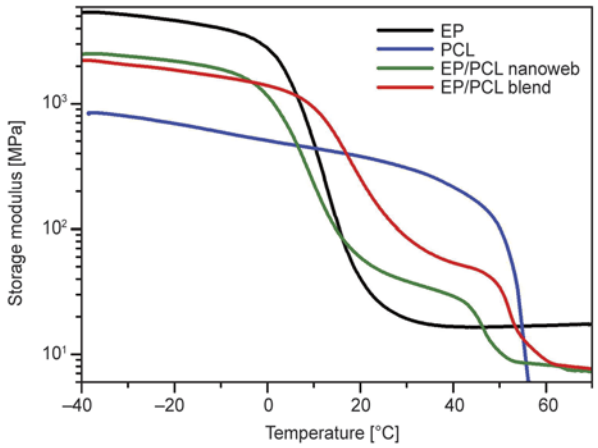

Figure 6. DMA traces (storage modulus vs temperature) of the EP with electrospun PCL nanoweb, semi IPN structured EP/PCL and the constituting PCL and EP. Notes: the PCL content in the EP/PCL combinations was 23 wt%.

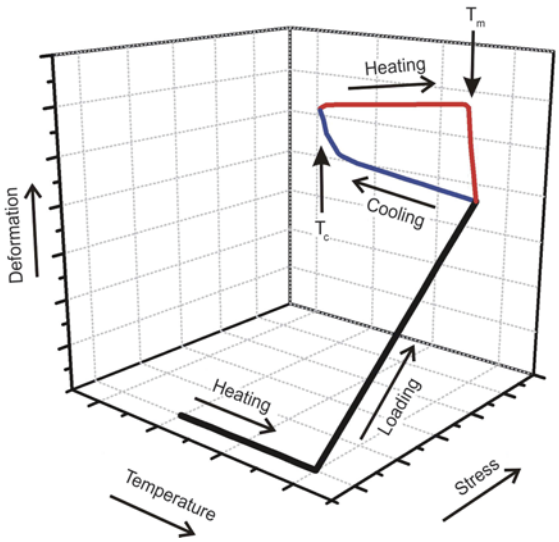

Figure 7. Single and multiple SM cycles of 2W-SMPs in 3D plots, schematically. Note that reversible shape change occurs between two temporary shapes whereby maintaining the stress.

run in between those of the PCL and EP. The SM properties of the EP/PCL with semi IPN structure were somewhat better than that with the electrospun PCL nanofiber mat. Note that the above semi IPN version should have self healing activity, which was, however, not yet tested.

Interpenetrating networks (IPNs)

Full IPN structured thermosets are also suitable SMP systems. It was shown by Zhang *et al.* [66]. The IPN structure was composed of crosslinked PU (PLGA-based diol crosslinked by polyisocyanate) and crosslinked PEG dimethacrylate (cured by UV irradiation). The content of the latter was varied between 0 and 50 wt%. The IPNs were amorphous and exhibited a rather broad T_g range (T_g between –23 and 63°C) that served for selection of T_{trans}. Both R_f and R_r data were reported over 93%. Kanazawa and Kawano filed a patent on electron beam crosslinked PLA/polystyrene having semi IPN or full IPN structures [67].

3. Two-way SMP (2W-SMP)

The 2W effect in bulk SMPs is linked with the presence of a reversible melting/crystallization switching segment. Accordingly, for 2W-SMPs $T_{trans} = T_m$. This is, however, only a necessary but not sufficient prerequisite. 2W-SMPs exhibit two distinct features compared to 1W-SMPs. First, the shape change occurs between two temporary ones. Second, to trigger the reversible shape change a certain stress should be steadily maintained. The preoriented chain segments crystallize upon cooling. This extends the specimen due to the crystallization heat released. Upon heating, the crystallites melt and the material contracts, shrinks. It is obvious that in order to meet the requirement, viz to return in the initial temporary shape during heating, the related structure should be crosslinked. In a linear system namely viscous flow would occur excluding the SM function. This, 2W-SMPs possess crosslinked (co)networks. During their design the network deformability should be adjusted to the deformation (in this case stress)-induced crystallization capability of the switch segments. This means that the M_W of the switching phase should be higher than that of the mean M_W between crosslinks. The SM cycle of a 2W-SMP is given in Figure 7. PCL-based 2W-SMPs were already produced and tested by Pandini and coworkers [21, 22].

Recently, another strategy was proposed to produce 2W-SM polymers. Behl *et al.* [68] suggested that creation of a special molecular conetwork (skeleton) containing reversible crystallizing/melting segments can overtake the job of external stress. Important prerequisites of this strategy are: presence of nanoscaled crystalline domains which are kept aligned by the skeleton network (thereby overtaking the role of external loading) and a broad melting range of the related crystallites. In the reversible shape change, i.e. extension upon cooling and contraction upon heating, only a given population of these crystals takes part. The concept has been

proven also for a conetwork composed of crystalline PCL (exhibiting a very broad melting range) and poly(n-butyl acrylate) having the necessary elasticity.

4. Conclusions

Biodegradable polyester-based SMPs are mostly used in and developed for applications in the human body (surgical sutures, catheters and stents). That is the reason why many R&D works addressed the adjustment of T_{trans}, related to T_m or T_g, respectively, to the body temperature. The other aspect, usually covered in the related research, is the biodegradability. Note that the SM characteristics are markedly reduced with the degradation time. This was shown on example of PCL-based systems degraded in vitro [69]. T_{trans} adjustment to body temperature and controlled biodegradability will remain preferred research topics further on [70]. Research on the SM behavior of bacterially synthesized aliphatic polyesters will be intensified.

There are, however, some general trends with SMPs. Nowadays considerable research efforts are undertaken to produce 1W multi-shape and 2W-SMP systems. Besides, ensuring multi-functionality (such as shape memory combined with self healing) become an emerging issue. Instead of direct thermal, many works are in progress to trigger the SM function by indirect heating via electric and magnetic fields. For this purpose suitable inorganic nanofillers are incorporated. The possibility of remote actuation will be extended for the SM performance of nanostructures such as electrospun nanofiber structures [71]. Chemically-induced SM functions, especially those triggered by water swelling and dissolution, will be investigated. SM hybrid composites will become under spot of interest [72]. Apart from experimental works, modeling and simulation studies will be increasingly performed. From the viewpoint of (supra)molecular design the following tendencies can be predicted:

Linear SMPs: creation of additional physical crosslinks through host-guest complexation and ionic clustering. For their realization researcher will adapt achievements from other fields, for example for ionic clustering the works on solid electrolytes may show the right directions [73]. Further attempts will be made to stabilize the bicontinuous structures of blends by adding nanofillers, polymeric coupling agents and even by selective crosslinking. Note that the latter means a transition toward semi IPN.

Crosslinked SMPs: conetworks, semi and full IPNs will become under spot of interest. They offer many benefits, such as enhanced recovery stress, broad T_g range, multiple T_g relaxations or T_m values (important for multi-shape programming). The non-polyester compounds in these crosslinked networks will be derived from renewable resources. So, petro-based EP will be replaced by epoxy functionalized plant oils [74]. Exploring various reversible crosslinking mechanisms, known under the heading of 'click chemistry', seems to be a very promising route.

Acknowledgements

The work reported here was supported by the Hungarian Research Fund (OTKA NK 83421) and by the TÁMOP-4.2.2.A-11/1/KONV-2012-0036 project co-financed by the European Union and the European Social Fund. This work was also supported by the European Union and the State of Hungary, co-financed by the European Social Fund, in the framework of TÁMOP-4.2.4.A/2-11/1-2012-0001 'National Excellence Program' (S. K.). The authors thank M. Fejős for her help in preparation of the artwork.

References

[1] Hu J., Zhu Y., Huang H., Lu J.: Recent advances in shape–memory polymers: Structure, mechanism, functionality, modeling and applications. Progress in Polymer Science, **37**, 1720–1763 (2012). DOI: 10.1016/j.progpolymsci.2012.06.001

[2] Sun L., Huang W. M., Wang C. C., Zhao Y., Ding Z., Purnawali H.: Optimization of the shape memory effect in shape memory polymers. Journal of Polymer Science Part A: Polymer Chemistry, **49**, 3574–3581 (2011). DOI: 10.1002/pola.24794

[3] Behl M., Razzaq M. Y., Lendlein A.: Multifunctional shape-memory polymers. Advanced Materials, **22**, 3388–3410 (2010). DOI: 10.1002/adma.200904447

[4] Mather P. T., Luo X., Rousseau I. A.: Shape memory polymer research. Annual Review of Materials Research, **39**, 445–471 (2009). DOI: 10.1146/annurev-matsci-082908-145419

[5] Xie T.: Recent advances in polymer shape memory. Polymer, **52**, 4985–5000 (2011). DOI: 10.1016/j.polymer.2011.08.003

[6] Huang W. M., Zhao Y., Wang C. C., Ding Z., Purnawali H., Tang C., Zhang J. L.: Thermo/chemo-responsive shape memory effect in polymers: a sketch of working mechanisms, fundamentals and optimization. Journal of Polymer Research, **19**, 9952/1–9952/34 (2012). DOI: 10.1007/s10965-012-9952-z

[7] Lendlein A.: Shape-memory polymers. Advances in Polymer Science. (ed. Lendlein A.) Springer, Berlin, Vol 226 (2010).
[8] Sauter T., Heuchel M., Kratz K., Lendlein A.: Quantifying the shape-memory effect of polymers by cyclic thermomechanical tests. Polymer Reviews, **53**, 6–40 (2013).
DOI: 10.1080/15583724.2012.756519
[9] Lu X. L., Cai W., Gao Z., Tang W. J.: Shape memory effects of poly(L-lactide) and its copolymer with poly (ε-caprolactone). Polymer Bulletin, **58**, 381–391 (2007).
DOI: 10.1007/s00289-006-0680-6
[10] Zheng X., Zhou S., Li X., Weng J.: Shape memory properties of poly(D,L-lactide)/hydroxyapatite composites. Biomaterials, **27**, 4288–4295 (2006).
DOI: 10.1016/j.biomaterials.2006.03.043
[11] Zhou S., Zheng X., Yu X., Wang J., Weng J., Li X., Feng B., Yin M.: Hydrogen bonding interaction of poly(D,L-lactide)/hydroxyapatite nanocomposites. Chemistry of Materials, **19**, 247–253 (2007).
DOI: 10.1021/cm0619398
[12] Ghobadi E., Heuchel M., Kratz K., Lendlein A.: Influence of the addition of water to amorphous switching domains on the simulated shape-memory properties of poly(L-lactide). Polymer, **54**, 4204–4211 (2013).
DOI: 10.1016/j.polymer.2013.05.064
[13] Kanazawa S.: Development of elastic polylactic acid material using electron beam radiation. SEI Technical Review: Sumitomo Electric, **66**, 50–54 (2008).
[14] Lu X. L., Cai W., Gao Z. Y.: Shape-memory behaviors of biodegradable poly(L-lactide-*co*-ε-caprolactone) copolymers. Journal of Applied Polymer Science, **108**, 1109–1115 (2008).
DOI: 10.1002/app.27703
[15] Yang J., Liu F., Yang L., Li S.: Hydrolytic and enzymatic degradation of poly(trimethylene carbonate-*co*-D,L-lactide) random copolymers with shape memory behavior. European Polymer Journal, **46**, 783–791 (2010).
DOI: 10.1016/j.eurpolymj.2009.12.017
[16] Zini E., Scandola M.: Shape memory behavior of novel (L-lactide-glycolide-trimethylene carbonate) terpolymers. Biomacromolecules, **8**, 3661–3667 (2007).
DOI: 10.1021/bm700773s
[17] Bertmer M., Buda A., Blomenkamp-Höfges I., Kelch S., Lendlein A.: Biodegradable shape-memory polymer networks: Characterization with solid-state NMR. Macromolecules, **38**, 3793–3799 (2005).
DOI: 10.1021/ma0501489
[18] Inoue K., Yamashiro M., Iji M.: Recyclable shape-memory polymer: Poly(lactic acid) crosslinked by a thermoreversible Diels–Alder reaction. Journal of Applied Polymer Science, **112**, 876–885 (2009).
DOI: 10.1002/app.29469
[19] Luo H., Liu Y., Yu Z., Zhang S., Li B.: Novel biodegradable shape memory material based on partial inclusion complex formation between α-cyclodextrin and poly(ε-caprolactone). Biomacromolecules, **9**, 2573–2577 (2008).
DOI: 10.1021/bm8004726
[20] Han S-I., Gu B. H., Nam K. H., Im S. J., Kim S. C., Im S. S.: Novel copolyester-based ionomer for a shape-memory biodegradable material. Polymer, **48**, 1830–1834 (2007).
DOI: 10.1016/j.polymer.2007.02.040
[21] Pandini S., Baldi F., Paderni K., Messori M., Toselli M., Pilati F., Gianoncelli A., Brisotto M., Bontempi E., Riccò T.: One-way and two-way shape memory behaviour of semi-crystalline networks based on sol–gel cross-linked poly(ε-caprolactone). Polymer, **54**, 4253–4265 (2013).
DOI: 10.1016/j.polymer.2013.06.016
[22] Pandini S., Passera S., Messori M., Paderni K., Toselli M., Gianoncelli A., Bontempi E., Riccò T.: Two-way reversible shape memory behaviour of crosslinked poly(ε-caprolactone). Polymer, **53**, 1915–1924 (2012).
DOI: 10.1016/j.polymer.2012.02.053
[23] Kumar U. N., Kratz K., Behl M., Lendlein A.: Shape-memory properties of magnetically active triple-shape nanocomposites based on a grafted polymer network with two crystallizable switching segments. Express Polymer Letters, **6**, 26–40 (2012).
DOI: 10.3144/expresspolymlett.2012.4
[24] Guo W., Kang H., Chen Y., Guo B., Zhang L.: Stronger and faster degradable biobased poly(propylene sebacate) as shape memory polymer by incorporating boehmite nanoplatelets. ACS Applied Materials and Interfaces, **4**, 4006–4014 (2012).
DOI: 10.1021/am300828u
[25] Schmidt A. M.: Electromagnetic activation of shape memory polymer networks containing magnetic nanoparticles. Macromolecular Rapid Communications, **27**, 1168–1172 (2006).
DOI: 10.1002/marc.200600225
[26] Lendlein A., Schmidt A. M., Schroeter M., Langer R.: Shape-memory polymer networks from oligo(ε-caprolactone)dimethacrylates. Journal of Polymer Science Part A: Polymer Chemistry, **43**, 1369–1381 (2005).
DOI: 10.1002/pola.20598
[27] Garle A., Kong S., Ojha U., Budhlall B. M.: Thermoresponsive semicrystalline poly(ε-caprolactone) networks: Exploiting cross-linking with cinnamoyl moieties to design polymers with tunable shape memory. ACS Applied Materials and Interfaces, **4**, 645–657 (2012).
DOI: 10.1021/am2011542
[28] Nagata M., Inaki K.: Biodegradable and photocurable multiblock copolymers with shape-memory properties from poly(ε-caprolactone) diol, poly(ethylene glycol), and 5-cinnamoyloxyisophthalic acid. Journal of Applied Polymer Science, **120**, 3556–3564 (2011).
DOI: 10.1002/app.33531
[29] Nagata M., Yamamoto Y.: Synthesis and characterization of photocrosslinked poly(ε-caprolactone)s showing shape-memory properties. Journal of Polymer Science Part A: Polymer Chemistry, **47**, 2422–2433 (2009).
DOI: 10.1002/pola.23333

[30] Nagata M., Yamamoto Y.: Photocurable shape-memory copolymers of ε-caprolactone and L-lactide. Macromolecular Chemistry and Physics, **211**, 1826–1835 (2010).
DOI: 10.1002/macp.201000106

[31] Nagata M., Sato Y.: Synthesis and properties of photocurable biodegradable multiblock copolymers based on poly(ε-caprolactone) and poly(L-lactide) segments. Journal of Polymer Science Part A: Polymer Chemistry, **43**, 2426–2439 (2005).
DOI: 10.1002/pola.20718

[32] Defize T., Riva R., Raquez J-M., Dubois P., Jérôme C., Alexandre M.: Thermoreversibly crosslinked poly(ε-caprolactone) as recyclable shape-memory polymer network. Macromolecular Rapid Communications, **32**, 1264–1269 (2011).
DOI: 10.1002/marc.201100250

[33] Defize T., Riva R., Jérôme C., Alexandre M.: Multifunctional multifunctional poly(ε-caprolactone)-forming networks by Diels–Alder cycloaddition: Effect of the adduct on the shape-memory properties. Macromolecular Chemistry and Physics, **213**, 187–197 (2012).
DOI: 10.1002/macp.201100408

[34] Zhu G., Liang G., Xu Q., Yu Q.: Shape-memory effects of radiation crosslinked poly(ε-caprolactone). Journal of Applied Polymer Science, **90**, 1589–1595 (2003).
DOI: 10.1002/app.12736

[35] Zhu G. M., Xu Q. Y., Liang G. Z., Zhou H. F.: Shape-memory behaviors of sensitizing radiation-crosslinked polycaprolactone with polyfunctional poly(ester acrylate). Journal of Applied Polymer Science, **95**, 634–639 (2005).
DOI: 10.1002/app.20989

[36] Guo B., Chen Y., Lei Y., Zhang L., Zhou W. Y., Rabie A. B. M., Zhao J.: Biobased poly(propylene sebacate) as shape memory polymer with tunable switching temperature for potential biomedical applications. Biomacromolecules, **12**, 1312–1321 (2011).
DOI: 10.1021/bm2000378

[37] Ishida K., Hortensius R., Luo X., Mather P. T.: Soft bacterial polyester-based shape memory nanocomposites featuring reconfigurable nanostructure. Journal of Polymer Science Part B: Polymer Physics, **50**, 387–393 (2012).
DOI: 10.1002/polb.23021

[38] Ninh C., Bettinger C. J.: Reconfigurable biodegradable shape-memory elastomers via Diels–Alder coupling. Biomacromolecules, **14**, 2162–2170 (2013).
DOI: 10.1021/bm4002602

[39] Yang D., Huang W., Yu J., Jiang J., Zhang L., Xie M.: A novel shape memory polynorbornene functionalized with poly(ε-caprolactone) side chain and cyano group through ring-opening metathesis polymerization. Polymer, **51**, 5100–5106 (2010).
DOI: 10.1016/j.polymer.2010.09.009

[40] Tobushi H., Hayashi S., Kojima S.: Mechanical properties of shape memory polymer of polyurethane series. JSME International Journal Series I, **35**, 296–302 (1992).

[41] Huang W. M., Yang B., Fu Y. Q.: Polyurethane shape memory polymers. CRC Press, Boca Raton (2012).

[42] Sisson A. L., Ekinci D., Lendlein A.: The contemporary role of ε-caprolactone chemistry to create advanced polymer architectures. Polymer, **54**, 4333–4350 (2013).
DOI: 10.1016/j.polymer.2013.04.045

[43] Kim B. K., Lee S. Y., Xu M.: Polyurethanes having shape memory effects. Polymer, **37**, 5781–5793 (1996).
DOI: 10.1016/s0032-3861(96)00442-9

[44] Ping P., Wang W., Chen X., Jing X.: The influence of hard-segments on two-phase structure and shape memory properties of PCL-based segmented polyurethanes. Journal of Polymer Science Part B: Polymer Physics, **45**, 557–570 (2007).
DOI: 10.1002/polb.20974

[45] Chen H., Liu Y., Gong T., Wang L., Zhao K., Zhou S.: Use of intermolecular hydrogen bonding to synthesize triple-shape memory supermolecular composites. RSC Advances, **3**, 7048–7056 (2013).
DOI: 10.1039/c3ra00091e

[46] Lai S-M., Lan Y-C.: Shape memory properties of melt-blended polylactic acid (PLA)/thermoplastic polyurethane (TPU) bio-based blends. Journal of Polymer Research, **20**, 140–148 (2013).
DOI: 10.1007/s10965-013-0140-6

[47] Zhang W., Chen L., Zhang Y.: Surprising shape-memory effect of polylactide resulted from toughening by polyamide elastomer. Polymer, **50**, 1311–1315 (2009).
DOI: 10.1016/j.polymer.2009.01.032

[48] Raja M., Ryu S. H., Shanmugharaj A. M.: Thermal, mechanical and electroactive shape memory properties of polyurethane (PU)/poly (lactic acid) (PLA)/CNT nanocomposites. European Polymer Journal, **49**, 3492–3500 (2013).
DOI: 10.1016/j.eurpolymj.2013.08.009

[49] Amirian M., Cai W., Chakoli A. N., Sui J., Feng J.: Shape memory properties of poly(L-lactide)/poly(ε-caprolactone) blends and their composites with carbon nanotubes. Journal of Materials Science and Engineering, **4**, 27–34 (2010).

[50] Zhang H., Wang H., Zhong W., Du Q.: A novel type of shape memory polymer blend and the shape memory mechanism. Polymer, **50**, 1596–1601 (2009).
DOI: 10.1016/j.polymer.2009.01.011

[51] Shen T., Lu M., Zhou D., Liang L.: Influence of blocked polyisocyanate on thermomechanical, shape memory and biodegradable properties of poly(lactic acid)/poly(ethylene glycol) blends. Iranian Polymer Journal, **21**, 317–323 (2012).
DOI: 10.1007/s13726-012-0031-4

[52] Radjabian M., Kish M. H., Mohammadi N.: Structure–property relationship for poly(lactic acid) (PLA) filaments: Physical, thermomechanical and shape memory characterization. Journal of Polymer Research, **19**, 9870/1–9870/10 (2012).
DOI: 10.1007/s10965-012-9870-0

[53] Wang L-S., Chen H-C., Xiong Z-C., Pang X-B., Xiong C-D.: A completely biodegradable poly[(L-lactide)-*co*-(ε-caprolactone)] elastomer reinforced by *in situ* poly(glycolic acid) fibrillation: Manufacturing and shape-memory effects. Macromolecular Materials and Engineering, **295**, 381–385 (2010).
DOI: 10.1002/mame.200900251

[54] Bhattacharyya D., Fakirov S.: Synthetic polymer-polymer composites. Hanser, Munich (2012).

[55] Du J., Armstrong S. R., Baer E.: *Co*-extruded multilayer shape memory materials: Comparing layered and blend architectures. Polymer, **54**, 5399–5407 (2013).
DOI: 10.1016/j.polymer.2013.07.012

[56] Li J., Liu T., Pan Y., Xia S., Zheng Z., Ding X., Peng Y.: A versatile polymer *co*-network with broadened glass transition showing adjustable multiple-shape memory effect. Macromolecular Chemistry and Physics, **213**, 2246–2252 (2012).
DOI: 10.1002/macp.201200231

[57] Erden N., Jana S. C.: Synthesis and characterization of shape-memory polyurethane–polybenzoxazine compounds. Macromolecular Chemistry and Physics, **214**, 1225–1237 (2013).
DOI: 10.1002/macp.201200315

[58] Lützen H., Gesing T. M., Kim B. K., Hartwig A.: Novel cationically polymerized epoxy/poly(ε-caprolactone) polymers showing a shape memory effect. Polymer, **53**, 6089–6095 (2012).
DOI: 10.1016/j.polymer.2012.10.033

[59] Ratna D., Karger-Kocsis J.: Shape memory polymer system of semi-interpenetrating network structure composed of crosslinked poly (methyl methacrylate) and poly(ethylene oxide). Polymer, **52**, 1063–1070 (2011).
DOI: 10.1016/j.polymer.2010.12.054

[60] Grishchuk S., Bonyár A., Elsäßer J., Wolynski A., Karger-Kocsis J., Wetzel B.: Toward reliable morphology assessment of thermosets via physical etching: Vinyl ester resin as an example. Express Polymer Letters, **7**, 407–415 (2013).
DOI: 10.3144/expresspolymlett.2013.38

[61] Rodriguez E. D., Luo X., Mather P. T.: Linear/network poly(ε-caprolactone) blends exhibiting shape memory assisted self-healing (SMASH). ACS Applied Materials and Interfaces, **3**, 152–161 (2011).
DOI: 10.1021/am101012c

[62] Yuan Y. C., Yin T., Rong M. Z., Zhang M. Q.: Self healing in polymers and polymer composites. Concepts, realization and outlook: A review. Express Polymer Letters, **2**, 238–250 (2008).
DOI: 10.3144/expresspolymlett.2008.29

[63] Bárány T., Czigány T., Karger-Kocsis J.: Application of the essential work of fracture (EWF) concept for polymers, related blends and composites: A review. Progress in Polymer Science, **35**, 1257–1287 (2010).
DOI: 10.1016/j.progpolymsci.2010.07.001

[64] Luo X., Mather P. T.: Triple-shape polymeric composites (TSPCs). Advanced Functional Materials, **20**, 2649–2656 (2010).
DOI: 10.1002/adfm.201000052

[65] Fejős M., Molnár K., Karger-Kocsis J.: Epoxy/polycaprolactone systems with triple-shape memory effect: Electrospun nanoweb with and without graphene versus *co*-continuous morphology. Materials, **6**, 4489–4504 (2013).
DOI: 10.3390/ma6104489

[66] Zhang S., Feng Y., Zhang L., Sun J., Xu X., Xu Y.: Novel interpenetrating networks with shape-memory properties. Journal of Polymer Science Part A: Polymer Chemistry, **45**, 768–775 (2007).
DOI: 10.1002/pola.21832

[67] Kanazawa S., Kawano K.: Method for producing crosslinked molded article of polylactic acid, and crosslinked molded article of polylactic acid. JP 2007182484, Japan (2007).

[68] Behl M., Kratz K., Noechel U., Sauter T., Lendlein A.: Temperature-memory polymer actuators. Proceedings of the National Academy of Sciences of the United States of America, **110**, 12555–12559 (2014).
DOI: 10.1073/pnas.1301895110

[69] Yu X., Zhou S., Zheng X., Xiao Y., Guo T.: Influence of *in vitro* degradation of a biodegradable nanocomposite on its shape memory effect. The Journal of Physical Chemistry C, **113**, 17630–17635 (2009).
DOI: 10.1021/jp9022986

[70] Díaz-Celorio E., Franco L., Puiggalí J.: Influence of microstructure on the crystallization of segmented copolymers constituted by glycolide and trimethylene carbonate units. Express Polymer Letters, **7**, 186–198 (2013).
DOI: 10.3144/expresspolymlett.2013.17

[71] Gong T., Li W., Chen H., Wang L., Shao S., Zhou S.: Remotely actuated shape memory effect of electrospun composite nanofibers. Acta Biomaterialia, **8**, 1248–1259 (2012).
DOI: 10.1016/j.actbio.2011.12.006

[72] Sun L., Huang W. M., Ding Z., Zhao Y., Wang C. C., Purnawali H., Tang C.: Stimulus-responsive shape memory materials: A review. Materials and Design, **33**, 577–640 (2012).
DOI: 10.1016/j.matdes.2011.04.065

[73] Sownthari K., Suthanthiraray S. A.: Synthesis and characterization of an electrolyte system based on a biodegradable polymer. Express Polymer Letters, **7**, 495–504 (2013).
DOI: 10.3144/expresspolymlett.2013.46

[74] Wang R., Schuman T. P.: Vegetable oil-derived epoxy monomers and polymer blends: A comparative study with review. Express Polymer Letters, **7**, 272–292 (2013).
DOI: 10.3144/expresspolymlett.2013.25

eXPRESS Polymer Letters Vol.8, No.6 (2014) 413–424
Available online at www.expresspolymlett.com
DOI: 10.3144/expresspolymlett.2014.45

Hyperbranched polysiloxane functionalized graphene oxide for dicyclopentadiene bisphenol dicyanate ester nanocomposites with high performance

M. M. Zhang, H. X. Yan, C. Gong, T. T. Li*

Department of Applied Chemistry, School of Science, Northwestern Polytechnical University, Xi'an, 710129 Shaanxi, P.R. China

Received 7 December 2013; accepted in revised form 31 January 2014

Abstract. We report an efficient and novel method to functionalize graphene oxide (GO) with hyperbranched polysiloxane and successfully compound them with dicyclopentadiene bisphenol dicyanate ester (DCPDCE) to prepare nanocomposites. X-ray photoelectron spectroscopy (XPS) and Fourier-transform infrared spectra (FT-IR) were employed to examine the surface functionalization of GO. The effects of functionalized GO on the curing reaction, mechanical, dielectric and thermal properties of DCPDCE resin were investigated systematically. Results of DSC show that the addition of modified GO can facilitate the curing reaction of DCPDCE and decrease the curing temperature of DCPDCE. Compared with pure DCPDCE resin, the impact and flexural strengths of the nanocomposite materials are improved markedly with up to 66 and 50% increasing magnitude, respectively. Meanwhile, the modified GO/DCPDCE systems exhibit lower dielectric constant and loss than pure DCPDCE resin over the testing frequency from 10 to 60 MHz. In addition, the thermal stability and moisture resistance of modified GO/DCPDCE nanocomposties are also superior to that of pure DCPDCE resin.

Keywords: *nanocomposites, graphene oxide, cyanate ester, mechanical properties, dielectric properties*

1. Introduction

Cyanate ester resin has been regarded as the candidate with the great competition to fabricate advanced functional/structural materials for electronic and aerospace industries due to its excellent integral properties, such as outstanding mechanical properties, good molding workability as well as outstanding dielectric properties, etc. [1–3]. Unfortunately, like most thermosetting resins, the biggest shortcoming of cyanate ester resin is its brittleness, which is the major disadvantage to restrict further expansion into the advanced industrial applications. Therefore, the potential applications as cost-effective replacement of engineering polymers by composite materials based on cyanate ester resin have attracted considerable attention and has been widely investigated. To improve the toughness, several methods have been developed to modify cyanate ester resins, such as polymer blending [4, 5], filling with mineral fillers [6, 7] and fiber reinforcement [8]. The advantage of these methods is that the fracture toughness can be improved dramatically. However, it is found to be difficult to obtain a resin system with both good mechanical and dielectric properties; in other words, the improvement of mechanical properties is generally accompanied by a decrease the other properties of the original cyanate ester resin. Therefore, there is a great interest to develop a new method to overcome the key shortcomings of original cyanate ester resin at the same time without deteriorating its original outstanding properties including excellent thermal property, dielectric property and moisture resistance.

*Corresponding author, e-mail: Hongxiayan@nwpu.edu.cn

Graphene, which is recognized as one of the strongest materials in the world, has generated much excitement among materials scientists due to its unique physical, chemical, and mechanical properties [9, 10]. Polymer/graphene nanocomposites have been intensively studied in the recent years with the aim to obtain high-performance materials [11–17]. However, pristine graphene is not quite ready for using as a filler due to the strong tendency of the monolayer graphene sheet to form irreversible agglomerates into monolayer graphite through strong π-π stacking and van der Waals interaction. Poor dispersability in most common organic polymers has been a hurdle in the way of exploitation [18]. Therefore, processing and dispersion of graphene in the polymeric hosts constitute the main challenge to use it in nanocomposites, the control of the interfacial interaction being crucial [19–21].

Hyperbranched polymers are special kinds of polymers with highly branched structure, they have good solubility, low melt viscosity, and extremely high density of functional groups, so they can be utilized advantageously as surface modifiers [22]. Anchoring the hyperbranched polymers on the silica nanoparticles [23] and carbon nanotubes [24] has been studied for improving solubility of the inorganic materials, and the obtained hybrid nanoparticles exhibited some novel properties. Among reported hyperbranched polymers so far, hyperbranched polysiloxanes are beginning to attract interests as new organic inorganic hybrid materials because they combine the unique chemical structure of polysiloxane and hyperbranched topology structure, and thus possess low viscosity, high reactivity, low surface energy and interface tension [25, 26]. Gu's group [27–29] investigated the effects of hyperbranched polysiloxane on the properties of cyanate ester resin, and the results show that hyperbranched polysiloxane has good compatibility with cyanate ester matrix and the incorporation of hyperbranched polysiloxane in cyanate ester leads to an obvious improvement in the mechanical and thermal properties. In order to develop graphene-based cyanate ester nanocomposites with high performance, hyperbranched polysiloxane functionalized graphene oxide (GO) can be a useful method for achieving homogeneous dispersion of GO sheets in polymeric matrix because the hyperbranched polysiloxane can offer stronger interactions between matrix and GO by covalent linkage. In this paper, we propose a facile method to modify dicyclopentadiene bisphenol dicyanate ester by introducing GO functionalized by a hyperbranched polysiloxane which contains active $–C=CH_2$ groups, expecting dispersal of GO in dicyclopentadiene bisphenol dicyanate ester resins. The effects of functionalized GO on the curing reaction, mechanical, dielectric and thermal properties of dicyclopentadiene bisphenol dicyanate ester resins were investigated to develop high performance materials.

2. Experimental

2.1. Reagents and materials

The GO nanosheets were produced from natural graphite flakes by the modified Hummers's method [30]. Dicyclopentadiene bisphenol dicyanate ester (DCPDCE, >99% pure) was purchased from Jiangdu Wuqiao Resin Plant (Jiangsu, China), the structure of DCPDCE was shown in Figure 1. Methylbis (dimethylallylsiloxy)silane was prepared according to the literature [31]. Vinyltriethoxysilane was purchased from Jingzhou Jianghan Fine Chemical Co. Ltd (Hubei, China). Platinum-carbon catalyst (Pt/C) was purchased from Shaanxi Kaida Chemical Engineering Co. Ltd (Shaanxi, China). Ethanol, carbon tetrachloride and hydrochloric acid (HCl) were purchased form Tianjin Fuyu Fine Chemical Co. Ltd (Hebei, China). Acetone was purchased from Tianjin Ruijinte Chemicals Co., Ltd (Tianjin, China). Distilled water was produced by our laboratory. Other reagents were all commercial products with analysis grades.

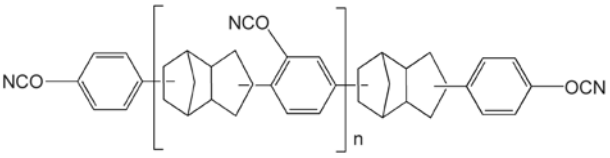

Figure 1. The structure of DCPDCE

2.2. Preparation of vinyltriethoxysilane grafted GO

GO nanosheets (1.0 g), vinyltriethoxysilane (10.0 mL), ethanol (95%, 100 mL) and distilled water (15.0 mL) were combined in a glass beaker. HCl (0.1 mol/L) was slowly dropped into the glass breaker with stirring to adjust the pH value to 3~4. Then the mixture was dispersed through ultrasonication for 2 h. After that, the solution was transferred into a 250 mL three-neck round-bottom flask equipped with a mechanical stirrer, reflux-con-

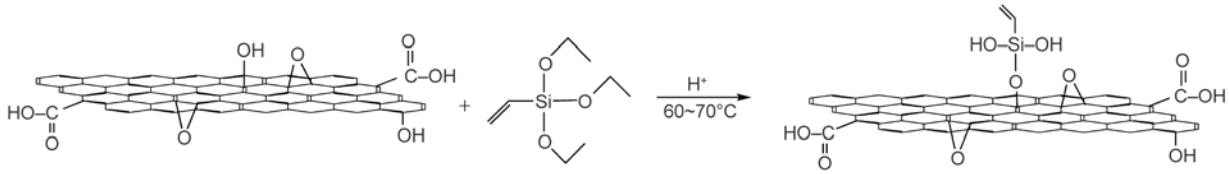

Figure 2. The synthesis route of vinyltriethoxysilane grafted GO

denser and thermometer. Then the mixture was heated to 60~70°C and held for about 5 h. The synthetic route was shown in Figure 2. After the reaction, the mixture was filtrated and washed with acetone to remove the unreacted vinyltriethoxysilane. Finally, the resulting product was collected and dried in a vacuum oven at 50°C for 12 h.

2.3. Preparation of hyperbranched polysiloxane functionalized graphene oxide (HBPGO)

In a four-neck round-bottom flask holding a nitrogen inlet, mechanical stirrer, reflux-condenser, constant-pressure funnel and thermometer, vinyltriethoxysilane grafted GO (0.2 g), Pt/C catalyst (6 mg) and carbon tetrachloride (100 mL) were added. At 25°C, the methylbis(dimethylallylsiloxy) silane (1.0 g) was slowly dropped into the flask through the constant-pressure funnel. The reaction mass was then slowly heated to 50°C at which the reaction continued for 5 h. The synthetic route was shown in Figure 3. After the reaction, the product was filtered and washed with copious amounts of ethanol (95%). Finally, the resulting product was collected and dried in a vacuum oven at 50°C for 24 h before use.

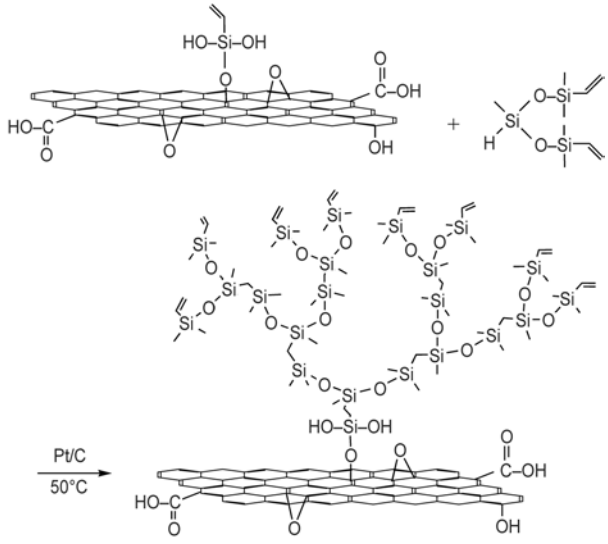

Figure 3. The synthesis route of HBPGO

2.4. Preparation of HBPGO/DCPDCE nanocomposites

The DCPDCE was heated to 100°C in a glass beaker and kept at this constant temperature until melting. The appropriate amount of HBPGO was then carefully mixed with the melted DCPDCE using a mechanical high shear dispersion process. The mixture, consisting of prepolymer and HBPGO, was heated to 140°C in an oil bath and kept at this temperature for 15~20 min with stirring. Then the mixture was put into a preheated mold with release agent followed by degassing at 140°C for 1 h in a vacuum oven. After that, the mixture was cured and post-cured via the procedures of 160°C/1 h + 180°C/1 h + 200°C/2 h + 220°C/2 h and 240°C/2 h, respectively. Finally, the mold was cooled to room temperature and demolded to get the samples of HBPGO/DCPDCE systems.

The samples of pure DCPDCE resin were prepared in the same manner as above. All samples were dried at 120°C under vacuum for 6 h and kept in a dry environment prior to testing.

2.5. Characterization

Fourier Transform Infrared (FTIR) spectrum was recorded between 400 and 4000 cm^{-1} with a resolution of 2 cm^{-1} on a Nicolet FTIR 5700 spectrometer (USA). The samples were mixed with potassium bromide (KBr) powder, to form the homogeneous mixtures using a grinder, and then the mixtures were compression moulded at 10 bar pressure to make a thin disc for the test.

X-ray photo-electron spectroscopy (XPS, Thermal Scientific K-Alpha XPS spectrometer) was used to investigate the surface elemental composition of GO and HBPGO. The analysis was performed under 1027 Torr vacuum with an AlKa X-ray source using a power of 200 W.

Transmission electron microscopic (TEM) images were obtained by a HITACHIS-600 (Japan) transmission electron microscope operating at 200 kV.

For TEM samples preparation, GO and HBPGO were dispersed in ethanol and chloroform, respectively. The dispersions of GO/ethanol and HBPGO/chloroform were dropped on a copper grid for TEM imaging, respectively.

Gel time was measured on a temperature-controlled hot plate by the standard knife method, the time required for the resin to stop legging and becomes elastic is recorded as the gel time.

Differential scanning calorimetry (DSC, MDSC2910, TA Instruments) experiments were performed at a heating rate of 5°C/min in a nitrogen atmosphere, heating from 25–350°C.

Impact strength was determined according to GB/T 2571-1995. Samples were cut into strips of (50±0.02)×(7±0.02)×(4±0.02) mm^3 by a cutting machine. The impact strength tests were performed using a Charpy impact machine tester (XCJ-L, China). Five samples were tested for each composition, and the results are presented as an average for tested samples.

Flexural strength was measured according to GB/T 2570-1995. Samples were cut into strips of (80±0.02)×(10±0.02)×(4±0.02) mm^3. The flexural tests were performed using an electronic universal testing machine (RIGER-20, China) at a crosshead speed of 2 mm·min^{-1}. Five samples were tested for each composition, and the results are presented as an average for tested samples.

Scanning electron micrographs (SEM) were performed on a HITACHIS-570 instrument. For SEM samples preparation, the fracture surface of the specimens was sputtered with a thin layer (about 10 nm) of gold by vapor deposition on a stainless steel stub using a vacuum sputter coater.

Thermogravimetrical analysis (TGA) tests were performed by using Perkin Elmer TGA-7 (USA) at a heating rate of 10°C/min in a nitrogen atmosphere from 25 to 800°C.

The dielectric constant and loss factor were measured by a high frequency QBG-3 Gauger and a S914 dielectric loss test set (China) at the frequency range from 10 to 60 MHz. The sample dimension was (25±0.02)×(25±0.02)×(3±0.02) mm^3. For each condition, five samples were tested the data was averaged.

The water absorption of a sample was determined by swelling the sample in distilled water for 48 h at 100°C. The sample dimension was (10±0.02)×(10±0.02)×(3±0.02) mm^3. The percentage of water absorbed by the specimen is calculated using equation. Percentage of water absorption = $(w_2 - w_1)/w_1$. Where w_1 is the initial weight of the sample and w_2 is the weight of the sample after immersion in water for 48 h at 100°C.

3. Results and discussions

3.1. Characteristics of HBPGO

X-ray photoelectron spectroscopy (XPS) is used for the investigation of elementary composition on the surface of the GO and HBPGO. Figures 4a and 4b show the board scan XPS spectra of the GO and HBPGO, respectively. Table 1 lists the elementary composition of HBPGO. Compared the board scan XPS spectrum of the GO (Figure 4a) with that of HBPGO (Figure 4b), successful grafting of the hyperbranched polysiloxane onto the GO can be confirmed due to the detection of silicon (Si) element. The Si element only derives from the hyperbranched polysiloxane, the C element and the O element derive from both the HBPGO and the GO.

Further evidence on the successful grafting of the hyperbranched polysiloxane onto the GO and the covalent bonding between the GO and the hyper-

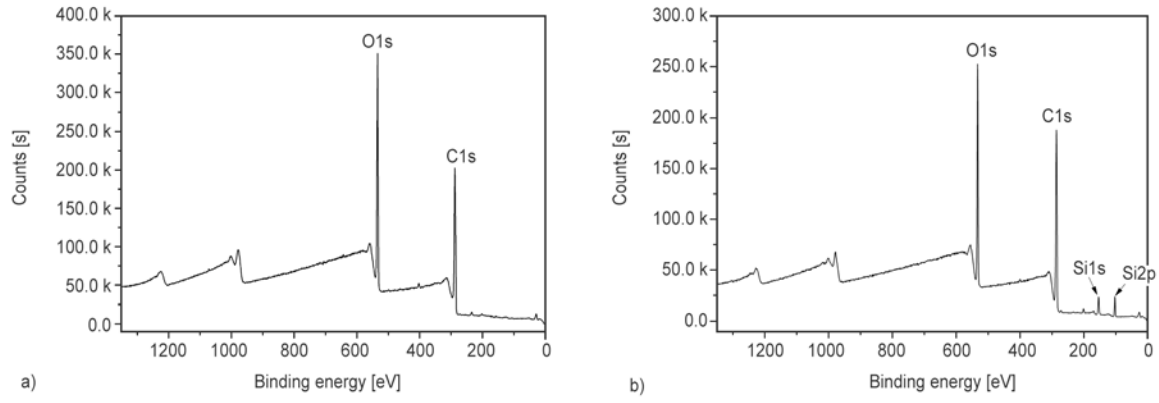

Figure 4. Board scan XPS spectra of GO (a) and HBPGO (b)

branched polysiloxane chains can be demonstrated by FTIR spectra, as shown in Figure 5. Compared the FTIR spectrum of the GO with that of HBPGO, significant changes in the range of 3500 to 500 cm^{-1} can be observed, which indicates the occurrence of chemical reaction. The details are discussed as follows.

Table 1. Elementary composition of HBPGO

Element	Bonding energy [eV]	Peak	Atom composition [%]
C	285.15	1s	40.78
O	532.85	1s	40.97
Si	154.11	1s	9.15
	103.10	2p	9.11

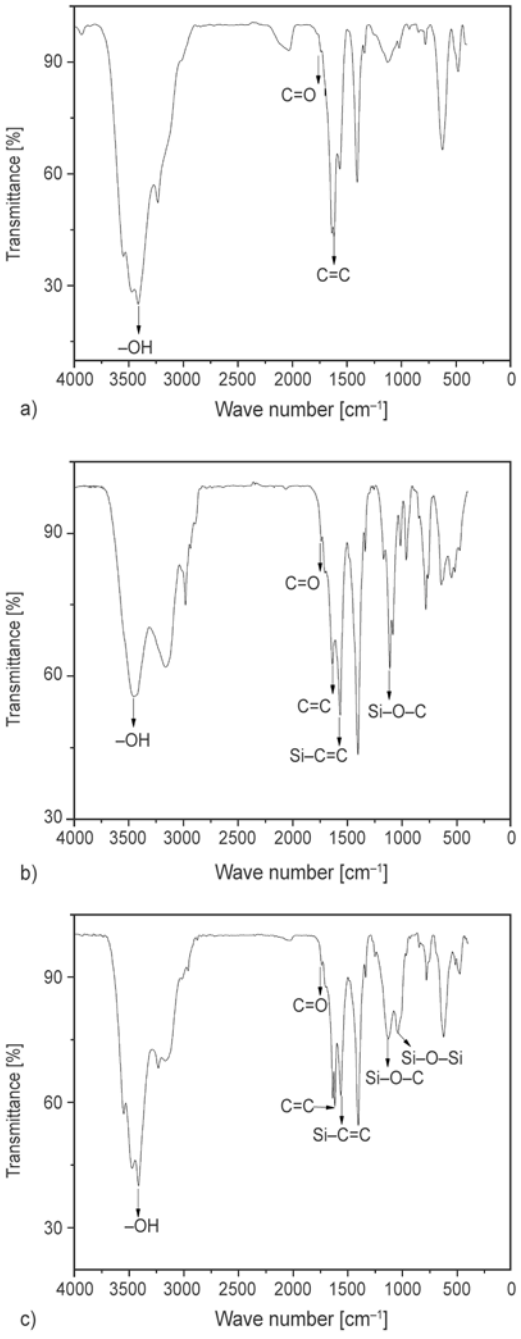

Figure 5. FTIR spectra of GO (a), vinyltriethoxysilane grafted GO (b) and HBPGO (c)

Figure 5a shows the FTIR spectrum of the GO. Intense absorption peak at 3421 cm^{-1} represents hydroxyl (–OH) groups, and the strong intensity may be affected by the absorbed water molecules. Peaks at 1626, 1055 and 1737.79 cm^{-1} are generated by C=C, C–O and C=O vibrations, respectively. Peaks at 864 and 1250 cm^{-1} are generated by bending and stretching vibrations of epoxy groups. Therefore, it can be concluded that the oxygen-containing functional groups of GO mainly are hydroxyl, epoxy and carboxyl groups. In the case of vinyltriethoxysilane grafted GO, as seen in Figure 5b, the peaks at around 3424, 1737 and 1622 cm^{-1}, which are assigned to –OH, C=O and C=C, respectively, continue to be observed, and peaks at 1254 and 909 cm^{-1} are generated by bending and stretching vibrations of epoxy groups. New peaks at 1130 and 1564 cm^{-1}, are assigned to Si–O–C and Si–C=C vibrations, respectively and are clearly visible. After the grafting of the hyperbranched monomers on the surface of vinyltriethoxysilane grafted GO, an obvious change can be observed in the FTIR spectrum as shown in Figure 5c, a new peak is found at 1041 cm^{-1}, which is ascribed to Si–O–Si vibration. These results provide an evidence of the successful covalent grafting of the hyperbranched polysiloxane onto the GO through the chemical reaction.

The nanosheets morphology of GO and HBPGO were investigated by TEM imaging as displayed in Figure 6. TEM analysis (Figure 6a) shows that the GO nanosheets are very thin and have some wrinkles and folded regions, and the surface of the GO nanosheets is fairly smooth, which is consistent with the morphology typically reported in the literature [32, 33, 17, 37]. In contrast, HBPGO (Figure 6b) exhibits a different morphology. Compared with GO, the nanosheets of HBPGO become less transparent, and some black regions on the surface of HBPGO can be observed. The black regions of HBPGO can be attributed to the hyperbranched polysiloxane layer attached onto the GO surface from both sides.

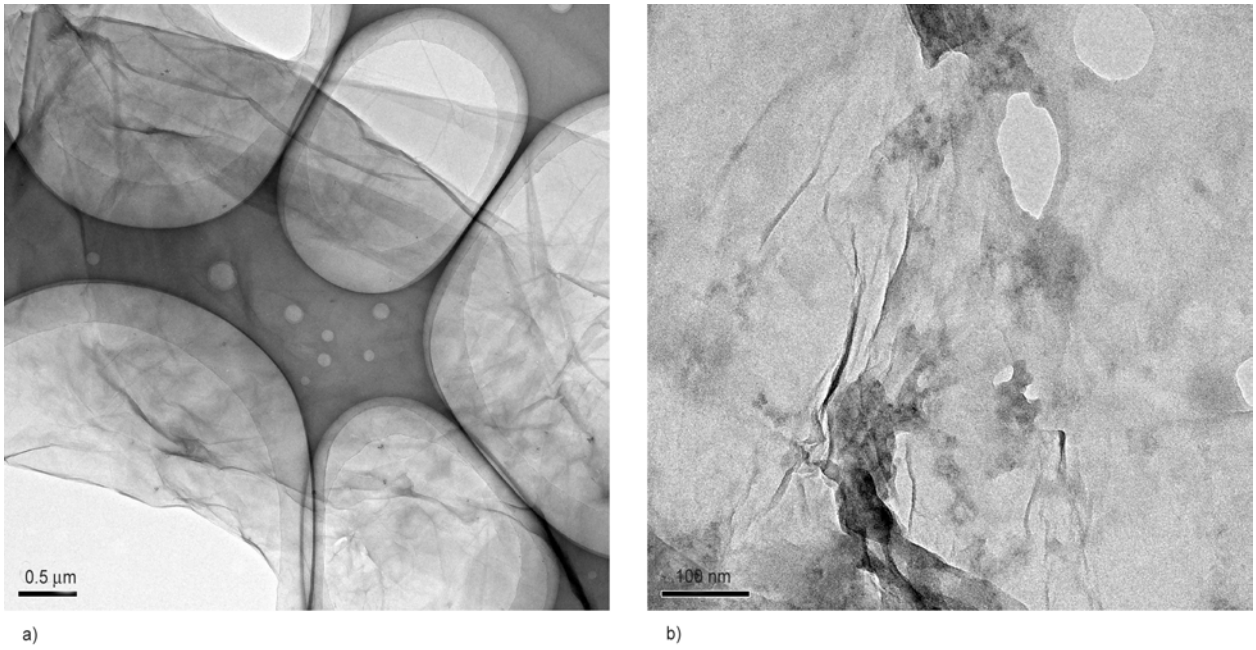

Figure 6. TEM images of GO (a) and HBPGO (b)

3.2. Curing behavior of HBPGO/DCPDCE system

Gel time is generally used to evaluate the curing behavior of a resin, a shorter gel time indicates a bigger curing activity. Figure 7 depicts the gel time of DCPDCE resin and HBPGO/DCPDCE systems at different temperatures, it can be observed that the addition of HBPGO can effectively decrease the gel time of DCPDCE, indicating that the addition of HBPGO can catalyze the gelation of DCPDCE. This phenomenon is mainly attributed to the intensive promotion of the curing reaction of DCPDCE by –OH groups in the molecule of HBPGO [34], and the copolymerization between active –C=CH_2 at the end of molecular chains of HBPGO with –OCN in DCPDCE [27].

In order to further confirm the role of HBPGO on the curing reaction of DCPDCE prepolymer, comparative DSC analyses of DCPDCE resin and 0.6 wt% HBPGO/DCPDCE composites at the heating rate of 5°C/min were carried out, and the corresponding curves are depicted in Figure 8. The whole peak of DCPDCE appears at the temperature from about 180 to 221°C, while that of HBPGO/DCPDCE system is between 160 and 196°C. Comparing with DCPDCE, the maximum curing temperature of HBPGO/DCPDCE shifts to lower temperature by about 15°C, demonstrating that the whole curing process of DCPDCE can be accelerated by a small amount of HBPGO loading. The decreased curing and post-curing temperature is beneficial to manufacture cyanate ester-based composites for industrial application.

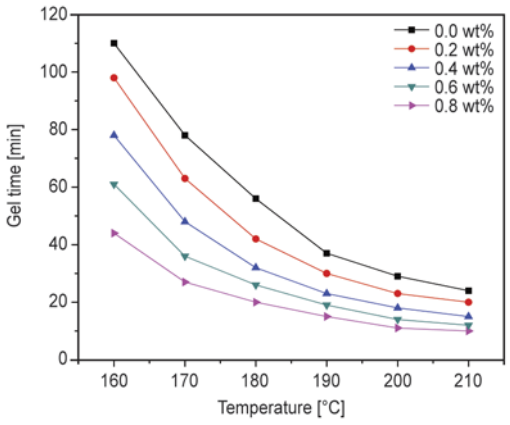

Figure 7. Dependence of gel time on temperature for DCPDCE and HBPGO/DCPDCE systems

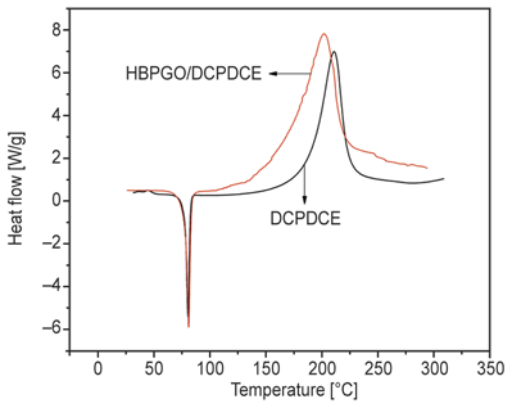

Figure 8. DSC curves of DCPDCE and 0.6 wt% HBPGO/DCPDCE system

3.3. Mechanical properties of HBPGO/DCPDCE system

Figure 9 shows the impact strengths of DCPDCE and HBPGO/DCPDCE systems. It is observed that all the HBPGO/DCPDCE composites exhibit higher impact strengths than pure DCPDCE resin, and the 0.6 wt% HBPGO/DCPDCE system has the maximum impact strength (16 kJ/m^2), which is increased by 66% compared with that of pure DCPDCE, indicating that the addition of HBPGO can significantly improve the toughness of DCPDCE resin. Figure 10 shows the flexural strengths of DCPDCE and HBPGO/DCPDCE systems, and a similar trend can be observed. The 0.6 wt% HBPGO/DCPDCE system has the maximum flexural strength (142 MPa), which is increased by about 50% compared with that of pure DCPDCE resin. Therefore, it can be concluded that the addition of HBPGO can efficiently improve the mechanical properties of DCPDCE resin. The enhancement of impact and flexural strength may be attributed to the outstanding mechanical properties of GO and the increased interface bonding strength between GO and matrix. On one hand, the chain of hyperbranched polysiloxane grafted on the surface of GO nanosheets can bring stronger mutual exclusion and steric hindrance effect, thus the restacking of GO nanosheets is restrained and the agglomeration tendency of GO in matrix can be controlled effectively. On the other hand, the –C=CH$_2$ groups in the molecule of HBPGO can react with –NCO in DCPDCE, leading to improved interfacial bonding strength between GO and matrix. For the HBPGO/DCPDCE system, the probability of forming a strong organic-inorganic combination will be enhanced. Therefore, the mechanical properties of HBPGO/DCPDCE system are increased as the contents of HBPGO from 0.0 to 0.6 wt%. However, when the fillers content is high enough (>0.6 wt%), the mechanical properties of the composites decrease with the increasing concentration of fillers. When the content of nanosheets is too large, the concentration of GO nanosheets is big enough to form aggregates, and thus reducing the mechanical properties. But the 0.8 wt% HBPGO/DCPDCE system still possesses much better mechanical properties than neat resin.

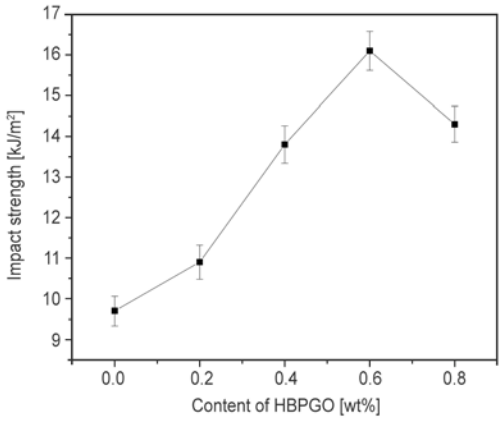

Figure 9. Relationship of impact strength on HBPGO content for HBPGO/DCPDCE systems

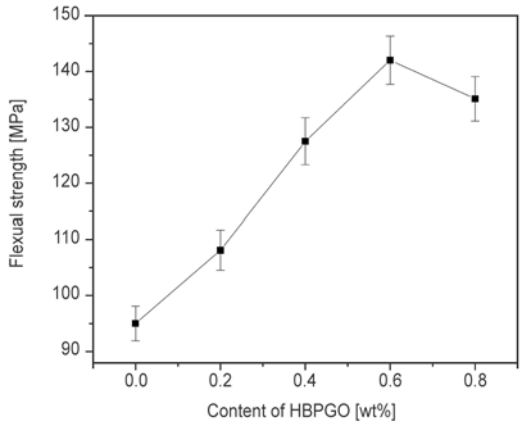

Figure 10. Relationship of flexural strength on HBPGO content for HBPGO/DCPDCE systems

In order to further confirm the effect of HBPGO on the toughness of DCPDCE resin, SEM images of the fracture surfaces of samples after impact tests are taken and shown in Figure 11, it can be observed that pure DCPDCE resin has a smooth and river-like fracture surface (Figure 11a), exhibiting a typical brittle feature. While with the addition of HBPGO into DCPDCE resin, the fracture surfaces become rougher and are accompanied with more ductile sunken areas, which is consistent with the improved impact strength of the nanocomposites. In the case of 0.2 wt% HBPGO/DCPDCE system, as shown in Figure 11b, the surface becomes coarse and some ductile sunken regions can be observed, which can absorb the energy of fracture and hinder the crack propagation. For the 0.6 wt% HBPGO/DCPDCE system, as shown in Figure 11c, the fracture surface of the composite is much rougher than those of pure DCPDCE and 0.2 wt% HBPGO/DCPDCE system, and there exist large amount of ductile sunken areas, exhibiting a typical rough feature. However, when the concentration of HBPGO is 0.8 wt%, as shown in Figure 11d, large clusters in the matrix appear due to the aggregation of HBPGO at high concentration, which will lead to more rapid crack initiation and impact failure. Therefore, the impact

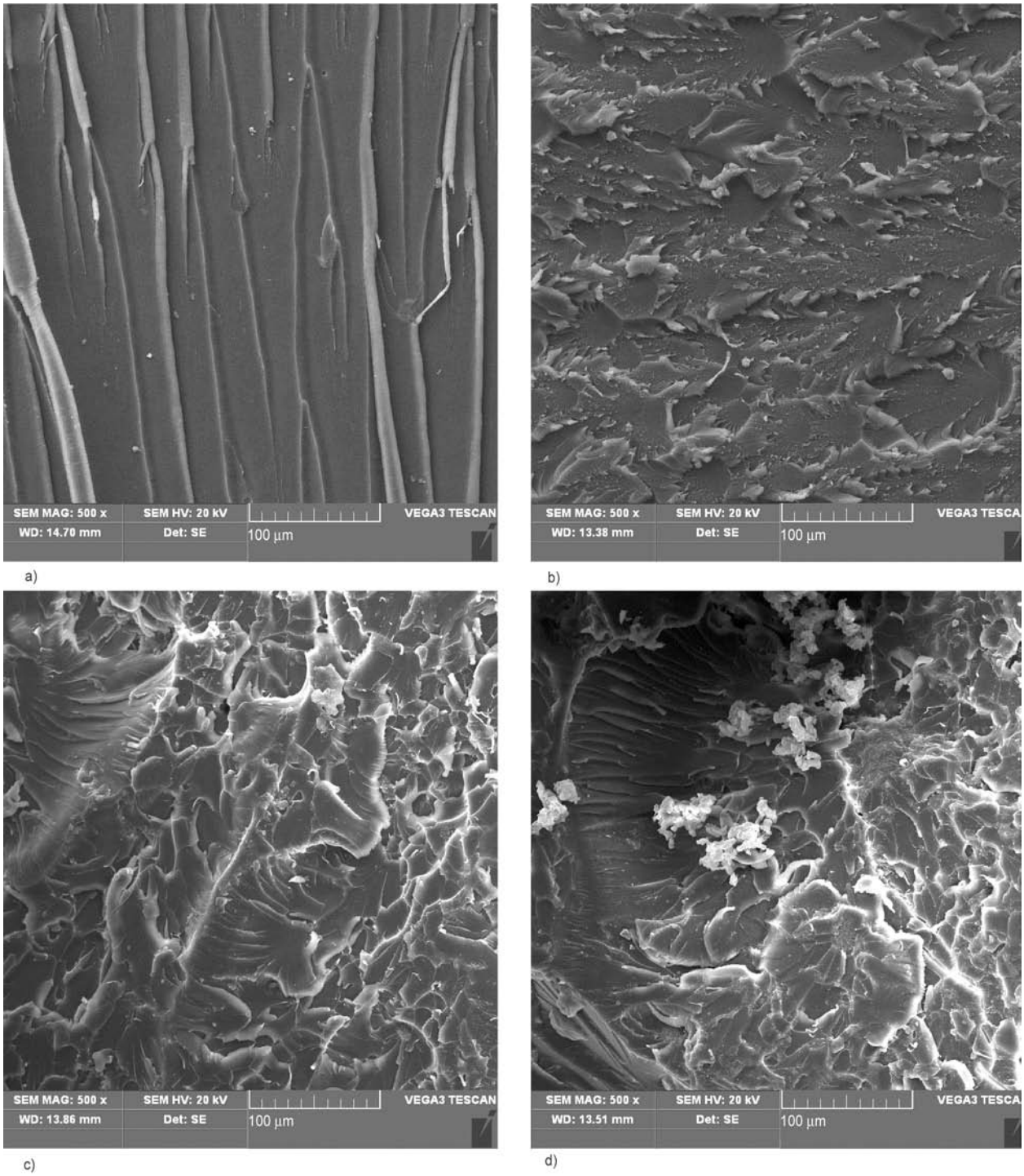

Figure 11. SEM images of the fracture surfaces of the HBPGO/DCPDCE systems with various contents of HBPGO (a: 0.0 wt%, b: 0.2 wt%, c: 0.6 wt%, d: 0.8 wt%)

strength of the nanocomposite with high HBPGO content is decreased. The features of the fracture surfaces of HBPGO/DCPDCE systems accord well with the mechanical properties.

3.4. Dielectric properties of HBPGO/DCPDCE system

One of the most attractive features of DCPDCE resin is its excellent dielectric properties including low and stable dielectric constant (2.8–3.2) and loss (0.002–0.008) over a wide range of frequency, which enables DCPDCE resin to be used in many advanced industries. Therefore, it is necessary to retain the outstanding dielectric properties of the original DCPDCE resin to develop a new modified DCPDCE system. Figures 12 and 13 show dependence of dielectric constant and loss factor on frequency for pure DCPDCE resin and other modified systems,

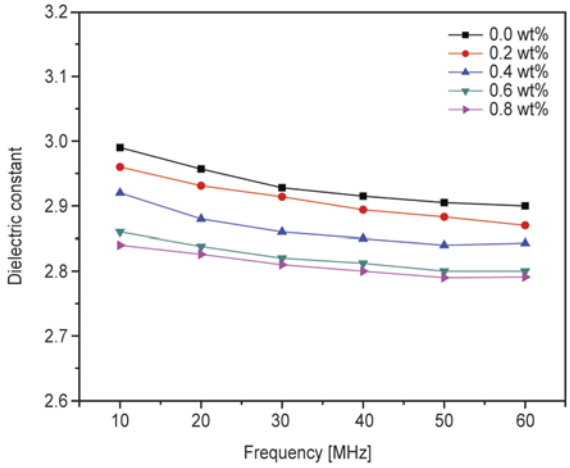

Figure 12. Dielectric constants of DCPDCE resin and HBPGO/DCPDCE systems versus frequency

respectively. It can be seen that the dielectric constant and loss values of HBPGO/DCPDCE system are lower than that of pure DCPDCE resin, and the higher the HBPGO concentration is, the lower the dielectric constant and loss. Meanwhile, the dielectric constant and loss of HBPGO/DCPDCE system remain stable over the testing frequency band from 10 to 60 MHz. With regard to a composite, its dielectric properties are determined by those of both matrix and fillers as well as interfaces [35]. Firstly, GO is an insulator, with oxygen atoms randomly attached at graphene sites, which undergo conversion from sp^2-hybridized carbon atoms in graphene, to sp^3-hybridized carbon in GO. This process reduces conjugation and confines π-electrons [36]. So GO exhibits very low dielectric constant values. When GO sheets are used as interlayers in the polymer matrix, there is much less electron mobility. Wang

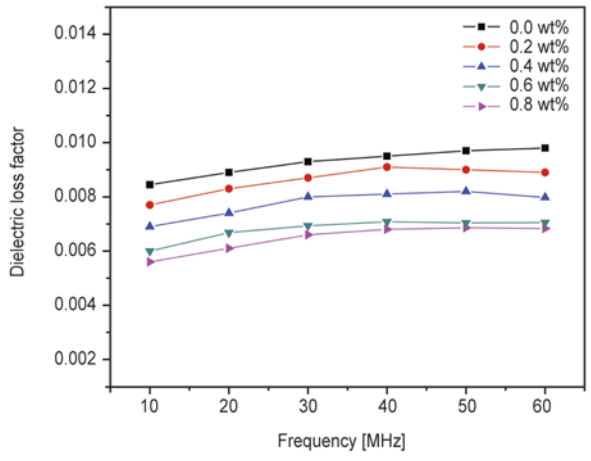

Figure 13. Dielectric loss factors of DCPDCE resin and HBPGO/DCPDCE systems versus frequency

et al. [37] investigated the effect of NH_2-functionalized GO on the dielectric constant of polyimide, and the results showed that the addition of GO/modified GO can efficiently decrease the dielectric constant of polyimide matrix. HBPGO has excellent dielectric properties due to the chemical structure of polysiloxane and special unoccupied spaces of hyperbranched polymers as well as the outstanding dielectric properties of GO, so modified DCPDCE systems with higher HBPGO concentration have smaller dielectric constant values. Secondly, the addition of HBPGO into CE resin promotes the self-polymerization of –NCO groups, thus increases the productivity of symmetrical triazine rings [38]. As a result, the modified DCPDCE system tends to form networks with greater symmetry and larger space hinder, which is beneficial for reducing the dielectric constant and loss. Thirdly, the incorporation of nanofillers can fill the space between polymeric chains of DCPDCE, so the number of movable molecular chains and polarized groups in the network is decreased [39], which also provides contribution to the decrease in dielectric constant and loss. In addition, a good adhesion between HBPGO and DCPDCE matrix will reduce the interfacial polarization and restrict the mobility of chain segments, leading to reduced dielectric constant and loss factor. Therefore, both the dielectric constant and loss factor of HBPGO/DCPDCE system decrease compared with those of pure DCPDCE resin.

3.5. Thermal properties of HBPGO/DCPDCE system

Overlay TGA and DTG curves of DCPDCE resin and 0.6 wt% HBPGO/DCPDCE system are shown in Figure 14. It can be seen that the modified DCPDCE system has higher decomposition temperatures than pure DCPDCE resin. The decomposition temperature at 5% weight loss of pure DCPDCE resin is 390°C, while that of HBPGO/DCPDCE system is 405°C. The char yield at 800°C of pure DCPDCE is 38%, while that of HBPGO/DCPDCE system is 46%. The higher decomposition temperatures and char yields of the composite materials suggest that the HBPGO/DCPDCE system possesses better thermal stability than pure DCPDCE. The enhanced thermal stability of the HBPGO/DCPDCE nanocomposite may be mainly attributed to the excellent thermal stability of HBPGO, and the increased

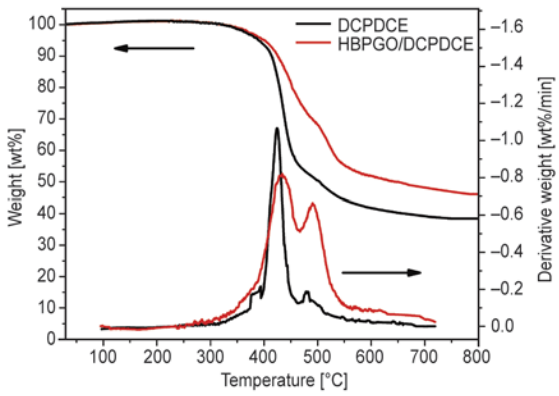

Figure 14. Overlay TGA and DTG curves of DCPDCE and 0.6 wt% HBPGO/DCPDCE system

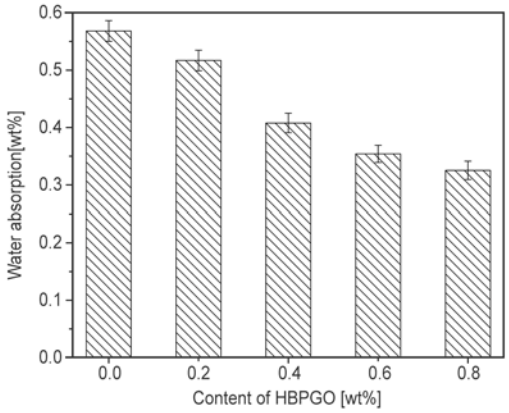

Figure 15. Water absorption of DCPDCE resin and HBPGO/DCPDCE systems

cross-linking degree of HBPGO/DCPDCE system which results from the catalytic effect of HBPGO in DCPDCE [27], as well as the fact that the mobility of polymer segments at the interfaces between the HBPGO and the DCPDCE matrix is suppressed by strong interactions [40]. In addition, compared with pure DCPDCE, the HBPGO/DCPDCE system is subject to a mass loss proceeding in two major steps. The former mass loss is attributed to the degradation of triazine rings, while the latter mass loss may mainly be caused by the pyrolysis of HBPGO because the thermal stability of the hyperbranched polysiloxane grafted on the surface of GO is better than that of triazine rings.

3.6. Water absorption of HBPGO/DCPDCE system

Outstanding moisture resistance is a very important property of a material, especially those requiring stably high performance, because in general absorbed water will decline almost all properties of the original material including thermal, mechanical and dielectric properties, etc., so very low water absorption is one important target for developing new resin systems with high performance [41]. One of the advantages of the DCPDCE resin is its low water absorption. Figure 15 gives the water absorption values of HBPGO/DCPDCE systems and that of pure DCPDCE resin for comparison. It can be seen that the water absorption decreases from 0.57 to 0.51 wt% with the small addition (0.2 wt%) of HBPGO into DCPDCE resin, and which continually decreases with the continuous increase of HBPGO content in HBPGO/DCPDCE systems. In case of 0.6 wt% HBPGO/DCPDCE system, its water absorption is 0.35 wt%, which is much lower than that of pure DCPDCE resin. The improvement of water-resistant property of HBPGO/DCPDCE systems may be ascribed to the following reasons. Firstly, as discussed earlier, the addition of HBPGO can effectively promote the curing reaction of DCPDCE, and thus leads to increasing conversion of the -OCN groups, which is a positive role on reducing the water absorption of DCPDCE resin. Secondly, Si-O–Si chains in HBPGO have excellent hydrophobic properties, which is beneficial to improve the water-resistant property of HBPGO/DCPDCE systems. Thirdly, a large number of functional groups on the HBPGO surface can enhance inorganic/organic phase compatibilization at the interface, which can effectively prevent water from entering the network of nanocomposties.

4. Conclusions

A kind of high-performance polymer composite has been fabricated using DCPDCE resin as matrix and GO as filler employing the method of melting mixing, in which the GO was modified with a hyperbranched polysiloxane before use in order to improve its dispersability and compatibility with the DCPDCE matrix. The incorporation of HBPGO into DCPDCE resin can not only effectively promote the curing reaction of DCPDCE, but also brings a lot of changes in the properties of HBPGO/DCPDCE nanocomposite materials. The impact and flexural strengths are increased obviously with suitable content of HBPGO within the matrix. In addition, the HBPGO/DCPDCE systems also exhibit better dielectric property, thermal stability and moisture resistance than pure DCPDCE resin. Especially, when

the concentration of HBPGO is 0.6 wt%, the best overall performance of HBPGO/DCPDCE nanocomposites can be achieved.

Acknowledgements

This work was financially supported by the Aerospace Science Foundation of China (2011ZF53064), Research Fund for the Doctoral Program of Higher Education (20136102110049) and graduate starting seed fund of Northwestern Polytechnical University (Z2014025).

References

[1] Mondragón I., Solar L., Nohales A., Vallo C. I., Gómez C. M.: Properties and structure of cyanate ester/polysulfone/organoclay nanocomposites. Polymer, **47**, 3401–3409 (2006).
DOI: 10.1016/j.polymer.2006.03.047

[2] Kimura H., Ohtsuka K., Matsumoto A.: Curing reaction of bisphenol-A based benzoxazine with cyanate ester resin and the properties of the cured thermosetting resin. Express Polymer Letters, **5**, 1113–1122 (2011).
DOI: 10.3144/expresspolymlett.2011.108

[3] Zhang J., Hu S., Zhan G., Tang X., Yu Y.: Biobased nanocomposites from clay modified blend of epoxidized soybean oil and cyanate ester resin. Progress in Organic Coatings, **76**, 1683–1690 (2013).
DOI: 10.1016/j.porgcoat.2013.07.017

[4] Santhosh Kumar K. S., Reghunadhan Nair C. P., Ninan K. N.: Investigations on the cure chemistry and polymer properties of benzoxazine–cyanate ester blends. European Polymer Journal, **45**, 494–502 (2009).
DOI: 10.1016/j.eurpolymj.2008.11.001

[5] Tao Q., Gan W., Yu Y., Wang M., Tang X., Li S.: Viscoelastic effects on the phase separation in thermoplastics modified cyanate ester resin. Polymer, **45**, 3505–3510 (2004).
DOI: 10.1016/j.polymer.2004.03.043

[6] Wooster T. J., Abrol S., MacFarlane D. R.: Polymeric toughening of particle filled cyanate ester composites. Macromolecular Materials and Engineering, **290**, 961–969 (2005).
DOI: 10.1002/mame.200500178

[7] Liang K., Toghiani H., Pittman Jr C. U.: Synthesis, morphology and viscoelastic properties of epoxy/polyhedral oligomeric silsesquioxane (POSS) and epoxy/cyanate ester/POSS nanocomposites. Journal of Inorganic and Organometallic Polymers and Materials, **21**, 128–142 (2011).
DOI: 10.1007/s10904-010-9436-8

[8] Badrinarayanan P., Rogalski M. K., Kessler M. R.: Carbon fiber-reinforced cyanate ester/nano-ZrW_2O_8 composites with tailored thermal expansion. ACS Applied Materials and Interfaces, **4**, 510–517 (2011).
DOI: 10.1021/am201165q

[9] Geim A. K.: Graphene: Status and prospects. Science, **324**, 1530–1534 (2009).
DOI: 10.1126/science.1158877

[10] Dreyer D. R., Park S., Bielawski C. W., Ruoff R. S.: The chemistry of graphene oxide. Chemical Society Reviews, **39**, 228–240 (2010).
DOI: 10.1039/B917103G

[11] Yuan X. Y., Zou L. L., Liao C. C., Dai J. W.: Improved properties of chemically modified graphene/poly(methyl methacrylate) nanocomposites via a facile in-situ bulk polymerization. Express Polymer Letters, **6**, 847–858 (2012).
DOI: 10.3144/expresspolymlett.2012.90

[12] Liang J., Huang L., Li N., Huang Y., Wu Y., Fang S., Oh J., Kozlov M., Ma Y., Li F., Baughman R., Chen Y.: Electromechanical actuator with controllable motion, fast response rate, and high-frequency resonance based on graphene and polydiacetylene. ACS Nano, **6**, 4508–4519 (2012).
DOI: 10.1021/nn3006812

[13] Huang L., Yi N., Wu Y., Zhang Y., Zhang Q., Huang Y., Ma Y., Chen Y.: Multichannel and repeatable self-healing of mechanical enhanced graphene-thermoplastic polyurethane composites. Advanced Materials, **25**, 2224–2228 (2013).
DOI: 10.1002/adma.201204768

[14] Liang J., Xu Y., Sui D., Zhang L., Huang Y., Ma Y., Li F., Chen Y.: Flexible, magnetic, and electrically conductive graphene/Fe_3O_4 paper and its application for magnetic-controlled switches. The Journal of Physical Chemistry C, **114**, 17465–17471 (2010).
DOI: 10.1021/jp105629r

[15] Wan C., Chen B.: Reinforcement and interphase of polymer/graphene oxide nanocomposites. Journal of Materials Chemistry, **22**, 3637–3646 (2012).
DOI: 10.1039/c2jm15062j

[16] Liu L., Gao Y., Liu Q., Kuang J., Zhou D., Ju S., Han B., Zhang Z.: High mechanical performance of layered graphene oxide/poly(vinyl alcohol) nanocomposite films. Small, **9**, 2466–2472 (2013).
DOI: 10.1002/smll.201300819

[17] Rafiee M. A., Rafiee J., Wang Z., Song H., Yu Z-Z., Koratkar N.: Enhanced mechanical properties of nanocomposites at low graphene content. ACS Nano, **3**, 3884–3890 (2009).
DOI: 10.1021/nn9010472

[18] He H., Gao C.: General approach to individually dispersed, highly soluble, and conductive graphene nanosheets functionalized by nitrene chemistry. Chemistry of Materials, **22**, 5054–5064 (2010).
DOI: 10.1021/cm101634k

[19] Gudarzi M. M., Sharif F.: Enhancement of dispersion and bonding of graphene-polymer through wet transfer of functionalized graphene oxide. Express Polymer Letters, **6**, 1017–1031 (2012).
DOI: 10.3144/expresspolymlett.2012.107

[20] Zhan Y., Yang J., Zhou Y., Yang X., Meng F., Liu X.: Nitrile functionalized graphene for poly(arylene ether nitrile) nanocomposite films with enhanced dielectric permittivity. Materials Letters, **78**, 88–91 (2012). DOI: 10.1016/j.matlet.2012.03.029

[21] Lin Y., Jin J., Song M.: Preparation and characterisation of covalent polymer functionalized graphene oxide. Journal of Materials Chemistry, **21**, 3455–3461 (2011). DOI: 10.1039/c0jm01859g

[22] Gao C., Yan D.: Hyperbranched polymers: From synthesis to applications. Progress in Polymer Science, **29**, 183–275 (2004). DOI: 10.1016/j.progpolymsci.2003.12.002

[23] Yu Y., Rong M. Z., Zhang M. Q.: Grafting of hyperbranched aromatic polyamide onto silica nanoparticles. Polymer, **51**, 492–499 (2010). DOI: 10.1016/j.polymer.2009.12.013

[24] Gao C., Muthukrishnan S., Li W., Yuan J., Xu J., Müller A. H. E.: Linear and hyperbranched glycopolymer-functionalized carbon nanotubes: Synthesis, kinetics, and characterization. Macromolecules, **40**, 1803–1815 (2007). DOI: 10.1021/ma062238z

[25] Ganicz T., Pakula T., Fortuniak W., Białecka-Florjańczyk E.: Linear and hyperbranched liquid crystalline polysiloxanes. Polymer, **46**, 11380–11388 (2005). DOI: 10.1016/j.polymer.2005.10.052

[26] Zheng Y., Thurecht K. J., Wang W.: Polysiloxanes polymers with hyperbranched structure and multivinyl functionality. Journal of Polymer Science Part A: Polymer Chemistry, **50**, 629–637 (2012). DOI: 10.1002/pola.25072

[27] Zhou C., Gu A., Liang G., Ji L., Yuan L.: Preparation and properties of novel resins based on cyanate ester and hyperbranched polysiloxane. Journal of Polymer Research, **18**, 139–149 (2011). DOI: 10.1007/s10965-010-9400-x

[28] Zhuo D., Gu A., Liang G., Hu J-T., Yuan L., Chen X.: Flame retardancy materials based on a novel fully end-capped hyperbranched polysiloxane and bismaleimide/diallylbisphenol A resin with simultaneously improved integrated performance. Journal of Materials Chemistry, **21**, 6584–6594 (2011). DOI: 10.1039/c1jm10233h

[29] Zhou C., Gu A., Liang G., Yuan L.: Novel toughened cyanate ester resin with good dielectric properties and thermal stability by copolymerizing with hyperbranched polysiloxane and epoxy resin. Polymers for Advanced Technologies, **22**, 710–717 (2011). DOI: 10.1002/pat.1570

[30] Hummers Jr W. S., Offeman R. E.: Preparation of graphitic oxide. Journal of the American Chemical Society, **80**, 1339 (1958). DOI: 10.1021/ja01539a017

[31] Si Q-F., Wang X., Fan X-D., Wang S-J.: Synthesis and characterization of ultraviolet-curable hyperbranched poly(siloxysilane)s. Journal of Polymer Science Part A: Polymer Chemistry, **43**, 1883–1894 (2005). DOI: 10.1002/pola.20675

[32] Bao C., Song L., Xing W., Yuan B., Wilkie C. A., Huang J., Guo Y., Hu Y.: Preparation of graphene by pressurized oxidation and multiplex reduction and its polymer nanocomposites by masterbatch-based melt blending. Journal of Materials Chemistry, **22**, 6088–6096 (2012). DOI: 10.1039/C2JM16203B

[33] Liu J., Chen G., Jiang M.: Supramolecular hybrid hydrogels from noncovalently functionalized graphene with block copolymers. Macromolecules, **44**, 7682–7691 (2011). DOI: 10.1021/ma201620w

[34] Lin C. H.: Synthesis of novel phosphorus-containing cyanate esters and their curing reaction with epoxy resin. Polymer, **45**, 7911–7926 (2004). DOI: 10.1016/j.polymer.2004.09.023

[35] Yu S., Hing P., Hu X.: Dielectric properties of polystyrene–aluminum-nitride composites. Journal of Applied Physics, **88**, 398–404 (2000). DOI: 10.1063/1.373672

[36] Mkhoyan K. A., Contryman A. W., Silcox J., Stewart D. A., Eda G., Mattevi C., Miller S., Chhowalla M.: Atomic and electronic structure of graphene-oxide. Nano Letters, **9**, 1058–1063 (2009). DOI: 10.1021/nl8034256

[37] Wang J-Y., Yang S-Y., Huang Y-L., Tien H-W., Chin W-K., Ma C-C. M.: Preparation and properties of graphene oxide/polyimide composite films with low dielectric constant and ultrahigh strength via in situ polymerization. Journal of Materials Chemistry, **21**, 13569–13575 (2011). DOI: 10.1039/c1jm11766a

[38] Zhang X., Gu A., Liang G., Zhuo D., Yuan L.: Liquid crystalline epoxy resin modified cyanate ester for high performance electronic packaging. Journal of Polymer Research, **18**, 1441–1450 (2011). DOI: 10.1007/s10965-010-9549-3

[39] Zhang Z., Liang G., Wang X., Adhikari S., Pei J.: Curing behavior and dielectric properties of amino-functionalized polyhedral oligomeric silsesquioxane/cyanate ester resin hybrids. High Performance Polymers, **25**, 427–435 (2013). DOI: 10.1177/0954008312469234

[40] Lin Q., Qu L., Lü Q., Fang C.: Preparation and properties of graphene oxide nanosheets/cyanate ester resin composites. Polymer Testing, **32**, 330–337 (2013). DOI: 10.1016/j.polymertesting.2012.11.014

[41] Ho T-H., Hwang H-J., Shieh J-Y., Chung M-C.: Thermal, physical and flame-retardant properties of phosphorus-containing epoxy cured with cyanate ester. Reactive and Functional Polymers, **69**, 176–182 (2009). DOI: 10.1016/j.reactfunctpolym.2008.12.019

eXPRESS Polymer Letters Vol.8, No.6 (2014) 425–435
Available online at www.expresspolymlett.com
DOI: 10.3144/expresspolymlett.2014.46

Study on the structure-properties relationship of natural rubber/SiO_2 composites modified by a novel multi-functional rubber agent

S. Y. Yang[1], L. Liu[2], Z. X. Jia[2], W. W. Fu[2], D. M. Jia[2], Y. F. Luo[2]*

[1]Chemical Industrial Cleaner Production and Green Chemical R&D Center of Guang Dong Universities, Dongguan University of Technology, Dongguan, China
[2]College of materials science and engineering, South China University of Technology, Guangzhou, China

Received 13 December 2014; accepted in revised form 9 February 2014

Abstract. Vulcanization property and structure-properties relationship of natural rubber (NR)/silica (SiO_2) composites modified by a novel multi-functional rubber agent, N-phenyl- N′-(γ-triethoxysilane)-propyl thiourea (STU), are investigated in detail. Results from the infrared spectroscopy (IR) and X-ray photoelectron spectroscopy (XPS) show that STU can graft to the surface of SiO_2 under heating, resulting in a fine-dispersed structure in the rubber matrix without the connectivity of SiO_2 particles as revealed by transmission electron microscopy (TEM). This modification effect reduces the block vulcanization effect of SiO_2 for NR/SiO_2/STU compounds under vulcanization process evidently. The 400% modulus and tensile strength of NR/SiO_2/STU composites are much higher than that of NR/SiO2/TU composites, although the crystal index at the stretching ratio of 4 and crosslinking densities of NR/SiO_2 composites are almost the same at the same dosage of SiO_2. Consequently, a structure-property relationship of NR/SiO_2/STU composites is proposed that the silane chain of STU can entangle with NR molecular chains to form an interfacial region, which is in accordance with the experimental observations quite well.

Keywords: *rubber, multi-functional rubber agent, structure-property relationship, silica*

1. Introduction

In recent years, polymer/inorganic filler composites have attracted great attention, not only in industry, but also in academia, for inorganic filler, such as silica (SiO_2), montmorillonite and halloysite nanotube can introduce great improvement in the mechanical properties of polymer/inorganic filler composites even at low dosage of filler [1]. Among these fillers, silica is believed to be one of the most important inorganic fillers applied to reinforce rubber vulcanizates because the compounding of silica offers a number of advantages on the mechanical properties of vulcanizates, such as excellent thermal stability, tensile strength, good tear and abrasion resistance [2, 3]. However, because of great discrepancies in polarity between the non-polar diene polymer and polar silica, primary particles of SiO_2 tend to aggregate due to the thermo-dynamical incompatibility driving force caused by hydrogen bonds among primary particles [4, 5]. Research revealed that on a larger scale, up to macroscopic scale, the silica spatial distribution is homogeneous, with no sign of connectivity at 5% and with connectivity at 15% [6].

On the other hand, except for the well dispersion of SiO_2 particles, the interfacial adhesion between polymer matrix and SiO_2 particles is another essential factor for the mechanical properties of compos-

*Corresponding author, e-mail: zxjia@scut.edu.cn

ites [7], as the weak interfacial adhesion would cause catastrophic damages to the matrix under applied stress. Thus, improvements in the interfacial adhesion between the two phases, as well as good dispersion of inorganic filler particles, have been realized in the preparation of polymer-filler hybrid composites using coupling agents [8]. Nakamura *et al*. [9] investigated the effect of the number of siloxane units on the mechanical properties of polyisoprene/SiO_2 composites by using silanes with dialkoxy and trialkoxy structures. The reinforcement effect introduced by the silane treatment of silica was found depend strongly both on the entanglement between the silane chain and polyisoprene rubber matrix and on the crosslinking reaction between the mercapto group of silane and polyisoprene rubber in the interfacial region, which is in accordance with results from other researches [7]. However, silane coupling agents can only modify the surface of SiO_2, promoting a good dispersion of SiO_2 in the rubber matrix. It has been realized that, except for the fine-dispersion of filler in rubber matrix, if the silane coupling agents possess another function of rubber agents, like acceleration function, the properties of rubber composites will be significantly promoted [8].

Moreover, binary accelerator systems are being widely applied in the rubber industry and become increasingly popular based on the fact that such binary systems can effectively facilitate the vulcanization process to be carried out at a lower temperature within a short time [10–12]. Among these binary accelerator systems, thiourea (TU) and its derivatives are favorable for improvements in the vulcanization process and mechanical properties of rubber composites [13, 14]. Kurien and Kuriakose [15] synthesized a sort of TU derivative, namely amidino thiourea (ATU), and studied the vulcanization properties of NR with binary accelerator systems including tetramethylthiuram disulphide (TMTD), mercapto-benzothiazyl disulphide (MBTS), or cyclohexyl-benzthiazyl-sulphenamide (CBS). The induction time and optimum curing time of the formulations with ATU or TU were shorter than that of the control references without ATU or TU. However, all these TU derivatives only can accelerate the vulcanization process of rubber composites. Consequently, how to combine the accelerating property of TU and surface modification function of coupling agent together still attracted great attentions both in academy and in industry.

In this work, a multi-functional rubber agent, N-phenyl-N′-(γ-triethoxysilane)-propyl thiourea (STU), was used to prepare NR/SiO_2 composites and the vulcanization property, as well as structure-properties relationship, was investigated in detail.

2. Experimental

2.1. Materials

Natural rubber ISNR-3 was used, and the other ingredients, such as zinc oxide (ZnO), stearic acid (SA), N-cyclohexyl-2-benzothiazole sulfonamide (CBS), thiourea (TU) and sulfur (S) were commercial grades. Precipitated silica (SiO_2), with the particle diameter of about 900 nm and BET surface area of 144.44 m^2/g, was kindly supplied by Huiming Chemical Industry Co. Ltd, Wanzai County, China. The synthesis of STU was performed by mixing γ-aminopropyl triethoxysilane and phenyl isothiocyanate drop by drop in a stoichiometric level under the room temperature for 24 hours. The details in FTIR and ^{1}H-NMR of STU are given as follow:

FTIR, cm^{-1} (neat): 3275br, (ν_{NH}); 3060w, (ν_{CH}, arom.); 2974m, 2927m, 2887m (ν_{CH}, alif.); 1597m (phenyl); 1536s (ν_{CNC}, B-band); 1450m ($\nu_{C–C}$, arom.); 1165m ($\nu_{C=S}$); 1078s ($\nu_{Si–O–Et}$) [16–18].

^{1}H-NMR, δ ($CDCl_3$): 8.14 (w, 1H, N′H); 7.37 (m, 2H, $H_{m,m'}$); 7.26 (m, 1H, H_p); 7.18 (m, 2H, $H_{o,o'}$); 6.25 (w, 1H, NH); 3.73 (s, 6H, ethoxy CH_2); 3.61 (m, 2H, γ-CH_2); 1.68 (m, 2H,β-CH_2); 1.13 (s, 9H, ethoxy CH_3); and 0.55 (m, 2H, α-CH_2). The chemistry structure of STU is displayed in Figure 1.

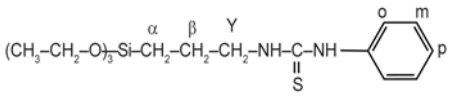

Figure 1. The chemistry structure of STU

2.2. Preparation of NR/SiO_2 compounds

The formulations of NR/SiO_2 compounds are summarized in Table 1 and Table 2.

NR was passed through the roller three times on an open two-roll mill (160 mm×320 mm) at room temperature with the nip gap of about 1 mm, then other ingredients, such as SiO_2, ZnO, SA, TU or STU, CBS and sulfur, were added to the glue stock one by one within ten minutes. After that, the compounds were stored for eight hours before the rheometer testing.

Table 1. The formulation of NR/SiO_2/STU composites [phr]

Sample	NR	STU	ZnO	SA	CBS	S	SiO_2
STU-SiO_2-0	100.0	0.92	5.0	2.0	2.64	1.5	0.0
STU-SiO_2-10	100.0	0.92	5.0	2.0	2.64	1.5	10.0
STU-SiO_2-20	100.0	0.92	5.0	2.0	2.64	1.5	20.0
STU-SiO_2-30	100.0	0.92	5.0	2.0	2.64	1.5	30.0
STU-SiO_2-40	100.0	0.92	5.0	2.0	2.64	1.5	40.0
STU-SiO_2-50	100.0	0.92	5.0	2.0	2.64	1.5	50.0

Table 2. The formulation of NR/SiO_2/TU composites [phr]

Sample	NR	TU	ZnO	SA	CBS	S	SiO_2
TU-SiO_2-0	100.0	0.20	5.0	2.0	2.64	1.5	0.0
TU-SiO_2-10	100.0	0.20	5.0	2.0	2.64	1.5	10.0
TU-SiO_2-20	100.0	0.20	5.0	2.0	2.64	1.5	20.0
TU-SiO_2-30	100.0	0.20	5.0	2.0	2.64	1.5	30.0
TU-SiO_2-40	100.0	0.20	5.0	2.0	2.64	1.5	40.0
TU-SiO_2-50	100.0	0.20	5.0	2.0	2.64	1.5	50.0

2.3. Characterization

The vulcanization research was carried out by a MDR (UR-2030SD, U-Can Limited Corporation, Taiwan, China) at 133°C. The compounds were cured at 133°C according to their optimum vulcanization time. The mechanical properties, such as 400% modulus, tensile strength, and elongation at break, were measured according to ISO/DIS37-1994 specifications. U-CAN electron tensile testing machine was used with the crosshead speed of 500 mm/min. All mechanical testing was undertaken at 25°C.

The possible chemical interactions between STU and SiO_2 were probed by infrared spectroscopy (IR) and X-ray photoelectron spectroscopy (XPS). For preparation of samples, SiO_2 and STU/SiO_2 (0.92/30, phr) model compounds were placed on a vulcanizing press machine at a setting time of 15 min under 133°C, followed by Soxhlet extraction experiment of the model compounds using boiling benzene (100°C) within 24 h, and then were dried to constant weight. The IR measurement of model compounds was recorded on a Bruker Vector 33 infrared spectroscopy in the range of 4000~400 cm^{-1}. Also, XPS spectra of the model compounds were recorded by using an X-ray photoelectron spectrometer (Kratos Axis Ultra DLD) with an aluminum (mono) K_α source (1486.6 eV). The aluminum K_α source was operated at 15 kV and 10 mA. All core level spectra were referenced to the C_{1s} neutral carbon peak at 284.7 eV.

The crosslinking density [19] test was performed on the base of swelling equilibrium measurement. The swelling equilibrium test was carried out by immersing samples in the toluene for 4 days. After that, the surface toluene was blotted off quickly with tissue paper. The specimens were immediately weighed on an analytical balance and then dried in a vacuum oven until the samples became constant weight and reweighed. The calculation was made according to the reference [20].

For the observation by transmission electron microscopy (TEM), the specimens were ultramicrotomed into thin pieces of about 100 nm in thickness with Leica EMUC6 under liquid nitrogen atmosphere. Then the observations were obtained using a Tecnai 12 transmission electron microscope (FEI Company, Holland) with an accelerating voltage of 100 kV.

The strain-induced crystallization (SIC) of NR/SiO_2 composites was performed on a WAXD apparatus (Philips X′ Pert PRO, Holland) with Ni-filtered Cu K_α radiation($\lambda = 0.154$ nm) at a generator voltage of 40 kV and generator current of 40 mA. The 2θ scanning rang was varied from 5 to 30°, with a step of 0.017° and a measuring time of 16.24 s per step. The degree of SIC (X_c) is calculated on the basis of peaks fitting during which a 2θ range from 10 to 30°, including crystalline and amorphous, was taken. X_c is defined as the ratio between the single integrated intensity of crystal (200 or 120 reflection was taken) A_c and the total integrated intensity of crystalline

and amorphous peaks A_{c+a} in the 2θ range, as expressed in the following Equation (1):

$$X_c = \frac{A_c}{A_{c+a}} \times 100\% \quad (1)$$

3. Results and discussions

3.1. Characterization of model compounds

3.1.1. IR spectroscopy

Figure 2 shows the IR spectra of SiO_2 and STU/SiO_2 model compounds. The peaks at 3441 and 1103 cm^{-1} are assigned to the stretching vibrations of –OH groups on the surface of SiO_2 and Si–O groups, respectively. In the spectrum of STU/SiO_2 model compounds, the stretching vibration of Si–O groups does not change, whereas the peak at 3423 cm^{-1} is associated with the stretching vibration of –NH groups with the bending vibration at 1550 cm^{-1}. Two reasons may be responsible for the unconspicuous representation of –OH groups. First, partial hydroxyl groups have reacted with the siloxane groups of STU, leading to a decrease in the amount of –OH groups. Second, the silane molecules have grafted to SiO_2 particles and covered on the surface of SiO_2 particles, which would give rise to the shielding effect for –OH groups. In the dotted line ellipse domain, the peaks located at 2983 and 2945 cm^{-1} are ascribed to stretching vibrations of methyl and methylene. Moreover, the characteristic stretching vibrations of benzene ring (1597 cm^{-1}) and C=S (1165 cm^{-1}) have disappeared, illuminating that a pyrolysis reaction of STU occurs during heating press [21].

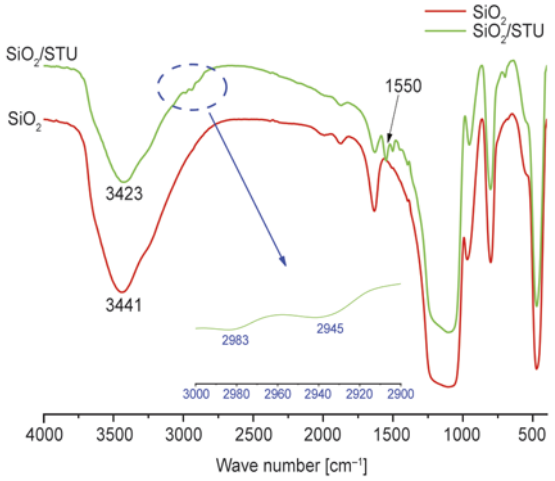

Figure 2. The IR spectra of SiO_2 and STU/SiO_2 model compounds

3.1.2. XPS analysis

In order to substantiate the formation of chemical bonds between SiO_2 and STU, XPS survey was performed on the model compounds. The formation of

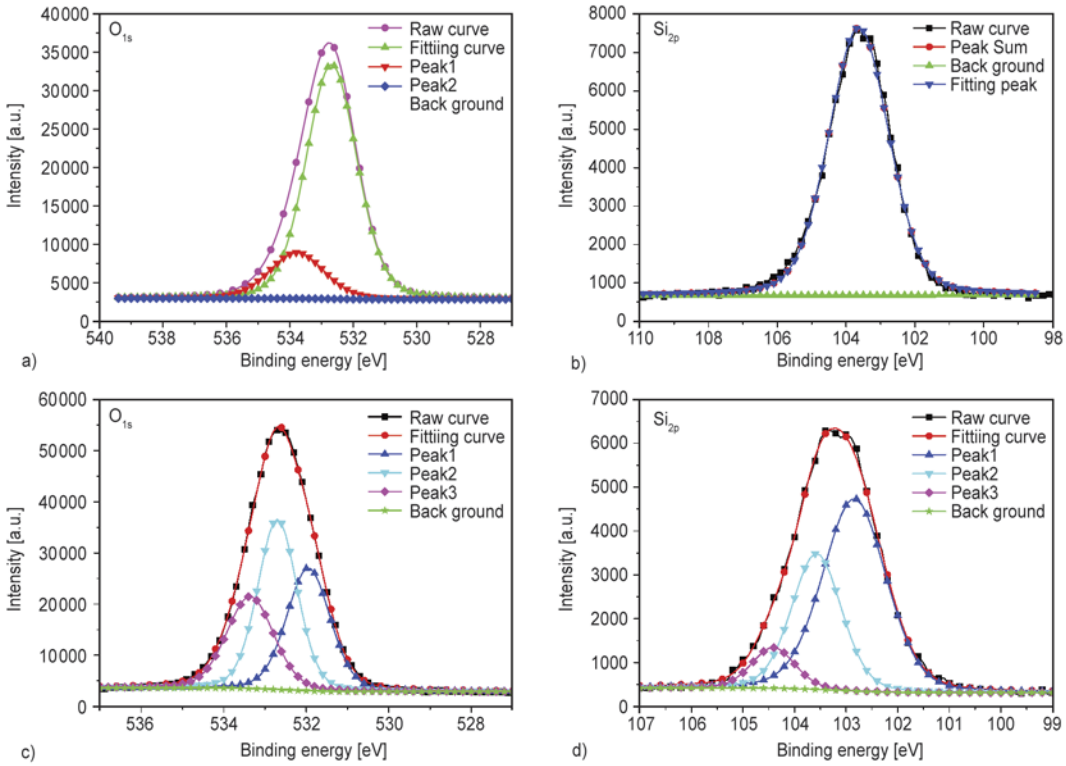

Figure 3. The XPS fitting peaks of model compounds: a) O_{1s} and b) Si_{2p} of SiO_2; c) O_{1s} and d) Si_{2p} of STU/SiO_2

Table 3. The characteristic parameters of fitting peaks of model compounds SiO_2 and STU/SiO_2

Sample	Si_{2p}			O_{1s}		
SiO_2	–	103.6	–	–	532.7	533.8
STU/SiO_2	102.8	103.6	104.4	532.0	532.7	533.4

chemical bond will cause a variation in the binding energies of certain atoms related to the chemical bond. The XPS spectra of SiO_2 and STU/SiO_2 model compounds are depicted in Figure 3 and Table 3. The characteristic signal due to silicon (Si_{2p} at 103.6 eV) of SiO_2 is detected, meanwhile, that for STU/SiO_2 model compounds is split into three characteristic signals, 102.8, 103.6 and 104.4 eV, respectively, indicating two new different chemical environments of silicon atom have been introduced to the surface of SiO_2. Moreover, one can see that there are two different binding energies, 532.7 and 533.8 eV, of O_{1s} in pure SiO_2, whereas, three evident peaks are found in the O_{1s} spectra of STU/SiO_2 model compounds, confirming the successful modification of SiO_2 particles by STU, as shows in Figure 4. The silanol groups of STU can react with the hydroxyl groups on the surface of SiO_2 with the elimination of ethanol [8] and phenyl isothiocyanate molecules under heating. The modification of SiO_2 will further prohibit the agglomeration of SiO_2 particles, as well as the physical adsorption of SiO_2 to rubber agents.

3.2. Vulcanization property of NR/SiO_2 compounds

The vulcanization parameters of NR/SiO_2/TU compounds and NR/SiO_2/STU compounds are showed in Table 4 and Table 5, separately. In Table 4, the scorch time (T_{s1}) and optimum curing time (T_{c90}) increase with increasing SiO_2, even at low SiO_2 dosage, indicating that SiO_2 particles can delay the vulcanization process. From the lowest torque (*ML*), *ML* value, as well as the *MH* value, dramatically change with the incorporation of SiO_2, elucidating a bad dispersion of SiO_2, that is, particles connectivity, in the NR matrix. In Table 5, the scorch time (T_{s1}) and optimum curing time (T_{c90}) also increase with increasing SiO_2, however, compared with NR/SiO_2/TU compounds, one can see that a

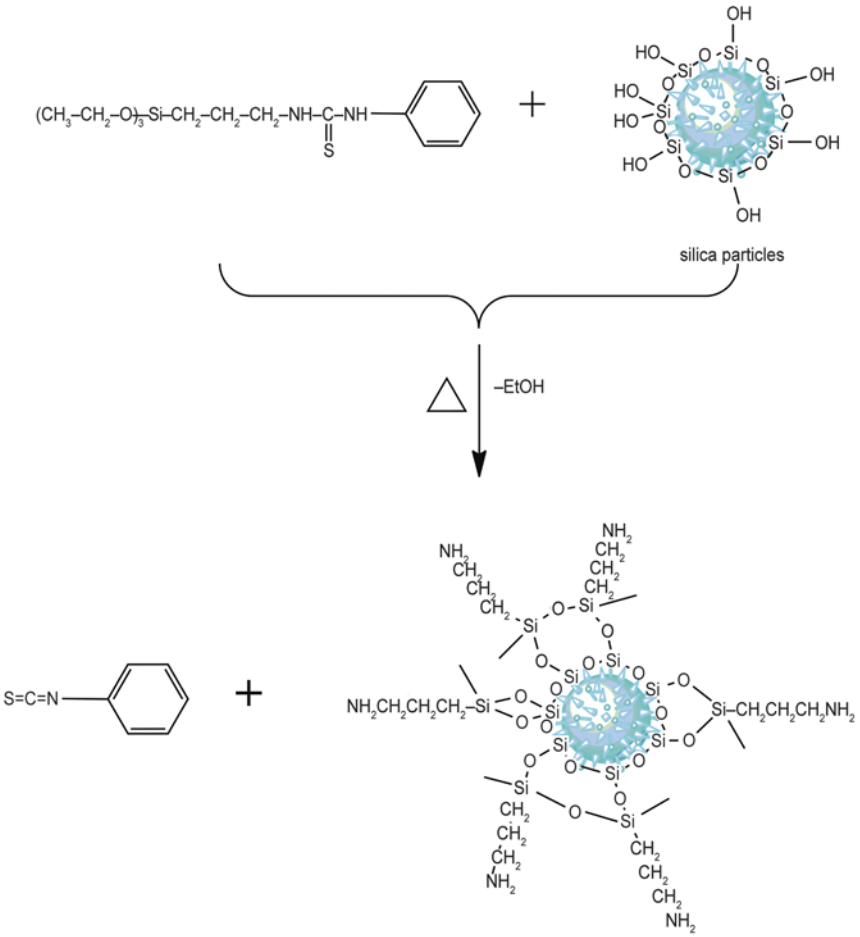

Figure 4. Schematic of STU modified silica particles

Table 4. The curing characteristics of NR/SiO_2/TU compounds (133°C)

Sample	T_{s1} [min]	T_{c90} [min]	ML [dN·m]	MH [dN·m]
TU-SiO_2-0	1.68	6.77	0.08	13.71
TU-SiO_2-10	5.30	11.10	0.28	15.15
TU-SiO_2-20	8.68	16.13	0.39	17.30
TU-SiO_2-30	8.90	17.78	1.16	22.60
TU-SiO_2-40	6.98	18.27	2.79	28.37
TU-SiO_2-50	9.03	28.27	4.08	31.07

Table 5. The curing characteristics of NR/SiO_2/STU compounds (133°C)

Sample	T_{s1} [min]	T_{c90} [min]	ML [dN·m]	MH [dN·m]
STU-SiO_2-0	3.10	8.15	0.05	13.20
STU-SiO_2-10	4.75	9.81	0.10	14.43
STU-SiO_2-20	5.63	10.97	0.10	14.97
STU-SiO_2-30	6.97	13.52	0.30	18.97
STU-SiO_2-40	8.27	18.85	1.75	26.27
STU-SiO_2-50	9.53	26.53	5.21	32.66

more moderate increase in the NR/SiO_2/STU compounds, suggesting a lower physical adsorption of SiO_2 particles to rubber agents. Meanwhile, when the incorporation of SiO_2 is lower than 30 phr, the *ML* or *MH* of NR/SiO_2/STU compounds evolves to high value slightly, which is quite different from NR/SiO_2/TU compounds. This can be attributed to the modified effect of STU.

3.3. Morphology of NR/SiO_2 composites

TEM technology is competent for analyzing the dispersed morphology of SiO_2 particles in the rubber matrix. Figure 5 is the TEM graphs of STU-SiO_2-30 vulcanizate (a) and TU-SiO_2-30 vulcanizate (b). As is readily seen, a result can be expected that the dispersion degree of Figure 5a seems to be more homogeneous than Figure 5b, which suggests that STU facilitates SiO_2 particles to disperse in NR matrix uniformly. In Figure 5a, the size of silica aggregation is reduced to a certain extent and not evident connectivity of SiO_2 particles is found, that is, the SiO_2 particles aggregations have been isolated by NR rubber matrix due to the modified effect of STU, as depicts in Figure 4. However, in Figure 5b, an opposite phenomenon is observed that SiO_2 particles trend to agglomerate seriously and the connectivity between particles has been formed, which can be assigned to the formation of hydrogen bonds among SiO_2 particles by thermodynamical driving force [7] and the huge difference in compatibility between silica particles and NR matrix.

3.4. Strain-induced crystallization (SIC) of NR/SiO_2 composites

It has been recognized long ago that the excellent tensile property of NR originates from SIC. The details of strain-induced crystallization of NR/SiO_2

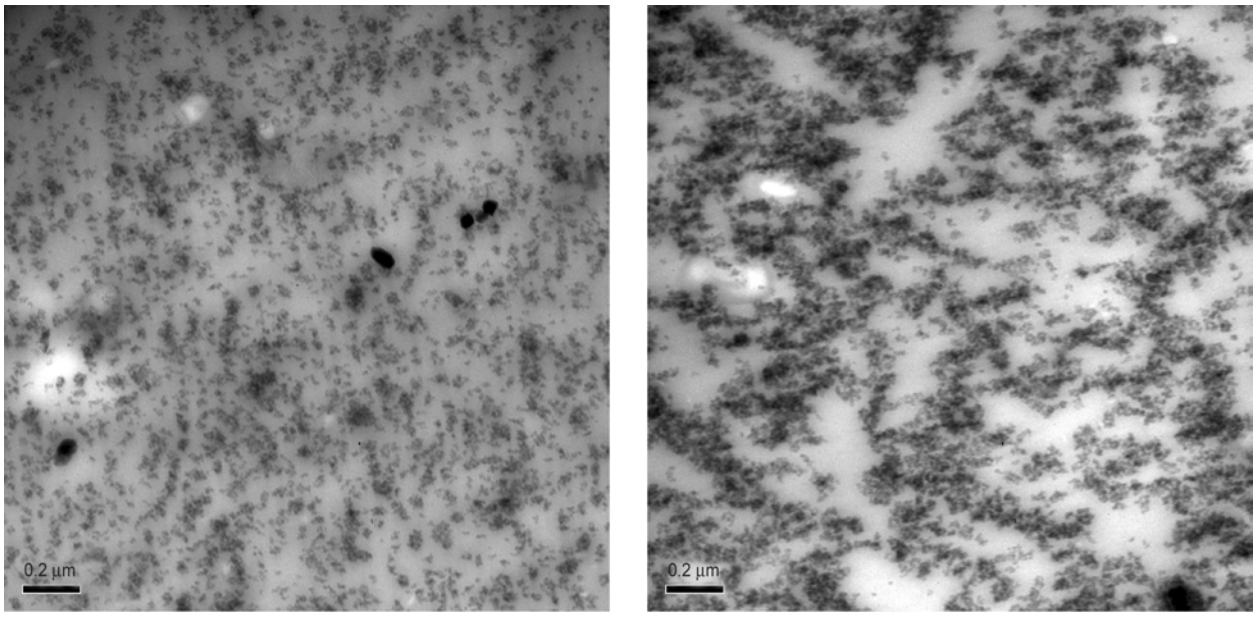

a) b)

Figure 5. The TEM photographs of STU-SiO_2-30 vulcanizate (a) and TU-SiO_2-30 vulcanizate (b)

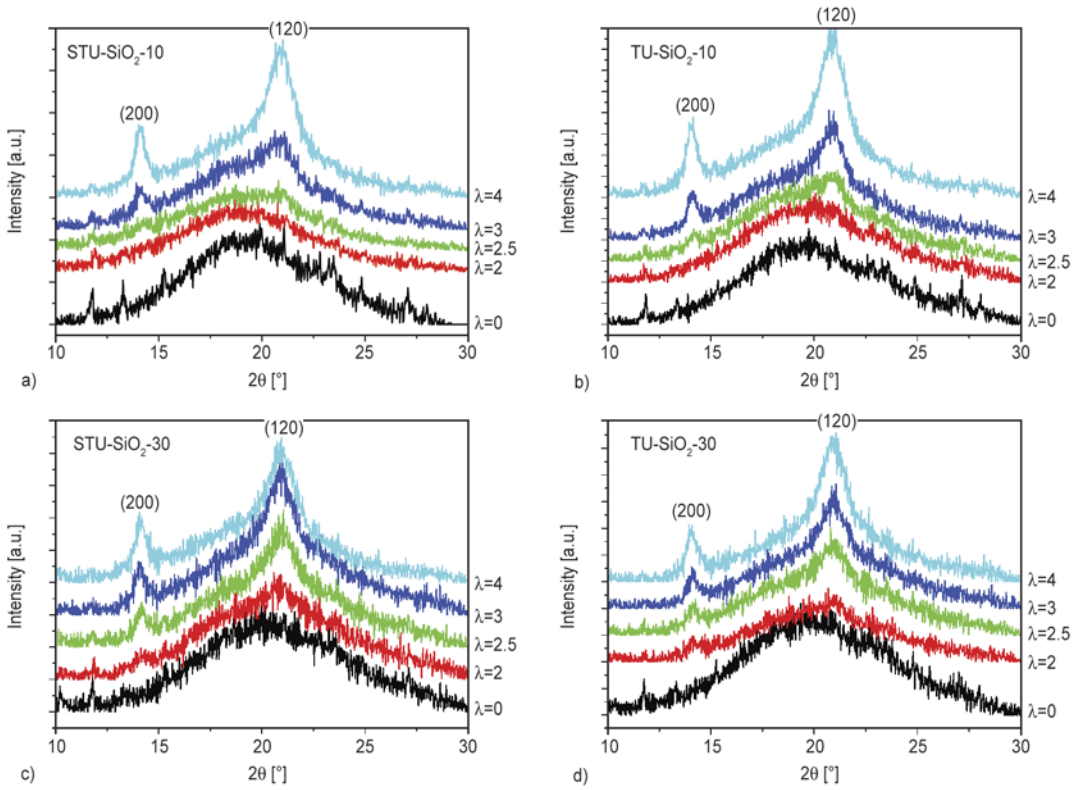

Figure 6. Equatorial diffraction profiles at selected strain values of vulcanizates as a function of strain under stretching at the 2θ angle range of 5–30°: STU-SiO_2-10 vulcanizate (a), TU-SiO_2-10 vulcanizate (b), STU-SiO_2-30 vulcanizate (c) and TU-SiO_2-30 vulcanizate (d)

composites experiments have been expressed in section 2.3. and the crystal index (CI) is calculated according to Equation (1). In this section, four NR/SiO_2 composites, STU-SiO_2-10, STU-SiO_2-30, TU-SiO_2-10 and TU-SiO_2-30, is adopted to illuminate the SIC of NR/SiO_2 composites according to the dispersion state of SiO_2 in the NR matrix. The diffraction profiles of STU-SiO_2-10, STU-SiO_2-30, TU-SiO_2-10 and TU-SiO_2-30 under different ratio at the 2θ angle range of 5–30° are shown in Figure 6, indicating that NR is a typical strain-induced crystallization material. Figure 7 illuminates the strain dependence of CI of NR/SiO_2 composites. In Figure 7a, when the stretching ratio is lower than 2.5,

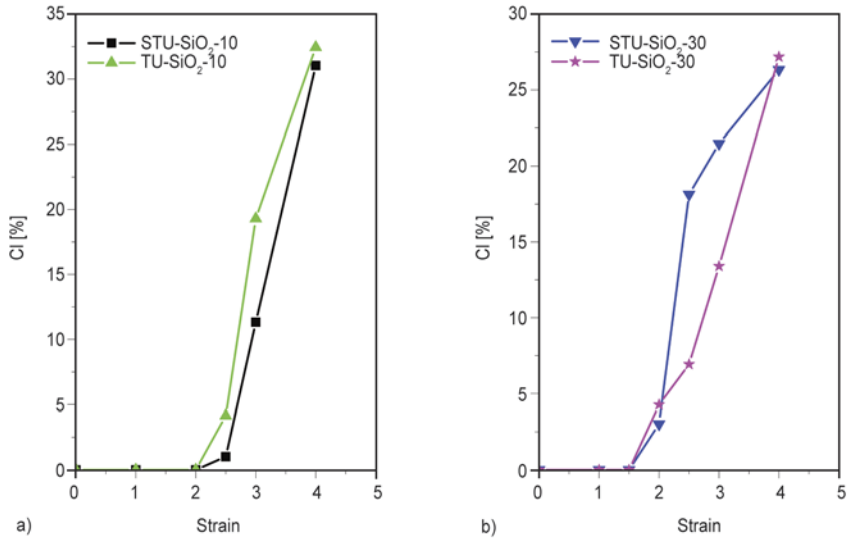

Figure 7. Variation of CI of NR with different vulcanization systems during the stretching process: filler content at 10 phr (a) and filler content at 30 phr (b)

not crystallization can be observed in STU-SiO_2-10 and TU-SiO_2-10 composites. After that, a steep upturning appears, indicating the orientated NR molecules begin to crystallize. The SIC rate of TU-SiO_2-10 is higher than that of STU-SiO_2-10, however, as the stretching ratio reaches 4, the CI is not apparent difference between STU-SiO_2-10 and TU-SiO_2-10. As one can see in Figure 7b, the initial crystallization strains of STU-SiO_2-30 and TU-SiO_2-30 are at the stretching ratio of 2, suggesting the incorporation of SiO_2 induces the NR molecules to crystallize. With respect to Figure 7a, the SIC rate of STU-SiO_2-30 increases faster than that of TU-SiO_2-30 at the stretching ratio of 2~3, illustrating the rubber molecules in STU-SiO_2-30 are readily to orientate. At the stretching ratio of 4, the CI is almost the same between STU-SiO_2-30 and TU-SiO_2-30.

3.5. Structure-property relationship of NR/SiO_2 composites

The stress-strain behavior of NR/SiO_2 composites is displayed in Figure 8 and Table 6. Compared the difference between *ML* and *MH* ($\Delta M = MH - ML$) in Table 4 and 5 with the crosslinking densities in Table 6 for NR/SiO_2 composites, the discrepancy between ΔM and crosslinking density is mainly attributed to the hydrodynamic volume effect of filler and the hardness discrepancy between filler and rubber [22]. In the NR/SiO_2/STU composites, the tensile strength increases with increasing SiO_2. As the addition of SiO_2 reaches 30 phr, the maximum tensile strength is about 30.75 MPa, following by a decrease in the tensile strength with increasing SiO_2, which is the same trend for NR/SiO_2/TU composites. However, the maximum tensile strength for NR/SiO_2/TU composites is only 25.52 MPa at the SiO_2 content of 30 phr, which is much lower than that of NR/SiO_2/STU composites. As is shown in Figure 7, the CI of NR/SiO_2 composites are almost the same at the stretching ratio of 4, so in this work, for distinct understanding of the enhancement of STU, 400% modulus of NR/SiO_2 composites is acquired, rather than 100 and 300% modulus. 400% modulus of NR/SiO_2/STU composites is higher than that of NR/SiO_2/TU composites at the same addition of SiO_2, suggesting that the reinforcing mechanism of NR/SiO_2/STU composites is quite different from NR/SiO_2/TU composites.

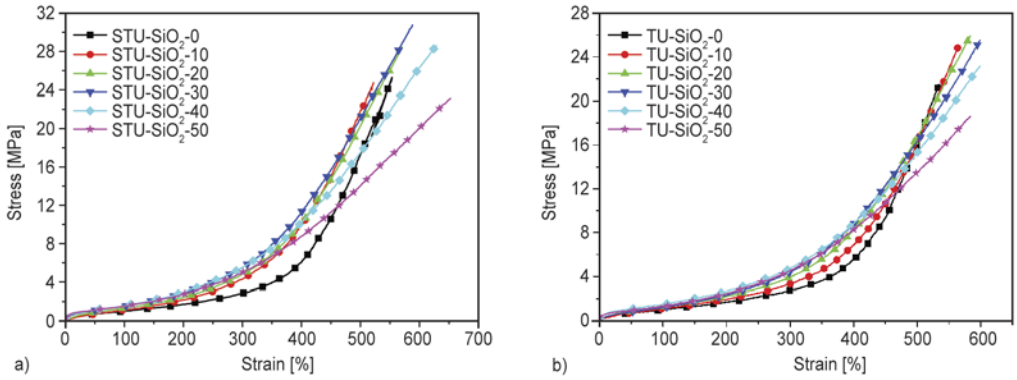

Figure 8. The stress-strain behavior of NR/SiO_2/STU composites (a) and NR/SiO_2/TU composites (b)

Table 6. The mechanical performance of NR/SiO_2 composites

Sample	400% Modulus [MPa]	Tensile-strength [MPa]	Elongation at break [%]	V_e [10^{-4}]
STU-SiO_2-0	6.08	25.29	553	1.2290
STU-SiO_2-10	9.94	24.74	522	1.2180
STU-SiO_2-20	10.14	28.35	573	1.0540
STU-SiO_2-30	11.26	30.75	609	0.9768
STU-SiO_2-40	10.25	28.36	627	0.8505
STU-SiO_2-50	8.73	23.11	646	0.5979
TU-SiO_2-0	5.53	21.49	534	1.2050
TU-SiO_2-10	6.84	24.71	578	1.1140
TU-SiO_2-20	8.27	25.09	584	1.0180
TU-SiO_2-30	8.79	25.52	602	0.8608
TU-SiO_2-40	8.81	22.95	599	0.7152
TU-SiO_2-50	8.29	18.07	592	0.5148

It is well known that the stress-strain behavior for filler filled rubber systems is affected by the crosslinking density [23], the size of agglomerates formed by filler [24], rubber/filler interactions [7, 23] and CI (only for crystal polymer) of rubber matrix. In Table 6 and Figure 7, the crosslinking density (V_e) and total CI are almost the same for NR/SiO_2/STU composites and NR/SiO_2/TU composites at the same dosage of SiO_2, indicating that these three factors on mechanical properties of NR/SiO_2 composites can be ignored. Two main reasons may be taken into consideration to represent the higher mechanical properties of NR/SiO_2/STU composites. First, as depicts in section 3.3. and Figure 5, the modified effect of STU gives rise to a fine-dispersion structure of SiO_2 in the NR matrix, leading to the small-size effect and less defects in the interphase of NR matrix and SiO_2 particles [7]. Second, the mechanical properties are found to be affected strongly by the entanglement, maybe the predominant reason, between the silane chain and NR matrix at the interfacial region, as illuminates in Figure 9. As described above, STU molecular chain, more exactly the silane chain, can graft to the surface of SiO_2 particles by the reactions between the silanol groups and hydroxyl groups of SiO_2 under heating. According to the theory similar molecules dissolve mutually, the silane chain can dissolve in the NR matrix, as in Figure 9a, leading to entanglement between these two molecular chains

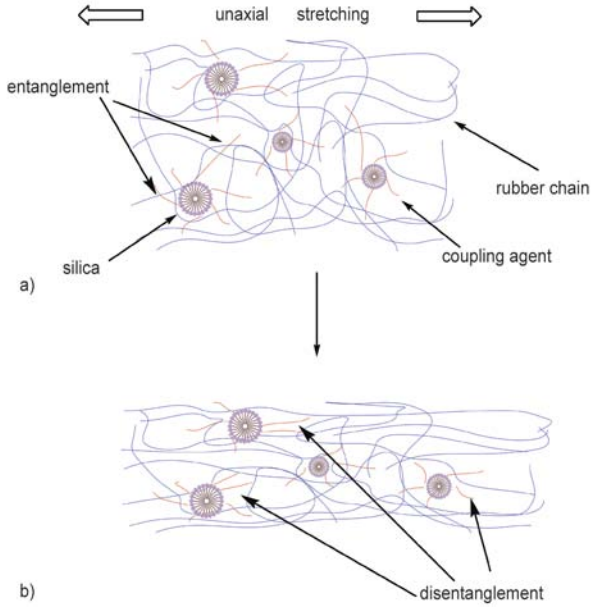

Figure 9. The reinforcement mechanism of STU modified SiO_2 in the NR/SiO_2/STU composites: before stretching (a) and after stretching (b)

at the interfacial region. When an exerted stress is applied to the matrix, the stress runs along the rubber chain, the reinforcement effect of the formed interfacial region becomes more effective to influence the modulus of NR/SiO_2/STU composites, leading to a much higher 400% modulus in the NR/SiO_2/STU composites than that of NR/SiO_2/TU composites at the same addition of SiO_2. As in Figure 9b, when the exerted stress continues to increase, the deformation of 'rubber depletion layer' (often a few nm distances away or larger [7, 25]) surrounding SiO_2 particles would develop [7]. If there are no interactions between NR matrix and SiO_2 particles, decohesion would happen at the interfacial region, following by a catastrophic breakage to the composites under a low tensile strength, like the NR/SiO_2/TU composites. On the other hand, when an entanglement exists in the interfacial region, like NR/SiO_2/STU composites, the stress will pass from NR molecular chains to the filler effectively before disentanglement happens. At the same time, the NR main chains can slip on the SiO_2 particles surface with the help of silane chains, allowing the network to relax to a more perfect regime and changing the local stress condition by means of stress homogenized distribution. These will lead to a much higher 400% modulus and tensile strength in the composites, like STU-SiO_2-30, before disentanglement.

4. Conclusions

Vulcanization property and structure-property relationship of NR/SiO_2 composites modified by a novel multi-functional rubber agent, STU, are explored thoroughly. From the IR and XPS spectra, STU can graft to the surface of SiO_2 under heating, reducing the block vulcanization effect of SiO_2 for rubber vulcanization due to the reduction in the physical adsorption of SiO_2 particles to rubber agents. From the graphs of TEM, STU can facilitate a fine-dispersed structure in the rubber matrix without any connectivity of SiO_2 particles, whereas, for NR/SiO_2 composites without modification, serious aggregation of SiO_2 particles is found. Moreover, the strain-induced crystallization at the stretching ratio of 4 and the crosslinking densities of NR/SiO_2 composites are almost the same at the same dosage of SiO_2. However, the 400% modulus and tensile strength of NR/SiO_2/STU composites are much higher than that of NR/SiO_2/TU composites. Finally, a structure-property relationship of NR/SiO_2/STU composites is

proposed that the silane chain of STU can entangle with NR molecular chains to form an interfacial region. When an exerted stress is applied to the matrix, the stress runs along the rubber chain, the reinforcement effect of the formed interfacial region became more effective to the mechanical properties of NR/SiO_2/STU composites.

Acknowledgements

The authors gratefully acknowledge the financial support from Guangdong Province Joint Funds of the National Natural Science Foundation of China (No. U1134005) and The National Natural Science Funds of China (No.51303026) and Strategic new industry core technology research project of Guangdong Province (2012A090100017).

References

[1] Xiong L., Liang H., Wang R., Chen L.: A novel route for the synthesis of poly(2-hydroxyethyl methacrylate-co-methyl methacrylate) grafted titania nanoparticles via ATRP. Journal of Polymer Research, **18**, 1017–1021 (2011).
DOI: 10.1007/s10965-010-9502-5

[2] Peng H., Liu L., Luo Y., Hong H., Jia D.: Synthesis and characterization of 3-benzothiazolthio-1-propyltriethoxylsilane and its reinforcement for styrene–butadiene rubber/silica composites. Journal of Applied Polymer Science, **112**, 1967–1973 (2009).
DOI: 10.1002/app.29634

[3] Peng H., Liu L., Luo Y., Jia D., Fu W.: Novel blocked mercaptosilane (3-propionylthio-1-propyltrimethoxylsilane) for natural rubber/silica composite reinforcement in various curing systems. e-Polymers, **8**, 1190–1198 (2008).
DOI: 10.1515/epoly.2008.8.1.1190

[4] Murakami K., Iio S., Ikeda Y., Ito H., Tosaka M., Kohjiya S.: Effect of silane-coupling agent on natural rubber filled with silica generated *in situ*. Journal of Materials Science, **38**, 1447–1455 (2003).
DOI: 10.1023/A:1022908211748

[5] Yun S. H., Cho D., Kim J., Lim S., Lee G-W., Park M., Lee S-S.: Effect of silane coupling agents with different organo-functional groups on the interfacial shear strength of glass fiber/nylon 6 composites. Journal of Materials Science Letters, **22**, 1591–1594 (2003).
DOI: 10.1023/A:1026384408153

[6] Jouault N., Vallat P., Dalmas F., Said S., Jestin J., Boué F.: Well-dispersed fractal aggregates as filler in polymer–silica nanocomposites: Long-range effects in rheology. Macromolecules, **42**, 2031–2040 (2009).
DOI: 10.1021/ma801908u

[7] Yang S., Liu L., Jia Z., Jia D., Luo Y.: Structure and mechanical properties of rare-earth complex La-GDTC modified silica/SBR composites. Polymer, **52**, 2701–2710 (2011).
DOI: 10.1016/j.polymer.2011.04.015

[8] Peng H., Liu L., Luo Y., Wang X., Jia D.: Effect of 3-propionylthio-1-propyltrimethoxylsilane on structure, mechanical, and dynamic mechanical properties of NR/silica composites. Polymer Composites, **30**, 955–961 (2009).
DOI: 10.1002/pc.20640

[9] Nakamura Y., Honda H., Harada A., Fujii S., Nagata K.: Mechanical properties of silane-treated, silica-particle-filled polyisoprene rubber composites: Effects of the loading amount and alkoxy group numbers of a silane coupling agent containing mercapto groups. Journal of Applied Polymer Science, **113**, 1507–1514 (2009).
DOI: 10.1002/app.30155

[10] Choi S-S.: Improvement of properties of silica-filled natural rubber compounds using polychloroprene. Journal of Applied Polymer Science, **83**, 2609–2616 (2002).
DOI: 10.1002/app.10201

[11] González L., Rodríguez A., Del Campo A., Marcos-Fernández A.: Crosslink reaction of natural rubber with thiuram sulphur donors in the presence of a thiuram monosulfide. Journal of Applied Polymer Science, **85**, 491–499 (2002).
DOI: 10.1002/app.10438

[12] Susamma A. P., Mini V. T. E., Kuriakose A. P.: Studies on novel binary accelerator system in sulfur vulcanization of natural rubber. Journal of Applied Polymer Science, **79**, 1–8 (2001).
DOI: 10.1002/1097-4628(20010103)79:1<1::AID-APP10>3.0.CO;2-V

[13] Susamma A. P., Claramma N. M., Nair A. B., Kuriakose A. P.: New binary systems containing TMTD-amidino phenyl thiourea and CBS–amidinophenyl thiourea for the vulcanization and rheological behavior of natural rubber latex. Journal of Applied Polymer Science, **115**, 2310–2316 (2010).
DOI: 10.1002/app.31360

[14] Aprem A. S., Joseph K., Mathew T., Volker A., Sabu T.: Studies on accelerated sulphur vulcanization of natural rubber using 1-phenyl-2, 4-dithiobiuret/tertiary butyl benzothiazole sulphenamide. European Polymer Journal, **39**, 1451–1460 (2003).
DOI: 10.1016/S0014-3057(02)00382-8

[15] Kurien M., Kuriakose A. P.: Studies on sulphur vulcanisation of natural rubber using amidino thiourea. Plastics, Rubber and Composites, **30**, 263–269 (2001).
DOI: 10.1179/146580101101541688

[16] Cauzzi D., Costa M., Cucci N., Graiff C., Grandi F., Predieri G., Tiripicchio A., Zanoni R.: Pd(II) and Rh(I) chelate complexes of the bidentate phosphino–thiourea ligand $PhNHC(S)NHCH_2CH_2PPh_2$: Structural properties and activity in homogeneous and hybrid catalysis. Journal of Organometallic Chemistry, **593–594**, 431–444 (2000).
DOI: 10.1016/S0022-328X(99)00615-4

[17] Angelova D., Armelao L., Gross S., Kickelbick G., Seraglia R., Tondello E., Trimmel G., Venzo A.: Investigation of thiourea-silanes as viable precursors for the sol–gel synthesis of composites containing Zn–S complexes. Applied Surface Science, **226**, 144–148 (2004).
DOI: 10.1016/j.apsusc.2003.11.014

[18] Angelova D., Armelao L., Barison S., Fabrizio M., Gross S., Sassi A., Seraglia R., Tondello E., Trimmel G., Venzo A.: Sol–gel synthesis of Zn-thiourea-SiO_2 thin films from $(EtO)_3Si(CH_2)_3NHC(=S)NHPh$ as molecular precursor. Solid State Sciences, **6**, 1287–1294 (2004).
DOI: 10.1016/j.solidstatesciences.2004.06.007

[19] Flory P. J.: Statistical mechanics of swelling of network structures. The Journal of Chemical Physics, **18**, 108–111 (1950).
DOI: 10.1063/1.1747424

[20] Yang S., Liu L., Jia Z., Jia D., Luo Y., Liu Y.: Studies on the influence of lanthanum glutamic dithiocarbamate on the interfacial reinforncement of SBR/SiO_2 composites by swelling equilibrium test. Acta Polymerica Sinica, **52**, 709–719 (2011).
DOI: 10.3724/SP.J.1105.2011.10184

[21] Yang S. Y., Jia Z. X., Liu L., Fu W. W., Jia D. M., Luo Y. F.: New insight into the vulcanization mechanism of novel binary accelerators for natural rubber. Chinese Journal of Polymer Science, in press (2014).

[22] Yang S., Liu L., Jia Z., Jia D., Luo Y.: Study on the curing properties of SBR/La-GDTC/SiO_2 composites. Journal of Rare Earths, **29**, 444–453 (2011).
DOI: 10.1016/S1002-0721(10)60477-2

[23] Yatsuyanagi F., Suzuki N., Ito M., Kaidou H.: Effects of surface chemistry of silica particles on the mechanical properties of silica filled styrene–butadiene rubber systems. Polymer Journal, **34**, 332–339 (2002).
DOI: 10.1295/polymj.34.332

[24] Suzuki N., Yatsuyanagi F., Ito M., Kaidou H.: Effects of surface chemistry of silica particles on secondary structure and tensile properties of silica-filled rubber systems. Journal of Applied Polymer Science, **86**, 1622–1629 (2002).
DOI: 10.1002/app.11050

[25] Starr F. W., Schrøder T. B., Glotzer S. C.: Molecular dynamics simulation of a polymer melt with a nanoscopic particle. Macromolecules, **35**, 4481–4492 (2002).
DOI: 10.1021/ma010626p

eXPRESS Polymer Letters Vol.8, No.6 (2014) 436–449
Available online at www.expresspolymlett.com
DOI: 10.3144/expresspolymlett.2014.47

Interactive effects between carbon allotrope fillers on the mechanical reinforcement of polyisoprene based nanocomposites

S. Agnelli[1], *V. Cipolletti*[2], *S. Musto*[2], *M. Coombs*[3], *L. Conzatti*[4], *S. Pandini*[1], *T. Riccò*[1], *M. Galimberti*[2,5*]

[1]Università degli Studi di Brescia, Via Valotti 9, 25123 Brescia, Italy
[2]Politecnico di Milano, Via Mancinelli 7, 20131 Milano, Italy
[3]Pirelli Tyre, Viale Sarca 222, 20126 Milano, Italy
[4]Consiglio Nazionale delle Ricerche, ISMAC UOS Genova, Via De Marini 6, 16149 Genova, Italy
[5]Consiglio Nazionale delle Ricerche, ISMAC, Via E. bassini 15, 20133, Milano, Italy

Received 11 November 2013; accepted in revised form 22 February 2014

Abstract. Interactive effects of carbon allotropes on the mechanical reinforcement of polymer nanocomposites were investigated. Carbon nanotubes (CNT) and nano-graphite with high shape anisotropy (nanoG) were melt blended with poly(1,4-cis-isoprene), as the only fillers or in combination with carbon black (CB), measuring the shear modulus at low strain amplitudes for peroxide crosslinked composites. The nanofiller was found to increase the low amplitude storage modulus of the matrix, with or without CB, by a factor depending on nanofiller type and content. This factor, fingerprint of the nanofiller, was higher for CNT than for nanoG. The filler-polymer interfacial area was able to correlate modulus data of composites with CNT, CB and with the hybrid filler system, leading to the construction of a common master curve.

Keywords: *nanomaterials, carbon nanotubes, nanographite, carbon black, interactive effects*

1. Introduction

Nanofillers have a great effect on polymer properties [1, 2], as the nano-size of such particles implies a high surface area that leads to a high interfacial area with the polymer and to the formation of filler networks at very low nanofiller concentrations.

Nowadays, most investigated nanofillers are carbon nanotubes (CNT) [1–4], graphene, a two-dimensional sheet made of sp^2-hybridized carbon atoms in an extended honeycomb network [5], and graphitic nanofillers [6–9] made by few layers of graphene (GE), usually indicated as graphite nanoplatelets, graphite nanosheets, graphite nanoflakes or just simply exfoliated or expanded graphite. Reviews are available on polymer nanocomposites (PNC) based on these types of nanofillers [8–11]. In polymer melts and elastomers, the formation of networks at low nanofiller concentration leads to high values of the dynamic modulus at low strain amplitudes, that goes however along with a pronounced reduction as the strain amplitude increases, phenomenon known as Payne effect [12]. Most studies reported in literature refer to PNC made by a single type of carbon nanofiller in a neat polymer matrix. However, an increasing interest is for elastomer based composites with hybrid filler systems, with a carbon nanofiller combined with the so-called nanostructured filler, carbon black (CB). In fact, the use of hybrid filler systems is considered to make it easier a large scale application of nanofillers.

*Corresponding author, e-mail: maurizio.galimberti@polimi.it

Papers have been published on PNC based on CB and either CNT or nano-graphite. In the case of elastomer polymer matrices, synergistic effects were envisaged [4] for CNT-CB system. CB particles were demonstrated to improve CNT dispersion in a styrene-co-butadiene copolymer matrix [13]. CNT were shown to interact with the surface of CB (N330) and good improvements in mechanical properties and electrical conductivity were reported, with a percolation threshold lower than that obtained with only CNT [13]. For such systems, connected filler structures were observed and commented [14]. In the case of a polyolefin elastomer (EPDM) [15], an enhancement of the mechanical reinforcement was reported to arise even by adding a small amount of CNT (about 3 php) to a considerable higher content of CB (N550, 40 php). A very high electrical conductivity was measured, much higher than that due to CB alone. In acrylonitrile-co-butadiene copolymer [16], it was reported that CNT (up to 9 php) and a conductive CB (20 or 40 php) induce reinforcing effects on tensile modulus and strength. Papers are as well available with nano-graphite and CB as the hybrid filler system. In NBR as the matrix, it was found [17] that the coefficient of friction and the specific wear rate were reduced when CB is associated to the nano-graphite, thanks to the formation of graphite lubricant films. In natural rubber as the polymer matrix (with epoxidized natural rubber as the compatibilizer), improvements of mechanical, thermal and dynamic-mechanical properties were observed [18] when the nanographite was added to CB (N234).

Previous research of the authors on PNC with hybrid carbon fillers in a poly(1,4-cis-isoprene) (PI) matrix revealed a dramatic enhancement of the material initial modulus, when a small content of nanofiller was added to a composite containing a prevailing amount of CB (N326, 60 php) [19, 20], and also a remarkable reduction of the modulus with the increase of the strain amplitude. In the case of CNT as the nanofiller [19], transmission electron microscopy (TEM) analysis documented the formation of hybrid CNT-CB networks at very low CNT content (about 2 php). The initial modulus values of the nanocomposites containing the hybrid CNT-CB filler network were found to be much higher than those calculated through the simple addition of the initial moduli of the composites containing only CB and only CNTs, and synergism between the two fillers was thus commented [19]. In ref. [20], CB was used in combination with a nano-graphite with a high shape anisotropy [21] (hereinafter nanoG), defined as the ratio between the crystallites dimensions in directions orthogonal and parallel to structural layers. Hybrid nanoG-CB networks were observed in TEM micrographs from a nanoG level of about 8 php and synergistic effects between nanoG and CB were observed on the initial moduli values of the nanocomposites containing the hybrid filler network.

It can be thus concluded that most prior art indicates a favourable interaction between two carbon allotropes, as it could be expected. In fact, also studies on zeta potential, a measure of the repulsion, in a dispersion, between similarly charged particles, lead to hypothesize an intimate interaction of CB and a nanofiller [22–24].

In the light of these findings and taking into consideration that experiments reported in the literature do not allow an overall rationalization, as data were collected with different types of carbon allotropes at different concentrations in the polymer matrix, it appeared to us worthwhile to perform a more systematic investigation of the interaction between CB and either CNT or nanoG. The aim was to understand the mechanisms that promote filler network formation and thus the stiffness of the material but also the pronounced non linearity of the dynamic-mechanical properties for polymer melts and elastomers. It is worth underlining that such non linearity means dissipation of energy. For example, this hinders nowadays a large scale application of carbon nanofillers in elastomeric materials. A series of composites were prepared in PI as the polymer matrix: with CB, CNT, nanoG as the only filler or combining CB with either CNT or nanoG. Structure of nanocomposites was investigated by means of TEM and X-ray diffraction (XRD) analysis. Dynamic storage modulus at low strain amplitude ($G'_{\gamma min}$) was determined through dynamic-mechanical measurements in the torsion mode. The experimental values were elaborated according to models available in literature. The results were analyzed in the light of findings from TEM and XRD analyses.

2. Experimental

2.1. Materials

Synthetic poly(1,4-*cis*-isoprene) (PI) was SKI3 from Nizhnekamskneftechim Export, with 70 Mooney Units (MU) as Mooney viscosity (M_L(1+4)100°C).

Table 1. Measured BET surface area and DBP absorption number for carbon fillers

Carbon filler	BET surface area [m^2/g]	DBP absorption number [mL/100 g][a]
CB	77.0	85.0
CNT	199.9	316.3
nanoG	330.3	162.4

[a]mL of absorbed DBP/100 grams of CB

Carbon Black N326 (CB) was from Cabot, with the following characterization data: 30 nm as mean diameter of spherical primary particles, nitrogen adsorption number of 77 m^2/g and DBP adsorption number of 85 mL/100 g.

Multiwall Carbon Nanotubes were Baytubes® C150 P from Bayer Material Science, with a chemical purity ≥95 as wt%, a length in the 1–10 μm range, a number of walls between 3 and 15 and outer and inner diameters of 10–16 nm and 4 nm respectively.

NanoGraphite (nanoG) was Synthetic Graphite 8427® from Asbury Graphite Mills Inc. In the technical data sheet, the carbon content and the surface area are reported to be at least 99 wt% and 330 m^2/g, respectively. Chemical composition determined from elemental analysis was, as wt%: carbon 99.5, hydrogen 0.4, nitrogen 0.1, oxygen 0.0.

To allow a direct comparison among the three fillers, BET surface areas and DBP absorption numbers were determined with ASTM D6556 and ASTM D2414 methods, respectively. Values are reported in Table 1.

2.2. Preparation of composites

Composites were prepared using a Brabender® type internal mixer, with 50 mL mixing room. Formulations of samples containing only one filler, either CB or CNT or nanoG, are in Table 2. The same filler volume fractions were used for all the fillers. Samples are labelled CNT, nanoG, CB, with reference to fillers, with a number indicating the filler content, expressed in parts per hundred polymer (php). Formulations of samples containing hybrid filler systems, CB-CNT or CB-nanoG, are in Table 2. They are labelled CB-CNT or CB-nanoG, with reference to the fillers, with a number indicating the CB content. CB and the nanofiller have the same volume fraction in the composite.

The following procedure was adopted for the preparation of all the samples: 50 g of PI were introduced in the Brabender type internal mixer and masticated at 90°C for 1 min with rotors rotating at 30 rpm. The filler was then added, mixing was performed for 4 min and the composite was then discharged at a temperature of about 100°C. The composite, so prepared, was left to reach room temperature and was fed again to the Brabender mixer kept at a temperature of about 50°C. Peroxide was added and the final composite was discharged after 2 minutes. Composites were finally further homogeneized by passing them 5 times through a two roll mill operating at 50°C, with the front roll rotating at 30 rpm and the back roll rotating at 38 rpm and 1 cm as the nip between the rolls.

2.3. Characterization

Crosslinking reaction was studied at 150°C with a Monsanto oscillating disc rheometer (MDR 2000) (Alpha Technologies, Swindon, UK), determining the minimum modulus M_L, the maximum modulus M_H, the modulus M_{final} at the end of the crosslinking reaction, the time t_{s1} required to have a torque equal to $M_L + 1$, the time t_{90} required to achieve 90% of the maximum modulus M_H (i.e. to achieve the optimum

Table 2. Formulations of composites with different fillers[a,b]

	CB-0	CB-2.5	CB-5	CB-10	CB-20	CB-30
CB	0	2.50	5.00	10.00	20.00	30.00
	CNT-0	**CNT-2.5**	**CNT-5**	**CNT-10**	**CNT-20**	**CNT-30**
CNT	0	2.50	5.00	10.00	20.00	30.00
	NanoG-0	**NanoG-3**	**NanoG-6**	**NanoG-11**	**NanoG-22**	**NanoG-33**
NanoG	0	2.78	5.56	11.11	22.22	33.33
	CB-0-CNT	**CB-1.25-CNT**	**CB-2.5-CNT**	**CB-5-CNT**	**CB-10-CNT**	**CB-15-CNT**
CB	0	1.25	2.50	5.00	10.00	15.00
CNT	0	1.25	2.50	5.00	10.00	15.00
	CB-0-NanoG	**CB-1.25-NanoG**	**CB-2.5-NanoG**	**CB-5-NanoG**	**CB-10-NanoG**	**CB-15-NanoG**
CB	0	1.25	2.50	5.00	10.00	15.00
NanoG	0	1.39	2.78	5.56	11.11	16.67

[a]Labels and amount of ingredients (expressed in php) are indicated

[b]Other ingredient: PI 100 php, DCUP 1.4 php

of crosslinking) and the so called reversion, i.e. the relative decrease of the modulus at the end of the crosslinking reaction: $(M_H - M_{final})/(M_H - M_L)\cdot 100$. TEM analysis was performed with a Zeiss EM 900 microscope applying an accelerating voltage of 80 kV. Ultrathin sections (about 50 nm thick) were obtained by using a Leica EM FCS cryoultramicrotome equipped with a diamond knife (sample temperature: –130°C).

Wide-angle X-ray diffraction (WAXD) patterns were taken with an automatic Bruker D8 Advance diffractometer, in reflection, with nickel filtered Cu-Kα radiation (1.5418 Å), at 35 kV and 40 mA. The intensities of reflections in WAXD patterns reported in this manuscript were not corrected for polarization and Lorentz factors, to allow a better visibility of the (00ℓ) peaks. d-spacings were calculated using Bragg's law. The $D_{hk\ell}$ correlation length of CNT and nanoG crystals was determined applying the Scherrer equation (Equation (1)):

$$D_{hk\ell} = \frac{K\lambda}{\beta_{hk\ell}\cos\theta_{hk\ell}} \quad (1)$$

where K is the Scherrer constant, λ is the wavelength of the irradiating beam (1.5419 Å, CuKα), $\beta_{hk\ell}$ is the width at half height, and $\theta_{hk\ell}$ is the diffraction angle. The introduction of a correction factor has to be used in case $\beta_{hk\ell}$ is lower than 1°.

Dynamic-mechanical measurements on crosslinked composites were performed with a Monsanto R.P.A. 2000 rheometer in the torsion mode. For each sample, a first strain sweep (0.1–25% shear strain amplitude) was performed at 50°C and 1 Hz, then the sample was kept in the instrument at the minimum strain amplitude (γ_{min} = 0.1%) for 10 min, to achieve fully equilibrated conditions. Finally, dynamic tests were performed at 50°C at increasing strain amplitude (0.1–25% shear strain amplitude) with a frequency of 1 Hz.

3. Results and discussion

3.1. Electron microscopic analysis

Composite structure was investigated by electron microscopy, analyzing samples with the highest filler contents.

Figure 1 shows representative images of composites with the highest content of each carbon allotrope: CNT-30 (Figure 1a), nanoG-33 (Figure 1b) and CB-30 (Figure 1c).

Micrograph in Figure 1a, taken at high magnification, shows an even distribution of isolated and entangled CNT tubes that create a continuous network throughout the PI matrix. As previously observed [19], the melt blending of CNT with the PI matrix leads to a remarkable shortening of the original CNT length, that is reported to be up to 10 μm by the supplier. In Figure 1b, agglomerates of nano-G are shown in nanoG-33 sample: they are not larger than 10 μm and most of them have submicrometric size, with a disordered structure of the graphitic layers. The presence of single graphite layers and stacks of few of them indicates a high level of delamination. Nanofiller particles appear to be evenly distributed, giving rise to almost continuous network. In Figure 1c, fine and sub-micrometric aggregates of CB appear to give rise to networks, though not continuous.

Figure 2 shows representative TEM micrographs of composites with the highest contents of the hybrid filler systems: CB-15-CNT (Figure 2a) and CB-15-nanoG (Figure 2b). A continuous hybrid CNT-CB network is clearly visible at high magnification in Figure 2a. CNTs lie very close to CB aggregates, thanks to the good interaction between the two carbon allotropes. The high aspect ratio of CNT tubes and their ability to wrap around CB aggregates appear to play a key role in creating the hybrid network.

Distribution and dispersion of nanoG appear to be improved by the presence of CB. In fact, in Figure 2b, nanoG agglomerates appear smaller than those present in TEM micrographs of Figure 1b, with a larger amount of single graphite layers or of stacks of few of them. However, no continuous hybrid filler network is observed even in the sample containing a total amount of filler above the percolation threshold of nanoG and close to the percolation threshold of CB. NanoG tends to remain stacked and, in most cases, appears preferentially adhered to the CB particles.

3.2. Mechanical characterization and data elaboration

The mechanical behavior of the crosslinked composites based on PI filled with only one carbon allotrope (either CB or CNT or nanoG; formulations are in Table 2) or with binary filler systems (formulations are in Table 2) was studied by means of dynamic-mechanical tests. For each composite, the

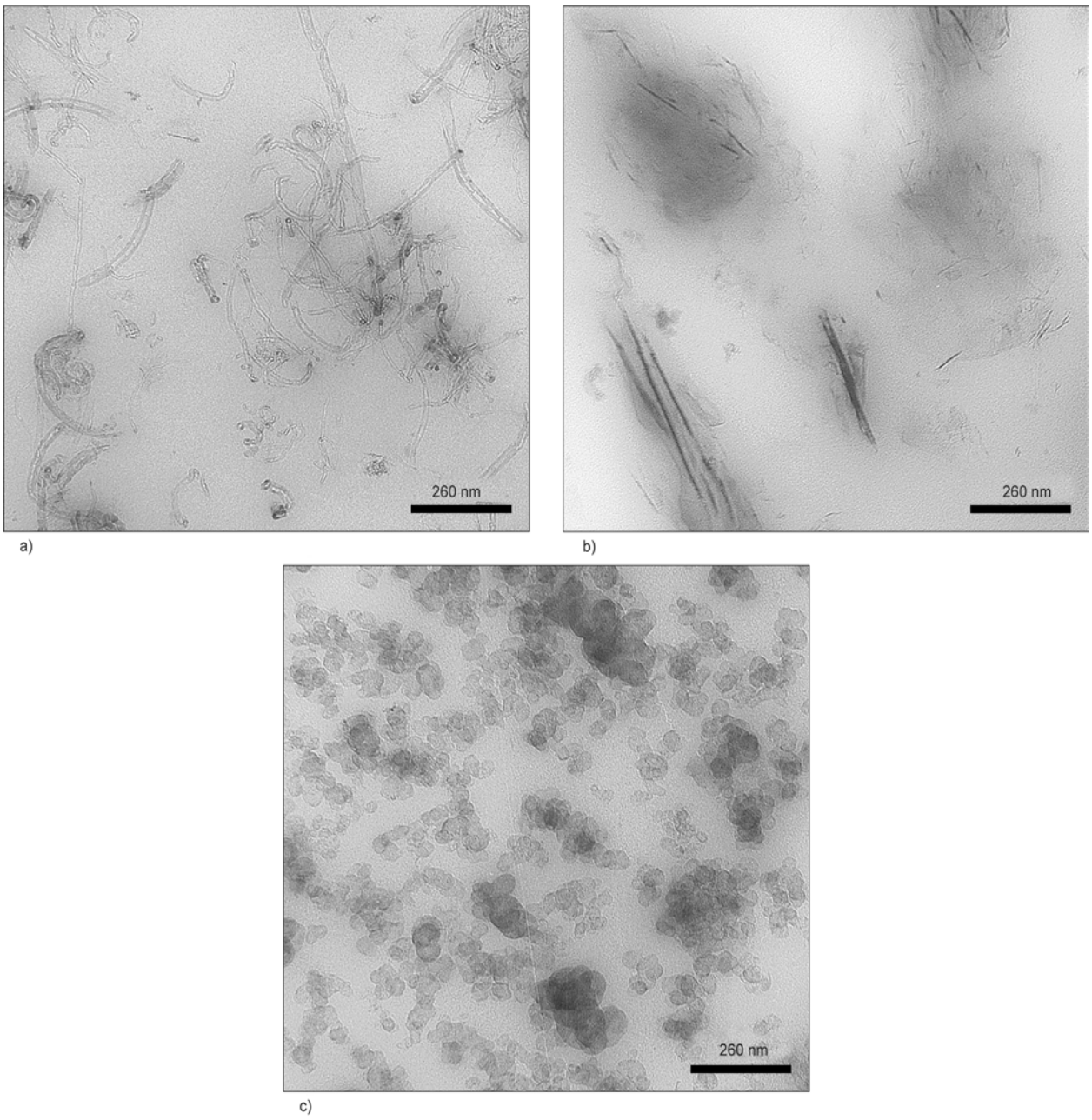

Figure 1. TEM micrographs of CNT-30 (a), nanoG-33 (b) and CB-30 (c)

storage shear modulus (G') was measured as a function of the strain, determining G' values up to 25% as strain amplitude.

Figure 3 shows an example of G' *vs* shear strain curves evaluated for composites with about 20 php as the overall filler content. Curves of CB filled PI and CNT filled PI are compared with the one of the composite with the hybrid CB-CNT system in Figure 3a and analogous comparison is shown in Figure 3b for composites with CB and nanoG.

The analysis of the reinforcement of single and binary filler systems was carried out on G' values taken at the minimum shear strain amplitude, $G'_{\gamma min}$. Figure 3 clearly highlights the higher reinforcing efficiency of CNT: G' for CNT-20 is nearly double that of nanoG-22, and G' values of both CNT-20 and nanoG-22 are higher than the G' value of CB-20. By replacing half of the nanofiller with the same amount of CB, $G'_{\gamma min}$ values are reduced and, for both nanofillers, storage moduli of the hybrid composites lie between the values of single filler composites. In Figure 4, $G'_{\gamma min}$ values are plotted as a function of the total filler volume fraction, i.e. $\Phi_{nanofiller} + \Phi_{CB}$, for all the investigated systems.

Figure 4 clearly shows the typical reinforcing effect of a filler in a molten polymer or in an elastomeric matrix. In fact, it is known that the modulus of the composite is remarkably increased when the added

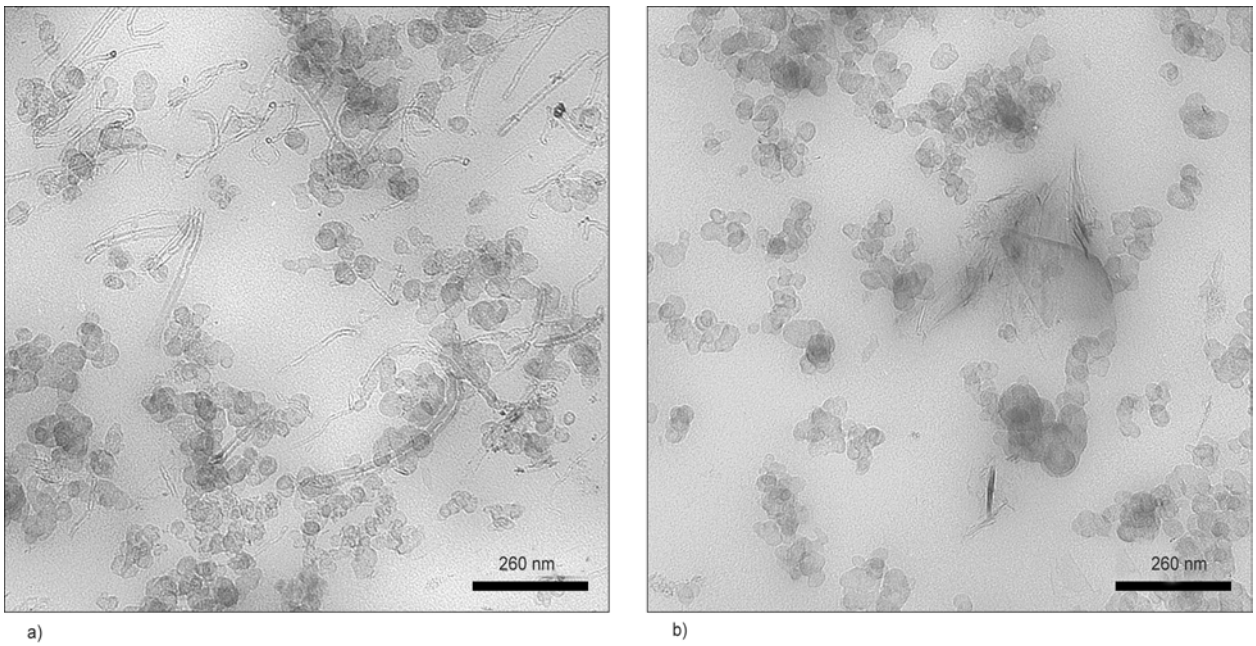

Figure 2. TEM micrographs of CB-15-CNT (a) and CB-15-nanoG (b)

filler(s) have a modulus much higher than that of the matrix. The effect of the reinforcing fillers becomes larger as the filler content increases. To describe such reinforcement, micromechanical models have been developed in the frame of continuum micro-mechanics approach [25–27]. These models attribute the composite reinforcement to the replacement of part of the soft matrix with the stiffer particles, and take into account the non-linear dependence of the modulus on the filler concentration as the result

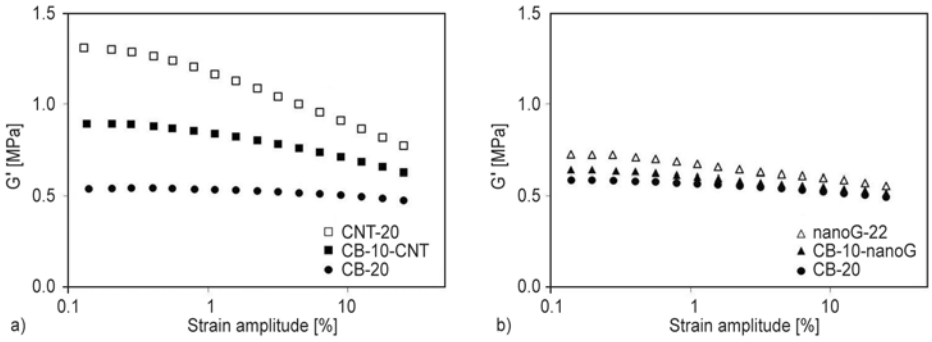

Figure 3. Storage shear modulus *G′ vs* strain amplitude for PI filled with 20 php of filler(s): CB and CNT as the fillers (a), CB and nanoG as the fillers (b)

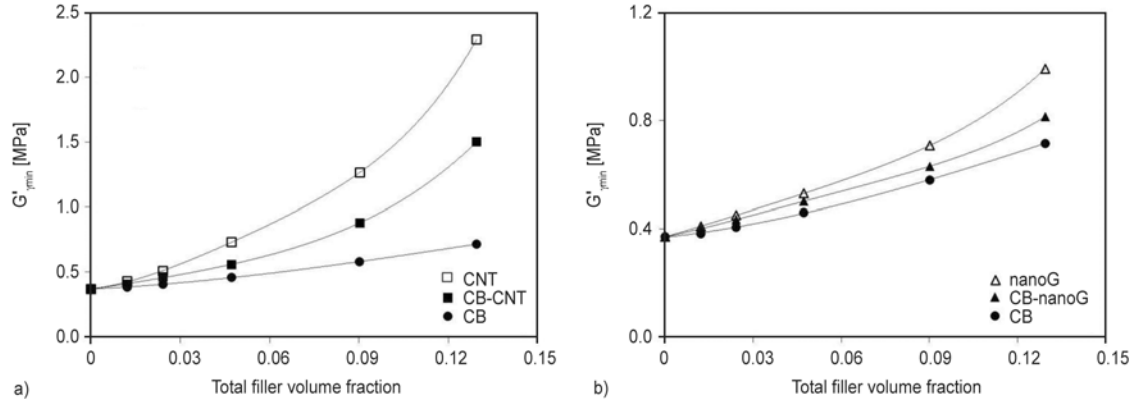

Figure 4. Experimental values of $G'_{\gamma min}$ *vs* total filler volume fraction (nanofiller:a) CNT, b) nanoG); lines indicate polynomial curves fitting the experimental data

of interactions of stress fields of each filler particle. The enhancement of the matrix elastic modulus, due to the filler addition, can be expressed for spherical filler particles through the Smallwood-Guth-Gold equation (Equation (2)) [28]:

$$\frac{G_c}{G_m} = 1 + 2.5\Phi + 14.1\Phi^2 \quad (2)$$

where G_c is the elastic modulus of the composite, G_m is the elastic modulus of the neat elastomer, Φ is the filler volume fraction and the quadratic term accounts for the mutual disturbance of filler particles. For non spherical particles and for particle aggregates, another equation proposed by Guth can be applied [29, 30] (Equation (3)):

$$\frac{G_c}{G_m} = 1 + 0.67f\Phi + 1.62f^2\Phi^2 \quad (3)$$

where f is a shape factor that takes into account the rod-like shape of filler or filler aggregate and is given by the length to width ratio of particle or aggregate. The authors relied on this model in previous studies on elastomer nanocomposites, to fit the mechanical properties of nanocomposites based on PI and containing either CNT [19] or nanoG [20] as the nanofiller. Best fit approach allowed determining the f aspect ratios, that were calculated to be 22 for CNT and 5 for nanoG. Equation (3) was applied also in other works in the literature for determining the aspect ratio f of CNT: f values in the range from 15 to 20 were reported [31] for composites based on a blend of a poly(1,3-butadiene) and poly[styrene-co-(1,3-butadiene)], prepared through dry melt blending. For composites based on poly[styrene-co-(1,3-butadiene)], prepared through solution blending, f values were in the range from 40 to 45 [4]. In this work, data available for the single filler composites allowed to calculate the f aspect ratio, reported in Table 3, by applying the best fit approach to the Guth equation (Equation (3)). The f aspect ratio appears to be substantially in line with the one published by some of the authors for nanoG [20], whereas is lower for CNT [19].

Figure 3 shows as well that G' decreases with strain amplitude when the composites contain a carbon nanofiller and this decrease is particularly pronounced for composites with CNT as the nanofiller. As mentioned in the Introduction, nanofillers are known to promote a remarkable Payne effect [12]. Several models have been developed in order to explain such an effect on the basis of two main interpretations: the first one, related to the filler networking concept, assumes an agglomeration–deagglomeration process of the filler network above the filler percolation threshold [12, 32–34], the second one, related to filler–matrix interaction, assumes matrix-filler bonding and debonding mechanisms [35–43]. It is not within the scope of this work to discuss the physical mechanisms occurring in the composites. Results will be thus analyzed from a mere phenomenological standpoint, moving from the phenomenon of filler percolation.

In previous author's works on elastomer nanocomposites, initial modulus values of matrix and composites were elaborated to calculate the mechanical percolation of the nanofillers, by means of the Huber-Vilgis plot [44]. The excess of modulus at minimum deformation $(G_c - G_m)/G_m$, was plotted as a function of the filler volume fraction in a double logarithmic plot. Usually, such plot shows two linear regimes with different slope, at filler contents below and above the percolation threshold, Φ_p. The percolation threshold is therefore evaluated as the filler content at which a discontinuity in the Huber-Vilgis plot is observed, and it was found to occur at 7.2 php for CNT [19] and at 21.2 php for nanoG [20]. For composites with only one carbon allotrope, Φ_p values were calculated on the basis of $G'_{\gamma min}$ values, by the Huber-Vilgis plot, and are shown in Table 3. Only the percolation threshold of CB could not be measured in the range of filler contents explored, since it is close to 30 php for N326. Determination of Φ_p for CB in PI based composites was performed by preparing samples with CB content higher than 30 php and Φ_p value was calculated to be 29 php, as shown in Table 3. With respect to previous works by the authors [19, 20], Φ_p value is in line for nanoG and is higher for CNT. This latter finding could be justified taking into account the lower CNT aspect ratio, that evidently depends on the mixing conditions experienced by the composite.

When dealing with binary filler systems, the applicability of Guth equation (Equation (3)) decays, and

Table 3. Filler f aspect ratio and percolation threshold, Φ_p, of CB, CNT and nanoG in PI matrix

Filler	f aspect ratio	Φ_p [php]
CB	5	29
CNT	12	9
nanoG	6	17

the prediction of the composite modulus by micromechanical models can be very complex. However, it is still possible to evaluate, rather simply, the extent of interaction between two different fillers, highlighting synergistic effects by means of an approach proposed by Sternstein *et al*. [45], who studied the influence of the mutual interaction of two different fillers on the mechanical reinforcement of an elastomeric matrix. They evaluated interactive effects of nanosilica particles (fumed and surface treated particles to form a binary system) in a poly(vinyl acetate) matrix by calculating the difference between the modulus values of the composite and those predicted by the following simple mixing rule:

$$G'_c(\Phi_a, \Phi_b) = G'_a(\Phi_a) + G'_b(\Phi_b) - G'_m \quad (4)$$

where $G'_c(\Phi_a, \Phi_b)$ is the modulus of a composite with two fillers indicated by *a* and *b*, with volume fractions Φ_a and Φ_b, respectively, index c stays for composite, G'_m, $G'_a(\Phi_a)$ and $G'_b(\Phi_b)$ are values of modulus of the neat polymer matrix *m*, of the composite with only filler *a* (volume fraction Φ_a) and of the composite with only filler *b* (volume fraction Φ_b), respectively. Values from this additive model establish a sort of lower benchmark of expected values and are obtained under the hypothesis that no interaction occurs between two different fillers. In Equation (4), the volume fraction of each filler in the composite with the binary filler system (e.g. Φ_a of G'_c) is the same as in the composite with only one filler (e.g. Φ_a of G'_a).
Equation (4) can be rearranged as Equation (5):

$$G'_c(\Phi_a, \Phi_b) = G'_m + (G'_a(\Phi_a) - G'_m) + (G'_b(\Phi_b) - G'_m) = G'_m + \Delta G'_a(\Phi_a) + \Delta G'_b(\Phi_b) \quad (5)$$

In this work, such model will be referred to as 'additive model', because the composite modulus is simply obtained as the sum of different contributions: the neat matrix modulus and the enhancements of modulus independently produced by each single filler in the same matrix at the same concentration as in the composite. Such model takes into account the nonlinear dependence of initial modulus on each single filler content, by G'_a and G'_b functions, but it does not include any nonlinearity due to the interactions between two different fillers at $\Phi_a+\Phi_b$ concentration. In the mentioned work [45], the measured values of initial moduli were found to be higher than the ones calculated with Equation (5). The differences between experimental and predicted values were attributed to an interaction term ($\Delta G'_{int}(\Phi_a, \Phi_b)$), that is specific of the binary filler/matrix system, that has to be added to Equation (5) as Equation (6):

$$G'_c(\Phi_{a,b}) = G'_m + \Delta G'_a(\Phi_a) + \Delta G'_b(\Phi_b) + \Delta G'_{int}(\Phi_a, \Phi_b) \quad (6)$$

Such an interaction term is in principle dependent on the fillers concentration (total and relative) as well as on the matrix and on the fillers features (surface area, filler aspect ratio and filler-matrix interaction strength).
Data of composites of the present work, containing only one filler, were examined by using Equation (6). A composite with only one filler can be ideally considered as a binary filler mixture composite, with two parts of the same filler. Evidently, the ratio between said two parts affects the results. In the following discussion, such ratio is fixed to 1:1. The total volume fraction $\Phi\varphi$ is thus split in two equal parts ($\Phi/2$). If the modulus of the single filler composite could be calculated by applying the additive model, the following equation (Equation (7)), analogous to Equation (5), should give the modulus values:

$$G'_c(\Phi) = G'_m + \Delta G'_c\left(\frac{\Phi}{2}\right) + \Delta G'_c\left(\frac{\Phi}{2}\right) = G'_m + 2\cdot\Delta G'_c\left(\frac{\Phi}{2}\right) \quad (7)$$

Figure 5 shows the $G'_{\gamma min}$ values of composites containing only one filler, as a function of the filler volume fraction. Symbols refer to experimental values and dotted lines indicate values obtained according to the additive model, through Equation (7).
The curves that interpolate the experimental values of the composites modulus (solid lines in Figure 5) diverge from the dotted lines that were drawn on the basis of the additive model, taking values from Equation (7). By examining the curves of Figure 5 in the light of data of Table 3, it appears that the differences between experimental and predicted values for CNT and nanoG become appreciable only when the nanofiller content is above the percolation threshold. In the case of CB, the percolation threshold (Φ_p close to 30 php) is only approached and

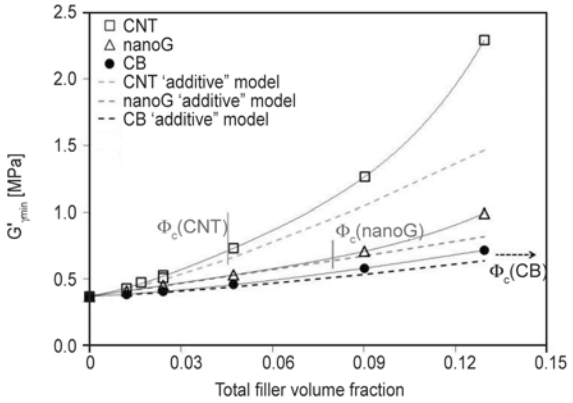

Figure 5. $G'_{\gamma min}$ *vs* filler volume fraction for CB, CNT and nanoG filled composites; broken lines indicate values predicted by the additive model (Equation (7)); the percolation threshold of each system (see Table 6) is also displayed

thus the interactive term is rather small. The excess of modulus could be seen as a sort of 'auto-interactive' term, that can be calculated by means of the following equation (Equation (8)), analogous to Equation (6):

$$G'_c(\Phi) = G'_m + \Delta G'_c\left(\frac{\Phi}{2}\right) + \Delta G'_c\left(\frac{\Phi}{2}\right) = G'_m + 2\cdot\Delta G'_c\left(\frac{\Phi}{2}\right) + \Delta G'_{int}\left(\frac{\Phi}{2},\frac{\Phi}{2}\right) \quad (8)$$

This 'auto-interactive' term is clearly related to the nonlinearity of the examined composite. In fact, if the modulus values of a composite with only one filler follow the Guth model (Equation (2)), by introducing the Guth expression (Equation (3)) for $G'_c(\Phi)$ and $G'_c(\Phi/2)$ into Equation (8), the following relationship is obtained (Equation (9)):

$$\Delta G'_{int}\left(\frac{\Phi}{2},\frac{\Phi}{2}\right) = \frac{1}{2}\cdot 1.62 f^2\Phi^2 \quad (9)$$

This equation indicates that the 'auto-interactive' term is related only to the quadratic (nonlinear) term of the dependence of modulus on the filler content. This so called 'auto-interactive' term $\Delta G'_{int}(\Phi/2, \Phi/2)$ was calculated through Equation (8) for all the composites containing only one filler. Moreover, the interactive term was calculated by applying Equation (6) for composites containing the hybrid filler systems. For this evaluation, experimental data were fitted by polynomial best fitting curves (lines in Figure 4), in order to compute the modulus values at the exact filler contents necessary to evaluate $\Delta G'_{int}$ by Equations (6) and (8).

Figure 6 shows the dependence of both the interactive and 'auto-interactive' terms on the total filler volume fraction. Graphs were prepared in order to emphasize the comparison between interactive terms arising from systems with only one filler or with the hybrid filler system.

Some comments can be added. Interactive terms for a given filler mixture (either made by two different fillers or by two parts of the same filler) strongly depend on the filler content, as expected: they are negligible at low contents, increase with the filler amount and appear to be remarkable only at the highest contents. It is definitely worth underlining the more pronounced nonlinearity of composites based on CNT with respect to composites based on nanoG and CB. Most interesting results seem to arise from the comparison of the composites with the hybrid filler systems CB-CNT and CB-nanoG. In fact, while

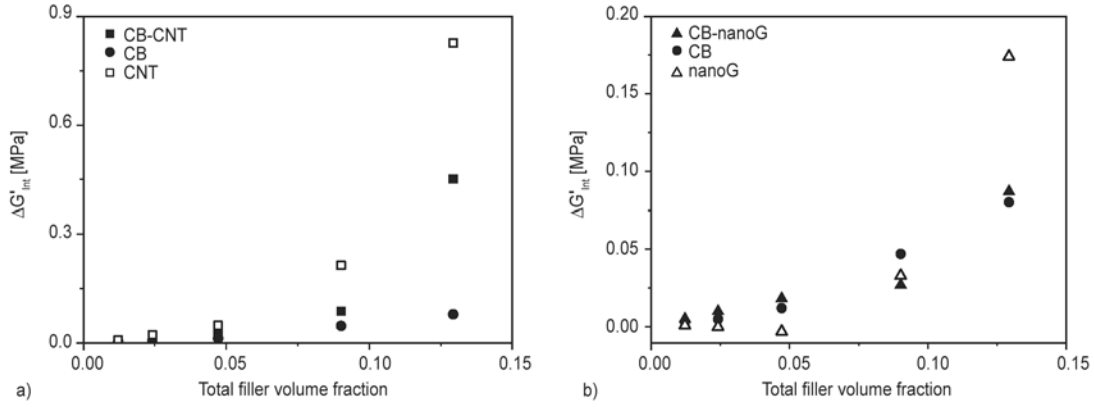

Figure 6. Interactive and 'auto-interactive terms', computed by Equation (6) and (8), respectively, as a function of the total filler volume fraction for the investigated systems; a) CB and/or CNT filled systems, b) CB and/or nanoG filled systems

values of $\Delta G'_{int}$ for the hybrid CB-CNT system (symbols ■ in Figure 6a) are between those of composites with either only CNT or only CB, values of $\Delta G'_{int}$ for the hybrid CB-nanoG system (symbols ▲ in Figure 6b) are overlapped with the values of the system containing only CB.

Modulus reinforcement is often evaluated as the ratio of the composite modulus over the matrix modulus. In a previous work by some of the authors, the reinforcement of PI filled with only CNT or filled with a mix of CNT and 60 php of CB [19] was evaluated. It was found that the relative increase of modulus brought about by CNT was the same, in the absence and in the presence of CB. $G'_{\gamma min}$ experimental data are in this work elaborated as done in ref. [19]. The relative modulus enhancement is expressed by a *k* factor, defined as follows: the moduli of composites with only CNT or only nanoG ($G'_{nanofiller}$) are normalized over the modulus of the neat PI matrix (G'_m) (Equation (10)):

$$k = \frac{G'_{nanofiller}(\Phi_{nanofiller})}{G'_m} \tag{10}$$

whereas the moduli of the hybrid filler composites (G'_c) are normalized over the modulus of the composite with only CB (G'_{CB}) (Equation (11)):

$$k = \frac{G'_c(\Phi_{nanofiller}, \Phi_{CB})}{G'_{CB}(\Phi_{CB})} \tag{11}$$

Figure 7 shows the *k* factor of the investigated composites, as a function of the nanofiller volume fraction. It is interesting to note that, in agreement with the results shown in ref. [19], in the investigated range of filler content, nanofillers enhance the matrix modulus by a multiplication factor, *k*, that depends only on the nanofiller type and content, no matter if

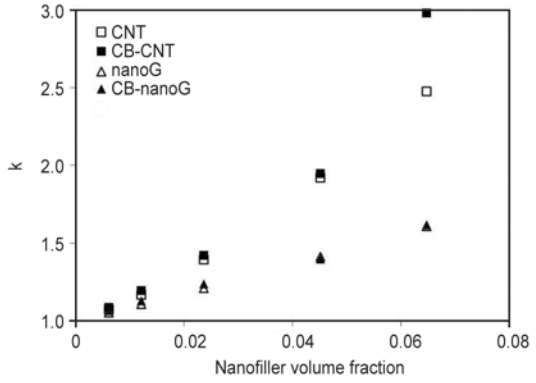

Figure 7. *k* factor vs nanofiller volume fraction; open symbols: single nanofiller compounds, full symbols: hybrid compounds (nanofiller-CB)

the matrix is a neat or a CB filled polymer. The only exception to this finding are the data of the systems with a CNT content of 6.5% (about 15 php), which deserve further investigation.

In a recent work [46], the multiplication factor *k* was calculated for CNT in PI based composites containing 12 php of CNT and 0, 20, 40, 60 php of CB and was found to be in a very narrow range. In particular, by keeping the same volume fraction of CNT in composites containing either 0 or 60 php of CB, *k* was observed to be 3.2 and 3.4, respectively.

On the basis of the observation that the multiplication factor, *k*, does not depend on the composition of the matrix (that can be either neat or filled with CB), the Equation (12) can be written:

$$k(\Phi_{nanofiller}) = \frac{G'_{nanofiller}(\Phi_{nanofiller})}{G'_m} = \frac{G'_c(\Phi_{nanofiller}, \Phi_{CB})}{G'_{CB}(\Phi_{CB})} \tag{12}$$

with $k(\Phi_{nanofiller})$ independent of Φ_{CB}.

By combining Equation (12) with Equation (6), this Equation (13) was derived:

$$k(\Phi_{nanofiller}) = 1 + \frac{\Delta G'_{int}(\Phi_{nanofiller}, \Phi_{CB})}{(G'_{CB}(\Phi_{CB}) - G'_m)} \tag{13}$$

Equation (13) shows that $k>1$ implies that $\Delta G'_{int}(\Phi_{nanofiller}, \Phi_{CB})$ is $\neq 0$, that means there is interaction between the nanofiller and CB, what was named above as synergy. As a matter of fact, Equation (12) itself reveals the interaction between the two different fillers. In fact, Equation (12) shows that the modulus of the composite G'_c with both fillers can be obtained by multiplying the moduli of composites containing only one filler, as shown by Equation (14):

$$G'_c(\Phi_{nanofiller}, \Phi_{CB}) = \frac{G'_{nanofiller}(\Phi_{nanofiller}) \cdot G'_{CB}(\Phi_{CB})}{G'_m} \tag{14}$$

These comments concerning *k* factor are based on the collected experimental data and a more general validity (for other filler systems) has still to be demonstrated.

Figure 1 clearly shows that *k* of CNT is higher than *k* of nanoG. The higher value of the *k* factor for CNT with respect to nanoG could be considered in line with what shown in the TEM micrographs: CNT does

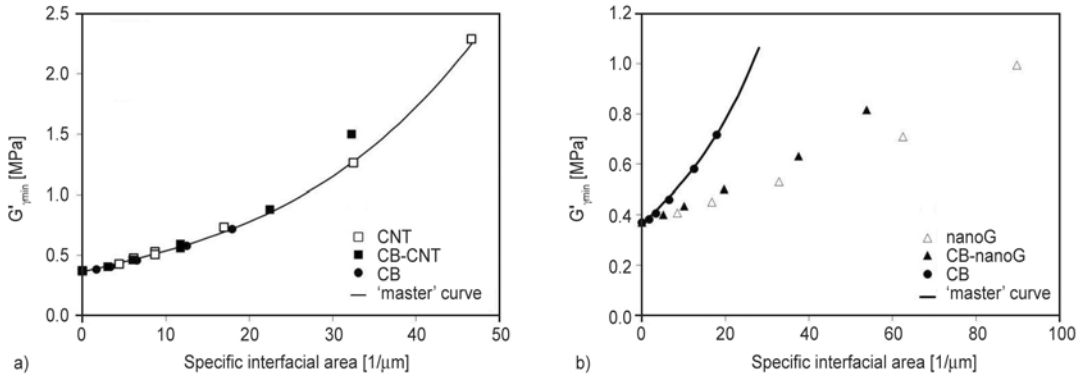

Figure 8. $G'_{\gamma min}$ values as a function of the specific filler – matrix interfacial area for the different compounds; the 'master' curve averaging the three fitting curves of the systems in a) is shown as well

have a higher ability to form networks, with itself and with a nano-structured filler such as CB. However, the high content of nanoG required to build networks is to an extent unexpected, on the basis of BET surface area data reported in Table 1.

It appears thus worthwhile to investigate the role played by surface area and, in particular, by filler-polymer interfacial area in determining the initial modulus of the composite material. Such investigation is more significant in the light of recent literature [34, 40], according to which the matrix properties do not keep constant with filler loading, rather they change depending on the amount of filler-matrix interface area (A_i). In particular, it was shown [40] that the reinforcement increases by changing particle shape at the same filler volume fraction i.e. by increasing surface area, for composites with the same chemical nature of the fillers.

In Figure 8, $G'_{\gamma min}$ data are plotted versus the specific filler – matrix interfacial area (the interfacial area normalized over the composite volume), evaluated as $A_i \cdot \rho \cdot \Phi$, where A_i is assumed to be equal to BET surface area (see Table 1) and ρ is the filler density. For hybrid filler systems, the specific filler – matrix interfacial area is evaluated for each filler at the corresponding volume fraction and the results are simply added to give the overall area. Figure 8a shows the experimental points for the composites containing only CNT, only CB and the hybrid CB-CNT system. Points referring to the three different composites appear to lie on a common 'master' curve (solid line in both Figure 8a and 8b), evaluated by averaging the three best fitting curves of each system.

This elaboration indicates that the filler surface and thus the filler-matrix interfacial area are the key features that affect the initial modulus values of the composites. This comment is simply in line with the basic theory of elastomer reinforcement [26, 27]. However for the first time, a common elaboration seems to be possible for nano- and nano-structured fillers. Figure 8b shows the 'master' curve evaluated by data of Figure 8a and experimental points for the composites containing only nanoG, only CB and the hybrid CB-nanoG systems. It is evident that points arising from nanoG based composites are well below the 'master' curve. To justify this finding, it could be hypothesized that the filler surface area of nanoG is not totally accessible to the polymer chains. In fact, Table 2 shows that, although the BET surface area of nanoG is higher than that of CNT, DBP absorption for nanoG is lower than for CNT. It is known [27] that the DBP absorption is correlated with the volume of the polymer occluded by the filler. Points in Figure 8b could be brought on the 'master' curve, by assuming for nanoG a surface area of about 90 m^2/g. It could be thus hypothesized that the surface areas experimentally determined for CB and CNT are prevailingly accessible to polymer chains, whereas nanoG layers seem to be accessible to the small Helium atoms used for the BET measurement but not to the bulky chains. This leads to hypothesize that nanoG layers are stacked, forming crystalline aggregates. To investigate the aggregation of layer in nanoG and in CNT, XRD analysis was performed on composites CB-15-nanoG and CB-15-CNT. Figure 9a shows the XRD pattern of the nanoG based composite and Figure 9b shows the XRD pattern of the CNT based composite. By applying the Scherrer equation (see Equation (1)) to the 002 reflection at 26.5° as 2θ value in the pattern of CB-15-nanoG, the number of layers stacked in a crys-

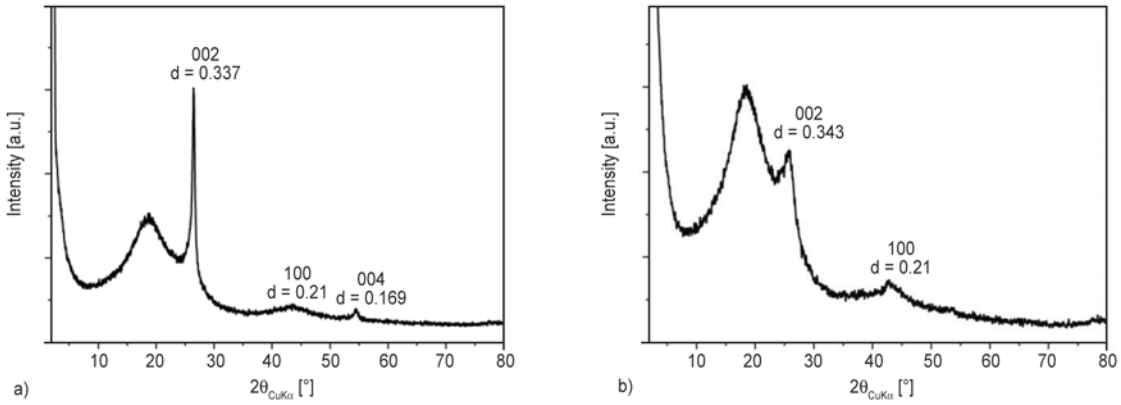

Figure 9. XRD pattern of CB-15-nanoG (a) and CB-15-CNT (b) in the 0–80° range as 2θ values

talline domain was calculated to be about 72. Interestingly, this number is higher than the one detected in the pristine nanoG sample [21].

It could be commented that the high pressure applied in the crosslinking step brings nanoG to a minimum of energy, that means to a higher crystallinity. This relatively high number of stacked layers confirms that the surface area measured through BET technique is not accessible to the polymer chains and justifies what shown in Figure 8b. By applying the Scherrer equation, the number of layers wrapped to form CNT was calculated to be about 12. Interestingly, also this number is higher than the one found in the pristine sample (10). Also in this case, the crosslinking pressure can be invoked to justify the formation of crystalline domains with a higher correlation length.

4. Conclusions

This work is focused on the interactive effects of carbon allotropes on the mechanical reinforcement of a hydrocarbon polymer matrix, poly(1,4-cis-isoprene). So called nano-fillers such as CNT or nano-G are used, in the neat polymer matrix, or combined with a nano-structured filler such as CB.

The reinforcement effects on the shear storage modulus brought about by hybrid fillers in an elastomeric matrix are analysed by a method proposed by Sternstein [45] and quantified by an interaction term. This method relates the extent of filler particles interactions to the nonlinearity of filler reinforcement and allows to assess the ability of the nanofiller to impart such non linearity to the composite with the hybrid filler system thus giving a reliable indication of the filler(s) ability to build networks.

CNT were found to have the largest values of the interaction term and to form filler networks, also in presence of CB, at low CNT concentrations.

A sort of fingerprint is identified for the carbon nanofillers. In fact, the relative increase of modulus, defined as k factor, brought about by a given nanofiller in the pure matrix is the same as in the system with CB. A correlation between the interaction term and k factor is shown.

Finally, the filler-polymer interfacial area is shown to be able to correlate the behaviour of a nano- with a nanostructured filler (CNT with CB): experimental storage modulus values lie on the same 'master' curve when plotted versus the specific interfacial area, provided that the surface area is accessible to the polymer. The definition of such a 'master' curve could be seen as a tool to investigate the polymer-filler interfacial area actually available. Moreover, these findings seem to highlight the importance of CNT shape, that allows high values of accessible surface area and the easy formation of networks.

References

[1] Mittal V.: Advances in polyolefin nanocomposites. CRC Press, Boca Raton (2011).

[2] Maiti M., Bhattacharya M., Bhowmick A. K.: Elastomer nanocomposites. Rubber Chemistry and Technology, **81**, 384–469 (2008). DOI: 10.5254/1.3548215

[3] Moniruzzaman M., Winey K. L.: Polymer nanocomposites containing carbon nanotubes. Macromolecules, **39**, 5194–5205 (2006). DOI: 10.1021/ma060733p

[4] Bokobza L.: Multiwall carbon nanotube elastomeric composites: A review. Polymer, **48**, 4907–4920 (2007). DOI: 10.1016/j.polymer.2007.06.046

[5] Novoselov K. S., Geim A. K., Morozov S. V., Jiang D., Zhang Y., Dubonos S. V., Grigorieva I. V., Firsov A. A.: Electric field effect in atomically thin carbon films. Science, **306**, 666–669 (2004).
DOI: 10.1126/science.1102896

[6] Park S., Ruoff R. S.: Chemical methods for the production of graphenes. Nature Nanotechnology, **4**, 217–224 (2009).
DOI: 10.1038/nnano.2009.58

[7] Jang B. Z., Zhamu A.: Processing of nanographene platelets (NGPs) and NGP nanocomposites: A review. Journal of Materials Science, **43**, 5092–5101 (2008).
DOI: 10.1007/s10853-008-2755-2

[8] Ramanathan T., Stankovich S., Dikin D. A., Liu H., Shen H., Nguyen S. T., Brinson L. C.: Graphitic nanofillers in PMMA nanocomposites – An investigation of particle size and dispersion and their influence on nanocomposite properties. Journal of Polymer Science Part B: Polymer Physics, **45**, 2097–2112 (2007).
DOI: 10.1002/polb.21187

[9] Li B., Zhong W-H.: Review on polymer/graphite nanoplatelet nanocomposites. Journal of Materials Science, **46**, 5595–5614 (2011).
DOI: 10.1007/s10853-011-5572-y

[10] Potts J. R., Dreyer D. R., Bielawski C. W., Ruoff R. S.: Graphene-based polymer nanocomposites. Polymer, **52**, 5–25 (2011).
DOI: 10.1016/j.polymer.2010.11.042

[11] Sengupta R., Bhattacharya M., Bandyopadhyay S., Bhowmick A. K.: A review on the mechanical and electrical properties of graphite and modified graphite reinforced polymer composites. Progress in Polymer Science, **36**, 638–670 (2011).
DOI: 10.1016/j.progpolymsci.2010.11.003

[12] Payne A. R., Whittaker R. E.: Low strain dynamic properties of filled rubbers. Rubber Chemistry and Technology, **44**, 440–478 (1971).
DOI: 10.5254/1.3547375

[13] Bokobza L., Rahmani M., Belin C., Bruneel J-L., El Bounia N-E.: Blends of carbon blacks and multiwall carbon nanotubes as reinforcing fillers for hydrocarbon rubbers. Journal of Polymer Science Part B: Polymer Physics, **46**, 1939–1951 (2008).
DOI: 10.1002/polb.21529

[14] Bokobza L.: Mechanical, electrical and spectroscopic investigations of carbon nanotube-reinforced elastomers. Vibrational Spectroscopy, **51**, 52–59 (2009).
DOI: 10.1016/j.vibspec.2008.10.001

[15] Lorenz H., Fritzsche J., Das A., Stöeckelhuber K. W., Jurk R., Heinrich G., Klüppel M.: Advanced elastomer nano-composites based on CNT-hybrid filler systems. Composites Science and Technology, **69**, 2135–2143 (2009).
DOI: 10.1016/j.compscitech.2009.05.014

[16] Ryu S-R., Sung J-W., Lee D-J.: Strain-induced crystallization and mechanical properties of NBR composites with carbon nanotube and carbon black. Rubber Chemistry and Technology, **85**, 207–218 (2012).
DOI: 10.5254/rct.12.88955

[17] Wang L. L., Zhang L. Q., Tian M.: Mechanical and tribological properties of acrylonitrile–butadiene rubber filled with graphite and carbon black. Materials and Design, **39**, 450–457 (2012).
DOI: 10.1016/j.matdes.2012.02.051

[18] Malas A., Das C. K., Das A., Heinrich G.: Development of expanded graphite filled natural rubber vulcanizates in presence and absence of carbon black: Mechanical, thermal and morphological properties. Materials and Design, **39**, 410–417 (2012).
DOI: 10.1016/j.matdes.2012.03.007

[19] Galimberti M., Coombs M., Riccio P., Riccò T., Passera S., Pandini S., Conzatti L., Ravasio A., Tritto I.: The role of CNTs in promoting hybrid filler networking and synergism with carbon black in the mechanical behavior of filled polyisoprene. Macromolecular Materials and Engineering, **298**, 241–251 (2012).
DOI: 10.1002/mame.201200075

[20] Galimberti M., Kumar V., Coombs M., Cipolletti V., Agnelli S., Pandini S., Conzatti L.: Filler networking of a nanographite with a high shape anisotropy and synergism with carbon black in poly(1,4-*cis*-isoprene)–based nanocomposites. Rubber Chemistry and Technology, in press (2014).
DOI: 10.5254/rct.13.87903

[21] Mauro M., Cipolletti V., Galimberti M., Longo P., Guerra G.: Chemically reduced graphite oxide with improved shape anisotropy. The Journal of Chemical Physics: C, **116**, 24809–24813 (2012).
DOI: 10.1021/jp307112k

[22] Bhattacharya M., Bhowmick A. K.: Synergy in carbon black-filled natural rubber nanocomposites. Part I: Mechanical, dynamic mechanical properties, and morphology. Journal of Materials Science, **45**, 6126–6138 (2010).
DOI: 10.1007/s10853-010-4699-6

[23] Brochard-Wyart F., de Gennes P. G.: Viscosity at small scales in polymer melts. European Physical Journal E, **1**, 93–97 (2000).
DOI: 10.1007/s101890050011

[24] Flores F., Graebling D., Allal A., Guerret-Piécourt C.: Modelization of flow electrification in a polymer melt. Journal of Physics D: Applied Physics, **40**, 2911–2919 (2007).
DOI: 10.1088/0022-3727/40/9/037

[25] Payne A. R.: Dynamic properties of filler-loaded rubbers. in 'Reinforcement of elastomers' (ed.: Kraus G.) Interscience Publishers, New York, 69–114 (1965).

[26] Donnet J. B., Custodero E.: Reinforcement of elastomers by particulate fillers. in 'The science and technology of rubber' (eds.: Mark J. E., Erman B., Eirich F. R.) Academic Press, San Diego, 367–400 (2005). DOI: 10.1016/B978-012464786-2/50011-0

[27] Medalia A. I.: Effect of carbon black on dynamic properties of rubber vulcanizates. Rubber Chemistry and Technology, **51**, 437–523 (1978). DOI: 10.5254/1.3535748

[28] Guth E., Gold O.: On the hydrodynamic theory of the viscosity of suspensions. Physical Review, **53**, 322–328 (1938).

[29] Guth E.: Theory of filler reinforcement. Journal of Applied Physics, **16**, 20–25 (1945). DOI: 10.1063/1.1707495

[30] Guth E.: Theory of filler reinforcement. Rubber Chemistry and Technology, **18**, 596–604 (1945). DOI: 10.5254/1.3546754

[31] Das A., Stöckelhuber K. W., Jurk R., Saphiannikova M., Fritzsche J., Lorenz H., Klüppel M., Heinrich G.: Modified and unmodified multiwalled carbon nanotubes in high performance solution-styrene–butadiene and butadiene rubber blends. Polymer, **49**, 5276–5283 (2008). DOI: 10.1016/j.polymer.2008.09.031

[32] Robertson C. G., Roland C. M.: Glass transition and interfacial segmental dynamics in polymer-particle composites. Rubber Chemistry and Technology, **81**, 506–522 (2008). DOI: 10.5254/1.3548217

[33] Bohm G. A., Tomaszewski W., Cole W., Hogan T.: Furthering the understanding of the non linear response of filler reinforced elastomers. Polymer, **51**, 2057–2068 (2010). DOI: 10.1016/j.polymer.2010.01.047

[34] Heinrich G., Klüppel M.: Recent advances in the theory of filler networking in elastomers. Advances in Polymer Science, **160**, 1–44 (2002). DOI: 10.1007/3-540-45362-8_1

[35] Maier P. G., Goritz D.: Molecular interpretation of the Payne effect. Kautschuk Gummi Kunstoffe, **49**, 18–21 (1996).

[36] Chazeau L., Brown J. D., Yanyo L. C., Sternstein S. S.: Modulus recovery kinetics and other insights into the payne effect for filled elastomers. Polymer Composites, **21**, 202–222 (2000). DOI: 10.1002/pc.10178

[37] Sternstein S. S., Zhu A-J.: Reinforcement mechanism of nanofilled polymer melts as elucidated by nonlinear viscoelastic behavior. Macromolecules, **35**, 7262–7273 (2002). DOI: 10.1021/ma020482u

[38] Montes H., Lequeux F., Berriot J.: Influence of the glass transition temperature gradient on the nonlinear viscoelastic behavior in reinforced elastomers. Macromolecules, **36**, 8107–8118 (2003). DOI: 10.1021/ma0344590

[39] Zhu Z., Thompson T., Wang S-Q., von Meerwall E. D., Halasa A.: Investigating linear and nonlinear viscoelastic behavior using model silica-particle-filled polybutadiene. Macromolecules, **38**, 8816–8824 (2005). DOI: 10.1021/ma050922s

[40] Kalfus J., Jancar J.: Elastic response of nanocomposite poly(vinylacetate)-hydroxyapatite with varying particle shape. Polymer Composites, **28**, 365–371 (2007). DOI: 10.1002/pc.20273

[41] Jancar J., Douglas J. F., Starr F. W., Kumar S. K., Cassagnau P., Lesser A. J., Sternsteinh S. S., Buehler M. J.: Current issues in research on structure–property relationships in polymer nanocomposites. Polymer, **51**, 3321–3343 (2010). DOI: 10.1016/j.polymer.2010.04.074

[42] Funt J. M.: Dynamic testing and reinforcement of rubber. Rubber Chemistry and Technology, **61**, 842–865 (1988). DOI: 10.5254/1.3536222

[43] Gauthier C., Reynaud E., Vassoille R., Ladouce-Stelandre L.: Analysis of the non-linear viscoelastic behaviour of silica filled styrene butadiene rubber. Polymer, **45**, 2761–2771 (2004). DOI: 10.1016/j.polymer.2003.12.081

[44] Huber G., Vilgis T. A.: Universal properties of filled rubbers: Mechanisms for reinforcement on different length scales. Kautschuk Gummi Kunstoffe, **52**, 102–107 (1999).

[45] Sternstein S. S., Ramorino G., Jang B., Zhu A-J.: Reinforcement and nonlinear viscoelasticity of polymer melts containing mixtures of nanofillers. Rubber Chemistry and Technology, **78**, 258–270 (2005). DOI: 10.5254/1.3547882

[46] Galimberti M., Coombs M., Cipolletti V., Riccò T., Agnelli S., Pandini S.: The role of nanofillers in promoting hybrid filler networking and synergism with carbon black in a hydrocarbon rubber. Kautschuk Gummi Kunstoffe, **7–8**, 31–36 (2013).

eXPRESS Polymer Letters Vol.8, No.6 (2014) 450–457
Available online at www.expresspolymlett.com
DOI: 10.3144/expresspolymlett.2014.48

A novel reduced graphene oxide decorated with halloysite nanotubes (HNTs-*d*-rGO) hybrid composite and its flame-retardant application for polyamide 6

*L. L. Li, S. H. Chen, W. J. Ma, Y. H. Cheng, Y. P. Tao, T. Z. Wu, W. P. Chen, Z. Zhou, M. F. Zhu**

State Key Laboratory for Modification of Chemical Fiber and Polymer Materials, College of Materials Science and Engineering, Donghua University, Shanghai 201620, People's Republic of China

Received 10 December 2013; accepted in revised form 24 February 2014

Abstract. The improvement of flame-retardant properties of polyamide 6 (PA6) was achieved by using reduced graphene oxide decorated with halloysite nanotubes (HNTs-*d*-rGO) hybrid composite as the additive in PA6 matrix. The intimate integration of reduced graphene oxide (rGO) and halloysite nanotubes (HNTs) through a three-step chemical functionalization, enabled the combination of their unique physical and chemical characteristics together. The nanostructure of HNTs-*d*-rGO was determined by Fourier transform infrared spectroscopy (FTIR), X-ray photoelectron spectroscopy (XPS) and transmission electron microscopy (TEM). A morphological study revealed that HNTs-*d*-rGO was dispersed uniformly in PA6 matrix. From the results of cone calorimetry measurements, the fire retardant properties of PA6 were further improved with the addition of HNTs-*d*-rGO when compared with that of either HNTs, or GO, or a mixture of HNTs and GO (HNTs-*m*-GO) used in PA6 matrix. The results indicate clearly that higher flame-retardant activity of the integrated HNTs-*d*-rGO nanostructures than that of the simple mixture verifies the importance of the intimate integration between HNTs and rGO, which ascribe to the combination of the stable silica layer created by HNT and the barrier effect of rGO.

Keywords: *nanocomposites, graphene oxide, halloysite nanotubes (HNTs), polyamide 6*

1. Introduction

Polyamide 6 (PA6), a commercially important semi-crystalline polymer, is widely used in engineering plastics, film and fibers [1–4], which usually causes fires and consequently leads to huge loss of human lives and property, which, to a certain degree, limits the range of applications. We demonstrate a novel strategy to improve the flame-retardant properties of PA6 by using reduced graphene oxide decorated with halloysite nanotubes (HNTs-*d*-rGO) hybrid composite.

Graphene, exhibiting outstanding electronic, mechanical [5–8] and thermal [9, 10] properties, is emerging as a rising star in the field of flame-retardant applications due to its endothermic and stable structure [10–13]. For example, the peak heat release rate (PHRR) of polyvinyl alcohol (PVA) filled with graphene is reduced by 49% [11]. However, in order to achieve fire resistance, the content of graphene used as flame retardant in polymer should be relatively high. Besides, nanocomposites consisting of polymer and clay, such as montmorillonite and kaolinite, are widely used to improve the flame-retardant properties of polymers [14, 15]. Halloysite nanotubes (HNTs), one kind of nanoclay, have attracted research attention as fillers for polymer nanocomposites due to their improvement of mechanical [16, 17], thermal [18], crystallization [19, 20] properties of polymer. Moreover, recent studies showed that HNTs enable to enhance the fire-retar-

*Corresponding author, e-mail: zhumf@dhu.edu.cn

dant performance of polymer composite, which is attributed to the formation of thermal insulation barrier during fire [21]. Therefore, the combination of reduced graphene oxide (rGO) and HNTs as additive may be considered as an efficient method to get good fire retardant properties in polymer.

Herein, we demonstrate a novel strategy to functionalize and decorate rGO with HNTs through a three-step chemical reaction. Finally, rGO decorated with HNTs (HNTs-*d*-rGO) was prepared and incorporated into PA6 for fire retardant applications.

2. Experimental

2.1. Materials

Graphite F-000 (≤2 μm) was purchased from Shanghai Yifan graphite Co., Ltd. (Shanghai, China). Polyamide 6 shows a melt flow rate (MFR) of 23.89 g/10 min provided by Jiangsu Haiyang Chemical Fiber Co., Ltd. (China). Halloysite nanotubes (HNTs) was supplied by Jinyangguang Ceramics Co. Ltd. (Zhengzhou, China). Sulphuric acid (H_2SO_4, 98%), hydrogen peroxide solution (H_2O_2, 30%), hydrochloric acid (HCl, 37%), potassium permanganate ($KMnO_4$), dimethylformamide (DMF), thionyl chloride ($SOCl_2$), triethylamine (Et_3N), toluene (C_7H_8), ethanol (C_2H_5OH), 3-aminopropyl triethoxysilane (APTES) and trichloroacetic acid ($C_2HCl_3O_2$) were used as received from Sinopharm Chemical Reagent Co., Ltd.

2.2. Synthesis of HNTs-decorated rGO (HNTs-*d*-rGO)

The synthetic routes of acylated rGO (rGO-COCl), ammoniated HNTs (HNTs-NH_2), HNTs-*d*-rGO are as shown in Figure 1. HNTs-NH_2 was synthesized according to the literature [22, 23]. Firstly, 20 mL APTES was dissolved in 250 mL of toluene, and then 6 g of dried HNTs was added into the above solution. The suspension was dispersed ultrasonically for 30 min at room temperature followed by stirring at 75°C for 20 h. The resulting powder was filtered and washed with toluene to remove the excess APTES, and then dried at 120°C under vacuum. Graphite oxide (600 mg) prepared using modified Hummers method [24, 25], was dispersed in $SOCl_2$ (120 mL) with addition of a few drops of DMF (3 mL), and the mixture was refluxed at 70°C for 24 h. After evaporation of the excess $SOCl_2$ under reduced pressure, the rGO-COCl product was added into an intensely stirred solution of 200 mL DMF and 10 mL triethylamine (Et_3N) at 120°C for 36 h. After cooling down to the room temperature, the products of HNTs-*d*-rGO were filtered through a PTFE membrane (0.22 μm), and washed with DMF and ethanol for three cycles respectively. Finally, the resulted HNTs-*d*-rGO was dried in vacuum at 120°C for 12 h.

2.3. Preparation of the PA6/ HNTs-*d*-rGO nanocomposites

All samples were dried in vacuum at 120°C for 24 h before use. Then the required proportion of HNTs-*d*-rGO were mixed and melt blended with PA6 in ThermoHaake Rheomix with the temperature range of 225–250°C at screw speed of 80 rpm. For comparison, PA6/HNTs, PA6/GO and PA6/mixture of HNTs and GO (HNTs-*m*-GO) were similarly prepared as mentioned for PA6/HNTs-*d*-rGO with equivalent filler content.

2.4. Characterization

Fourier-transform infrared (FTIR) spectra were recorded on a Nicolet 8700 FTIR spectrometer. The sample was mixed with potassium bromide (KBr) powder and pressed into pellets. Transmission electron microscopy (TEM) analysis was conducted using a JEOL JEM-2100 instrument with an acceleration voltage of 100 kV. The HNTs, GO and HNTs-*d*-rGO were dropped on a copper grid for TEM characterization. X-ray photoelectron spectroscopy (XPS) was performed with a VG ESCALB MK-II electron spectrometer. The excitation source was an

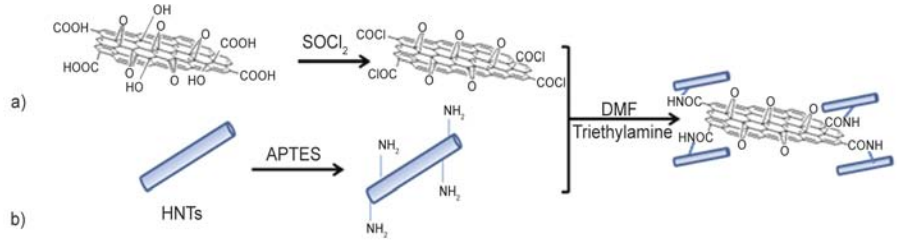

Figure 1. Schematic illustration of the synthetic route of HNTs-*d*-rGO

Al Kα line at 1253.6 eV. Scanning electron microscopic (SEM) images of the fracture surface of composites were collected using a Hitachi S-4800 field-emission SEM instrument (operated at 10 kV). The PA6 nanocomposite pellets were oven-dried and molded into standard 100×100×3 mm^3 samples using a Dehong SZ-5-C injection molding machine with the barrel and mold temperatures maintained at 270 and 50°C, respectively. Then cone calorimeter tests (ISO 5660) were performed on samples placed horizontally with a flux of 35 kW/m^2 to evaluate the flammability of the composites.

3. Results and discussion

3.1. Characterization of HNTs-*d*-rGO nanostructure

FTIR spectra of HNTs, HNT-NH_2, GO and HNTs-*d*-rGO are presented in Figure 2. Compared with the pristine HNTs (Figure 2 curve a), HNT-NH_2 exhibit some new FTIR peaks (Figure 2 curve b), such as the stretching vibration band of CH_2 around 2930 cm^{-1}, the deformation vibration CH_2 at 1492 cm^{-1}, and the deformation vibration NH_2 at 1560 cm^{-1}. All of these show that the successful grafting of amino groups to the surface of HNT. As shown in Figure 2 curve c, the absorption bands of GO at 1719, 1618 and 1055 cm^{-1} are ascribed to C=O, C=C and C–O [26, 27], respectively. After the functionalization of GO by HNT-NH_2, there are some new absorption peaks in the spectrum of HNTs-*d*-rGO. The strong absorption band at around 1090 cm^{-1} is attributed to the Si–O–Si group in APTES-modified sample HNT-NH_2, and the peak at 1568 cm^{-1} is corresponding to the bending vibrations of the amide groups, which together with the

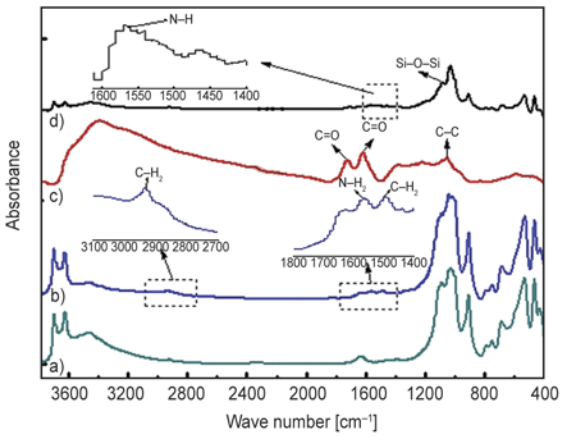

Figure 2. FTIR spectra of (a) pristine HNTs, (b) HNT-NH_2, (c) GO and (d) HNTs-*d*-rGO

significantly reduced intensity of hydroxyl stretching at 3400 cm^{-1} implying fewer oxygen-containing groups in the reduced GO are certifications of the successful decoration of HNT-NH_2 onto the surface of rGO.

The XPS spectra of pristine HNTs, HNT-NH_2, GO and HNTs-*d*-rGO, and higher resolution C1s spectra of GO, HNTs-*d*-rGO and N1s spectra of HNTs-*d*-rGO are shown in Figure 3. As can be observed, HNT-NH_2 displayed a strong photoemission at a binding energy (BE) of 401.9 eV belonging to N1s. The concentration of nitrogen increased up to 4.33% and the BE of 401.9 eV assigned to C–N–H, which implied the successful ammonification of HNTs. The main Si2p peak at 103 eV is attributed to Si–O–Si/Si–O–Al [23, 28]. The C1s XPS of GO (Figure 3b) shows a degree of oxidation with four peaks appearing at 284.8, 285.6, 286.8 and 288.4 eV, which are ascribed to the non-oxygenated ring C, the C bonded to C atoms in defective structures, the C in C–O bonds and the carbonyl C, respectively [29]. The C1s XPS spectrum of HNTs-*d*-rGO (Figure 3c) also exhibits these same oxygen functionalities, but the peak intensities of oxygenated C are much smaller than those in GO, indicating the partial reduction of GO. In the N1s spectra of HNTs-*d*-rGO (Figure 3d), The detection of a N1s peak at a binding energy of 400.6 eV, which is ascribed to C–N–C, is a key indication of the successful covalent functionlization of rGO by HNTs.

On the basis of FTIR and XPS results, TEM was employed to obtain the morphological information of products we have synthesized. As shown in Figure 4, compared with pristine HNTs (Figure 4a), HNT-NH_2, which was prepared by amino-functionalized HNT using APTES, not only did the diameter of the HNT increase to some degree, but also their surfaces (including outer surface and inner surface) were much rougher relative to HNT, and a thin polymeric layer could be observed (Figure 4b). The layers of GO (Figure 4c) are clean and several hundred nanometers large, while HNTs-*d*-rGO (Figure 4d) have many nanotubes attached. The rGO in HNTs-*d*-rGO was so thin that some of the edges are nearly invisible (Figure 4d). Moreover, the ordered graphite lattices are clearly visible and the disordered regions are also found in Figure 4e, indicating that the GO sheets were partially reduced and restored to ordered crystal structure. The inset selected area electron diffraction pattern (SAED),

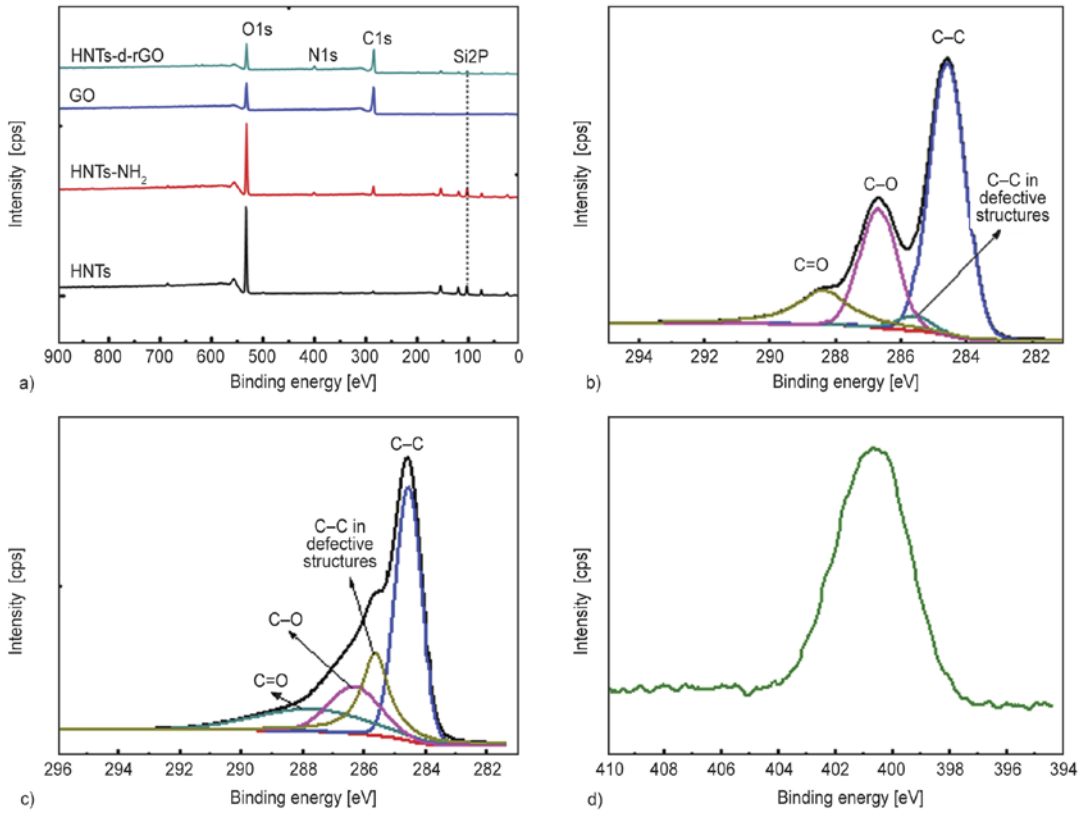

Figure 3. XPS spectra of (a) pristine HNTs, HNT-NH_2, GO and HNTs-*d*-rGO, and higher resolution C1s spectra of (b) GO, (c) HNTs-*d*-rGO and (d) N1s spectra of HNTs-*d*-rGO

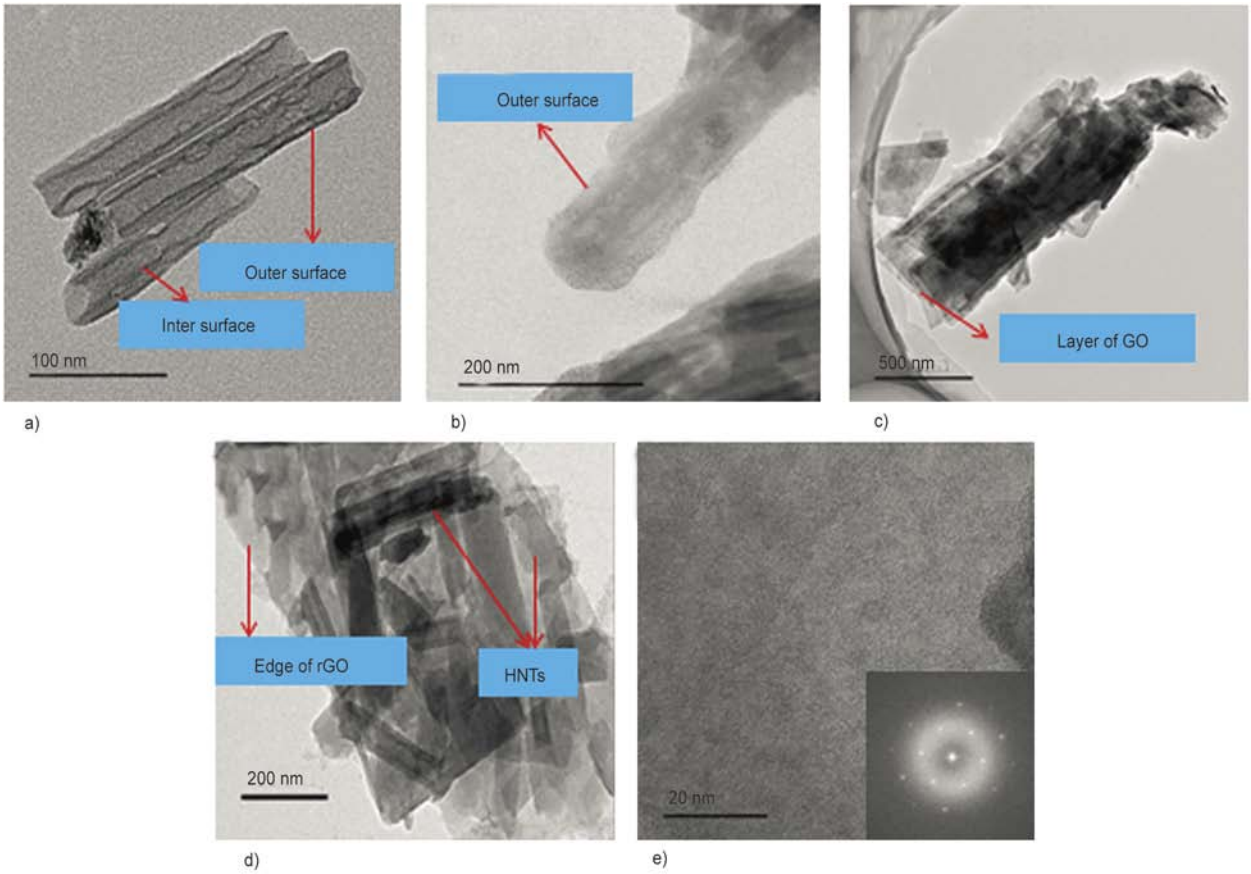

Figure 4. TEM images of (a) pristine HNTs, (b) HNT-NH_2, (c) GO, (d) HNTs-*d*-rGO, (e) HRTEM of the rGO in HNTs-*d*-rGO (inset is the SAED pattern)

shows both diffraction rings and dots, which is consistent with high resolution transmission electron microscopy (HRTEM) results.

3.2. Dispersion of HNTs-*d*-rGO in the composites

The dispersion of fillers in PA6 is an important factor to affect the various properties of composites. It is necessary to obtain the morphological information of fillers in the matrix. In this study, SEM was used to examine the dispersion of HNTs, GO, HNTs-*d*-rGO and HNTs-*m*-rGO in PA6. In order to show the dispersion state more clearly, the fractured surfaces of PA6 composites made by cryo-fractured in liquid nitrogen were etched with $C_2HCl_3O_2$ (30 wt%)/C_2H_5OH solution at 60°C for 1 h. It is evident that HNTs are homogeneously dispersed in the PA6/HNTs composites (Figure 5a). As shown in Figure 5b, many GO sheets could be observed on the fractured surface and they are uniformly dispersed in the PA6/GO composites without agglomeration. Figure 5c presents a good dispersion of HNTs-*d*-rGO in PA6 matrix and less isolated HNTs and their aggregates compared with those in PA6/HNTs-*m*-rGO composite (as shown in Figure 5d), indicating a strong interaction between the rGO sheets and the HNTs, which may be good for the flame retardant property of PA6 composite.

3.3. Flame-retardant properties of the PA6 composites

The cone calorimeter test results for PA6 and the corresponding composites filled with 1 wt.% of HNTs, GO and HNTs-*d*-rGO prepared by melt blending are presented in Figure 6 and Table 1. From Figure 6a, it can be observed that pure PA6 burns rapidly after ignition and the peak heat release rate (PHRR) value is 663 kW/m^2. As expected, incorporating HNTs and GO into PA6 makes the PHRR decrease to 634 and 617 kW/m^2 respectively. Moreover, the PHRR

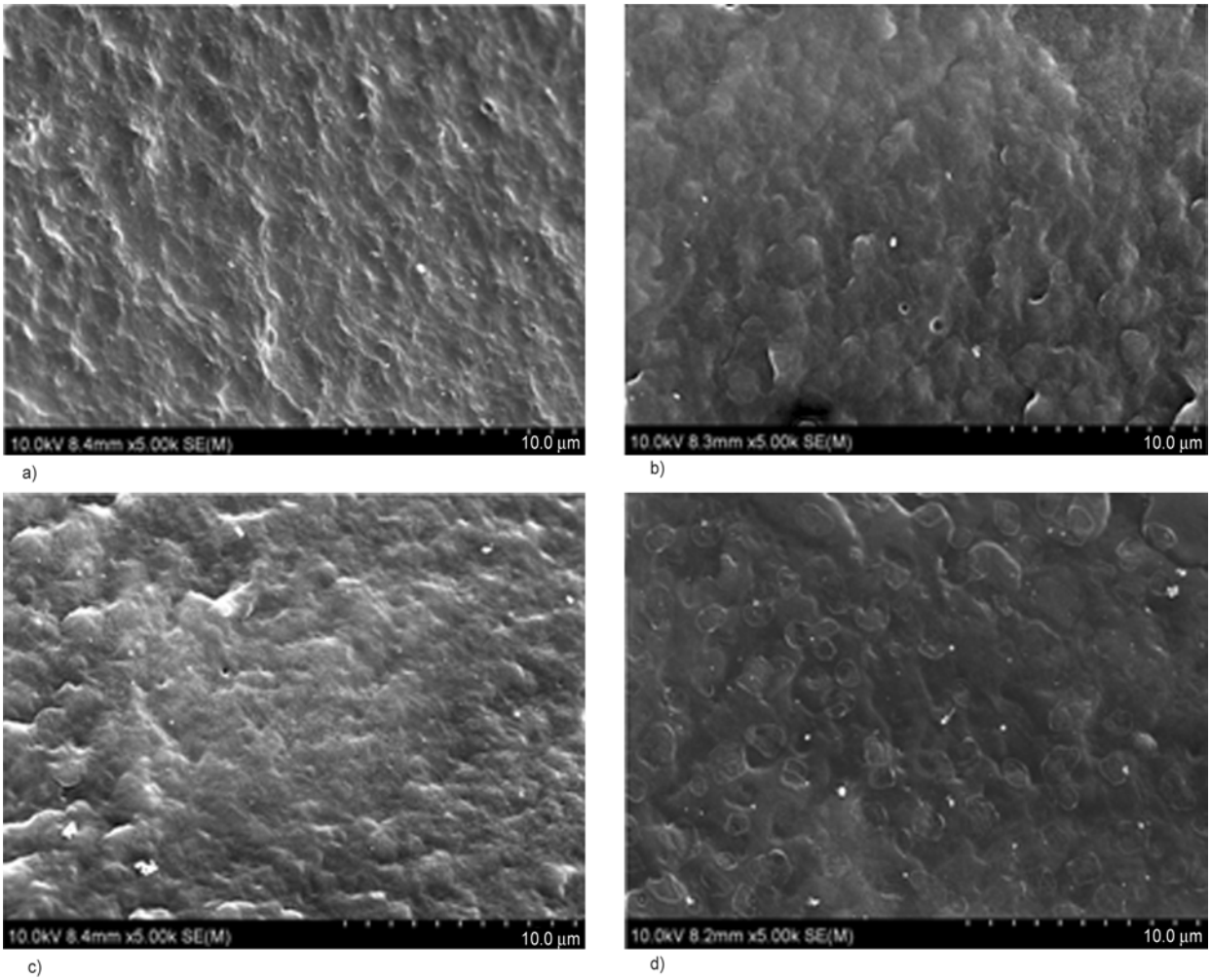

Figure 5. SEM images obtained from fracture surface of 1.0 wt% (a) pristine HNTs, (b) GO, (c) HNTs-*d*-rGO, (d) HNTs-*m*-GO in PA6 matrix etched with 30 wt% trichloroacetic acid/ethanol solution at 60°C for 1 h

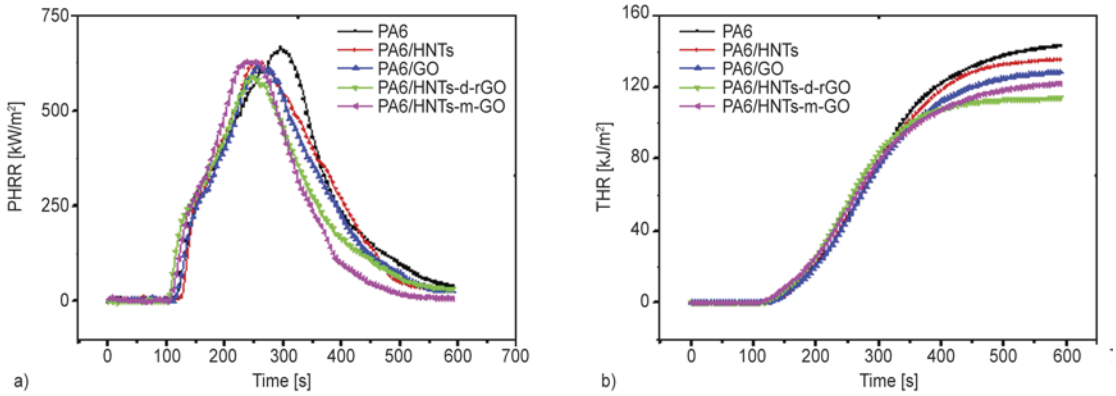

Figure 6. Heat release rate (HRR) (a), total heat release (THR) (b) versus time curves of polyamide 6

Table 1. Cone test results for PA6 and PA6 composites

Samples	PHRR [kW/m^2]	THR [MJ/m^2]	TTI [s]	TSP [m^2/m^2]
PA6	663	142.6	110	4.26
PA6/HNTs	634	135.0	121	4.35
PA6/GO	617	128.2	99	4.98
PA6/HNTs-*d*-rGO	588	113.6	107	4.72
PA6/HNTs-*m*-GO	628	122.0	104	4.70

of PA6/HNTs-*d*-rGO composite exhibits a further reduction compared to both PA6/HNTs and PA6/GO. To clarify whether the grafting effect or the effect of a simple combination of HNTs and CNTs was responsible for this result, we conducted a contrast experiment by physically mixing HNTs and GO in PA6. The PHRR for this composite was higher than HNTs-*d*-rGO at the same loading level, indicating the grafting was good for the fire retardancy. Therefore, the best fire retardant properties of PA6/HNTs-*d*-rGO could be attributed to two aspects: firstly, the reduction of GO converts GO into a more stable form, reduced GO (rGO); Secondly, HNTs can create a stable silica layer on the char surface of PA6, which reinforces the barrier effect of graphene. From Figure 6b,The total heat release (THR) curves show a similar trend as heat release rate (HRR), and THR values of PA6/ HNTs, PA6/GO, PA6/HNTs-*d*-rGO are reduced from 142.6 MJ/m^2 (pure PA6) to 135.0, 128.2 and 113.6 MJ/m^2, respectively. While the PA6/HNTs-*m*-GO exhibits the higher THR value than PA6/ HNTs-*d*-rGO, which proves the above mechanism for the best fire retardant properties of PA6/HNTs-*d*-rGO again. From Table 1, it can be found that incorporation of the nanofillers has a slight influence on the time-to-ignition (TTI) of the composites, owing to their small loadings. With regard to the total smoke production (TSP), all the samples containing nanofillers show higher TSP compared to pure PA6. This phenomenon is probably due to the incomplete combustion of PA6.

4. Conclusions

In summary, we have firstly reported the covalently bonded HNT-*d*-rGO nanostructures, which successfully improved the flame-retardant properties as the fillers in PA6 from the PHRR and THR results. The nanostructures of HNT-*d*-rGO were determined by FTIR, XPS, and TEM studies. A morphological study revealed that HNTs-*d*-rGO was dispersed well in PA6. Our results indicate that the improvement in flame-retardancy of HNT-*d*-rGO hybrid composite may due to the barrier effect of its network. The HNT-*d*-rGO hybrid composites open up a new strategy to be applied towards a wide range of polymers materials as an effective fillers to improve the fire safety of polar polymers.

Acknowledgements

This study is supported by The National Science Fund for Distinguished Young Scholars (50925312), Program of Changjiang Scholars and Innovative Research Team in University (T2011079, IRT1221) and Research Program of Shanghai Science and Technology Commission (12nm 0500200 and 11nm 0500100). The authors thank Jiangsu Haiyang Chemical Fiber Co., Ltd. for kindly providing the PA6 samples used in this study.

References

[1] Kim G-M., Michler G. H., Ania F., Balta Calleja F. J.: Temperature dependence of polymorphism in electrospun nanofibres of PA6 and PA6/clay nanocomposite. Polymer, **48**, 4814–4823 (2007).
DOI: 10.1016/j.polymer.2007.05.082

[2] Ryu Y. J., Kim H. Y., Lee K. H., Park H. C., Lee D. R.: Transport properties of electrospun nylon 6 nonwoven mats. European Polymer Journal, **39**, 1883–1889 (2003).
DOI: 10.1016/S0014-3057(03)00096-X

[3] Cai Y., Huang F., Wei Q., Song L., Hu Y., Ye Y., Xu Y., Gao W.: Structure, morphology, thermal stability and carbonization mechanism studies of electrospun PA6/Fe-OMT nanocomposite fibers. Polymer Degradation and Stability, **93**, 2180–2185 (2008).
DOI: 10.1016/j.polymdegradstab.2008.08.003

[4] Abacha N., Kubouchi M., Sakai T.: Diffusion behavior of water in polyamide 6 organoclay nanocomposites. Express Polymer Letters, **3**, 245–255 (2009).
DOI: 10.3144/expresspolymlett.2009.31

[5] Zang J., Ryu S., Pugno N., Wang Q., Tu Q., Buehler M. J., Zhao X.: Multifunctionality and control of the crumpling and unfolding of large-area graphene. Nature Materials, **12**, 321–325 (2013).
DOI: 10.1038/NMAT3542

[6] Fardindoost S., Mohammadi S., Iraji zad A., Sarvari R., Shariat Panahi S. P., Jokar E.: Electromechanical resonator based on electrostatically actuated graphene-doped PVP nanofibers. Nanotechnology, **24**, 135201/1–135201/6 (2013).
DOI: 10.1088/0957-4484/24/13/135201

[7] Majumdar A., Kim J., Vuckovic J., Wang F.: Electrical control of silicon photonic crystal cavity by graphene. Nano Letters, **13**, 515–518 (2013).
DOI: 10.1021/nl3039212

[8] Prakash A., Misra S. K., Bahadur D.: The role of reduced graphene oxide capping on defect induced ferromagnetism of ZnO nanorods. Nanotechnology, **24**, 095705/1–095705/10 (2013).
DOI: 10.1088/0957-4484/24/9/095705

[9] Veca L. M., Meziani M. J., Wang W., Wang X., Lu F., Zhang P., Lin Y., Fee R., Connell J. W., Sun Y-P.: Carbon nanosheets for polymeric nanocomposites with high thermal conductivity. Advanced Materials, **21**, 2088–2092 (2009).
DOI: 10.1002/adma.200802317

[10] Balandin A. A., Ghosh S., Bao W. Z., Calizo I., Teweldebrhan D., Miao F., Lau C. N.: Superior thermal conductivity of single-layer graphene. Nano Letters, **8**, 902–907 (2008).
DOI: 10.1021/nl0731872

[11] Huang G., Gao J., Wang X., Liang H., Ge C.: How can graphene reduce the flammability of polymer nanocomposites? Materials Letters, **66**, 187–189 (2012).
DOI: 10.1016/j.matlet.2011.08.063

[12] Bao C., Song L., Wilkie C. A., Yuan B., Guo Y., Hu Y., Gong X.: Graphite oxide, graphene, and metal-loaded graphene for fire safety applications of polystyrene. Journal of Materials Chemistry, **22**, 16399–16406 (2012).
DOI: 10.1039/c2jm32500d

[13] Song P., Liu L., Fu S., Yu Y., Jin C., Wu Q., Zhang Y., Li Q.: Striking multiple synergies created by combining reduced graphene oxides and carbon nanotubes for polymer nanocomposites. Nanotechnology, **24**, 125704/1–125704/8 (2013).
DOI: 10.1088/0957-4484/24/12/125704

[14] Pack S., Kashiwagi T., Cao C. H., Korach C. S., Lewin M., Rafailovich M. H.: Role of surface interactions in the synergizing polymer/clay flame retardant properties. Macromolecules, **43**, 5338–5351 (2010).
DOI: 10.1021/ma100669g

[15] Dasari A., Yu Z-Z., Mai Y-W., Liu S.: Flame retardancy of highly filled polyamide 6/clay nanocomposites. Nanotechnology, **18**, 445602/1–445602/10 (2007).
DOI: 10.1088/0957-4484/18/44/445602

[16] Handge U. A., Hedicke-Höchstötter K., Altstädt V.: Composites of polyamide 6 and silicate nanotubes of the mineral halloysite: Influence of molecular weight on thermal, mechanical and rheological properties. Polymer, **51**, 2690–2699 (2010).
DOI: 10.1016/j.polymer.2010.04.041

[17] Liu M., Guo B., Zou Q., Du M., Jia D.: Interactions between halloysite nanotubes and 2,5-bis(2-benzoxazolyl) thiophene and their effects on reinforcement of polypropylene/halloysite nanocomposites. Nanotechnology, **19**, 205709/1–205709/10 (2008).
DOI: 10.1088/0957-4484/19/20/205709

[18] Liu C., Luo Y. F., Jia X. X., Zhong B. C., Li S. Q., Guo B. C., Jia D. M.: Enhancement of mechanical properties of poly(vinyl chloride) with polymethyl methacrylate-grafted halloysite nanotube. Express Polymer Letters, **5**, 591–603 (2011).
DOI: 10.3144/expresspolymlett.2011.58

[19] Liu M. X., Guo B. C., Du M. L., Chen F., Jia D. M.: Halloysite nanotubes as a novel β-nucleating agent for isotactic polypropylene. Polymer, **50**, 3022–3030 (2009).
DOI: 10.1016/j.polymer.2009.04.052

[20] Guo B., Zou Q., Lei Y., Du M., Liu M., Jia D.: Crystallization behavior of polyamide 6/halloysite nanotubes nanocomposites. Thermochimica Acta, **484**, 48–56 (2009).
DOI: 10.1016/j.tca.2008.12.003

[21] Marney D. C. O., Russell L. J., Wu D. Y., Nguyen T., Cramm D., Rigopoulos N., Wright N., Greaves M.: The suitability of halloysite nanotubes as a fire retardant for nylon 6. Polymer Degradation and Stability, **93**, 1971–1978 (2008).
DOI: 10.1016/j.polymdegradstab.2008.06.018

[22] Yuan P., Southon P. D., Liu Z., Green M. E. R., Hook J. M., Antill S. J., Kepert C. J.: Functionalization of halloysite clay nanotubes by grafting with γ-aminopropyltriethoxysilane. Journal of Physical Chemistry C, **112**, 15742–15751 (2008).
DOI: 10.1021/jp805657t

[23] Yah W. O., Takahara A., Lvov Y. M.: Selective modification of halloysite lumen with octadecylphosphonic acid: New inorganic tubular micelle. Journal of the American Chemical Society, **134**, 1853–1859 (2012). DOI: 10.1021/ja210258y

[24] Hummers W. S., Offeman R. E.: Preparation of graphitic oxide. Journal of the American Chemical Society, **80**, 1339–1339 (1958). DOI: 10.1021/ja01539a017

[25] Petit C., Bandosz T. J.: MOF-graphite oxide composites: Combining the uniqueness of graphene layers and metal-organic frameworks. Advanced Materials, **21**, 4753–4757 (2009). DOI: 10.1002/adma.200901581

[26] Bagri A., Mattevi C., Acik M., Chabal Y. J., Chhowalla M., Shenoy V. B.: Structural evolution during the reduction of chemically derived graphene oxide. Nature Chemistry, **2**, 581–587 (2010). DOI: 10.1038/NCHEM.686

[27] Ou J., Wang J., Liu S., Mu B., Ren J., Wang H., Yang S.: Tribology study of reduced graphene oxide sheets on silicon substrate synthesized via covalent assembly. Langmuir, **26**, 15830–15836 (2010). DOI: 10.1021/la102862d

[28] Wittberg T. N., Wang P. S.: XPS study of the dehydration of clay and kaolin powders. Surface and Interface Analysis, **27**, 936–940 (1999). DOI: 10.1002/(SICI)1096-9918(199910)27:10<936::AID-SIA656>3.0.CO;2-N

[29] Stankovich S., Dikin D. A., Piner R. D., Kohlhaas K. A., Kleinhammes A., Jia Y., Wu Y., Nguyen S. T., Ruoff R. S.: Synthesis of graphene-based nanosheets via chemical reduction of exfoliated graphite oxide. Carbon, **45**, 1558–1565 (2007). DOI: 10.1016/j.carbon.2007.02.034